RESONANT ELECTRON DYNAMICS IN OPEN NANO SCALE SYSTEMS: A TIME-DEPENDENT NON-EQUILIBRIUM GREEN FUNCTION APPROACH

by

Alexander H. Prociuk

A dissertation submitted in partial fulfillment
of the requirements for the degree of
Doctor of Philosophy
(Physics)
in The University of Michigan
2009

Doctoral Committee:

Assistant Professor Barry D. Dunietz, Co-Chair
Professor Paul R. Berman, Co-Chair
Professor Bradford G. Orr
Associate Professor Eitan Geva
Associate Professor Roseanne J. Sension
Assistant Professor Alexei V. Tkachenko

To my wife Amy, her parents, Greg and Sandy, and my parents Anatol and Barbara, for planting faith in me when I doubted myself.

ACKNOWLEDGEMENTS

I owe a very special thanks to my advisor, Barry Dunietz. Without his guidance, this project would certainly not have come to fruition.

I would also like to thank the computational chemistry staff, in particular, Todd Raeker and Doug Cox. Their quick effective responses to computer and cluster problems simplified my life by orders of magnitude.

Finally, I would like to thank Eitan Geva and Roi Baer for their indispensable advice.

TABLE OF CONTENTS

LIST OF FIGURES

Figure

LIST OF TABLES

Table

LIST OF APPENDICES

Appendix

CHAPTER I

Introduction

The forces that motivate research in nanometer length scale devices are manyfold. On the one hand, the field is driven by a quest for greater device efficiency, including, the further miniaturization of devices, the ability to increase the speed of information transfer, lower power requirements and large reduction of noise induced errors. On the other hand, nano-scale devices have the ability to directly exploit unique quantum effects such as electroluminescence (flux enabled spectroscopic transitions), negative differential resistance and absolute negative conductance. Examples of such nano-scale devices include the quantum dot and the molecular wire. A host of experimental research has already been performed on both of these types of systems[62, 58, 94, 93, 41, 72, 64, 63, 91, 90, 17, 127, 46, 116, 138, 102, 28, 32, 31, 56, 42, 96, 75, 78, 1, 81, 80, 45, 113, 95, 33, 34, 121, 86, 66, 130, 129, 47, 43, 97, 132, 60, 85, 27, 122, 103].

The ever-increasing ability to fabricate such devices demands the development of a theoretical formalisms and computational models to both predict and explain their underlying physics and chemistry. As a result, a host of theoretical methods and models have been developed to study these fundamental aspects. [133, 36, 118, 134, 35, 135, 3, 11, 55, 39, 109, 9, 11, 10, 110, 87, 24, 23, 65, 104, 29, 101, 59, 57, 18, 70, 123, 13, 14, 79, 65, 111, 30, 112, 98, 76, 89, 128, 124, 115, 108, 22, 20, 116,

Figure 1.1: Two examples of open systems: molecular junction C centered between two electrodes L,R under source-drain bias V carries current I (left) and a system of two coupled quantum dots l,r connected to two electrodes *source,drain* (right – image taken from [93]).

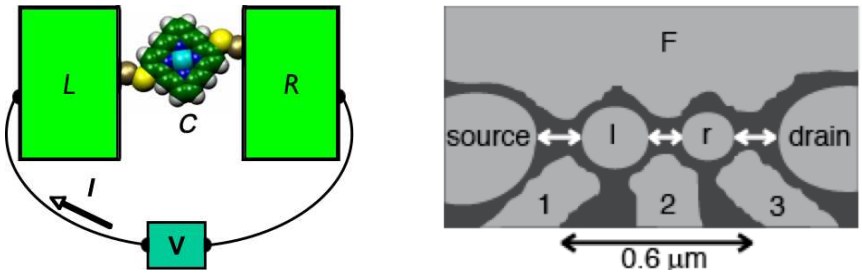

138, 21, 126, 82, 7, 6, 120, 61, 2, 5, 112, 73, 74, 26, 83, 25, 4, 8] These approaches are based on an *open system* picture of the device (fig. 1.1) [67, 12, 54]. In this picture, the quantum mechanical junction connects two large (typically semi-infinite) electrodes.[105, 119, 136, 40, 88, 114] A source drain bias and time dependent driving fields are then applied to the system and the response is characterized. For simplicity, vibrational modes are neglected and the structure of the device is assumed to be rigid. Only electron motion is considered.

Outline of dissertation

This work focuses on the development and implementation of a methodology for modeling open systems under the influence of weak time dependent driving fields.

Chapter II provides experimental background and a brief summary of the development goals for this methodology. In addition, justifications for basing the derived methodology on the non-equilibrium Green function (NEGF) formalism is provided.

Chapters III, IV and V give a detailed pedagogical and working description of the aspects of NEGF formalism relevant to the methodology developed in this work. An introduction to propagation formalism and many body (field) theory is provided in Chapter III. The description in these chapters culminates with the introduction of

the crucial quantity of interest, the lesser Green function (GF) and the derivation of its properties and fundamental equation of motion (chapter IV). Finally, a relevant derivation of GF-theory for a time independent Hamiltonian is provided in V. This is the basis for already widely used theories, such as Landauer theory. More importantly, the results from this chapter will provide the "initial" conditions for the time-dependent (TD) theory provided in later chapters, thus connecting my TD methodology to already well known and frequently used steady state quantities.

Chapter VI describes, in detail, my formal contributions to this area of research. The time dependent NEGF equations of motion used to characterize the time dependent propagation of an open system in terms of its manifold of states is derived. Furthermore, the special case of a system under the influence of a time-independent applied potential is derived from these equations. This constant potential theory (CPT) indicates that "constant" dynamic responses, such as steady state current, cannot be captured by a simple steady state theory where the system is statistically equilibrated (chapter V). Instead, these properties are inherently dynamic and manifest themselves on the transition density matrix elements.

Chapter VII applies the theory developed in chapter VI to simple two and four site open systems under an applied time independent ramped potential (source-drain bias), and an applied oscillating potential (laser field). Among other results, two fundamental phenomena are simulated, namely, electroluminescence and population inversion induced absolute negative conductance.

Chapter VIII describes formal and numerical disagreements between CPT and Landauer theory and sketches a formal path that can potential resolve these issues.

Finally, this work is summarized in chapter IX.

CHAPTER II

Experimental Motivation and Methodological Objectives

2.1 Time Dependent Experiments

In this chapter, we provide a few examples of experimental research that motivate the study of time dependent open systems and transient transport modeling in particular. The volume of experimental work in this field is expansive.[62, 58, 94, 93, 41, 72, 64, 63, 91, 90, 17, 127, 46, 116, 138] Thus, this section is not intended to give detailed summaries of all of this work. Instead, a focus is placed on describing some of the different types of experiments that have been performed in time dependent transport. For example, we describe work on absolute negative conductance caused by temporal driving fields since we model this effect in a later chapter. We now elaborate on some of these works.

In 1995, Keay and co-workers[58] fabricated a ten quantum well n-doped GaAs hetero-structure with eleven potential barriers and characterized photon assisted electronic transport that lead, in particular, to the observation of current suppression and absolute negative conductance at low applied source-drain bias (fig. 2.1). The mechanism for this absolute negative conductance is depicted in figure 2.2 for the case of two quantum wells. When the source drain bias shifts the ground state of the first well into alignment with the excited state of the second well and population is

Figure 2.1: I-V characteristics for varying strengths of applied (1.30 THz/5.38meV) radiation field. Figure taken from [58].

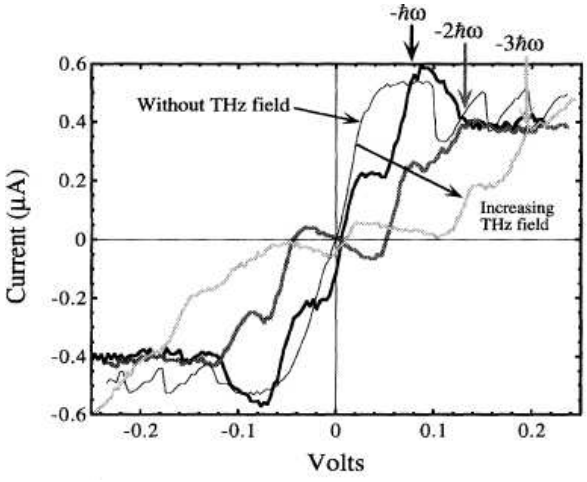

Figure 2.2: Schematic diagram depicting forward and reverse current mechanisms in a two quantum well system. Figure taken from [58].

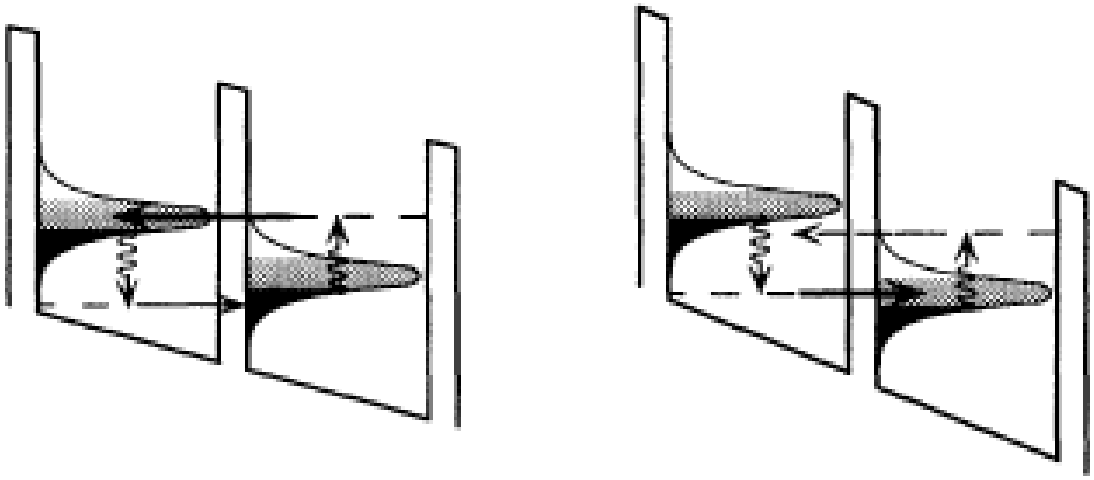

Figure 2.3: Photon assisted transport mechanisms involving the ground ϵ_0 and first excited ϵ_1 quantum dot states and microwave frequency f. Left panels: electrons are pumped from the left electrode to either quantum dot state and subsequently traverse under bias to the right electrode. Center top panel: electrons traverse directly from the left electrode through the ground quantum dot state to the right electrode. Center bottom: Electrons traverse from left electrode through excited quantum dot state to right electrode ONLY AFTER the coulomb blockade is lifted via pumping the ground state electron out of the quantum dot. Right panels: electrons traverse from left electrode to quantum dot states and are subsequently pumped from the quantum dot to the right electrode. Figure taken from [94].

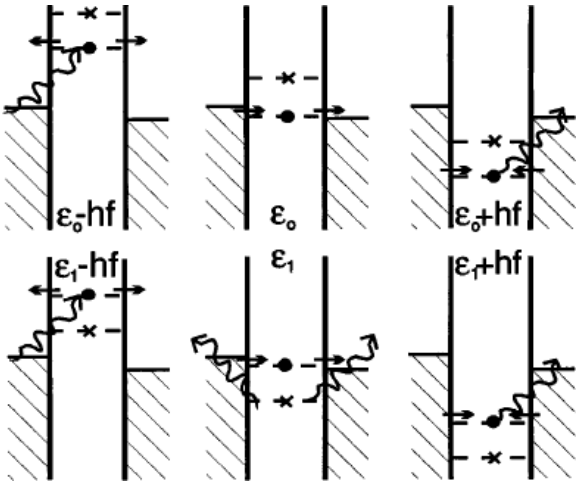

transfered by the radiation field from the ground to first excited state in the second well, a reversal in the direction of the current can be achieved. This mechanism can, in a sense be seen as population inversion induced absolute negative conductance. In section 7.3 we will show theoretically and computationally that population inversion can indeed lead to absolute negative conductance.

In 1997, Oosterkamp and coworkers[94] performed an experiment on a single quantum dot coupled to two electrodes. A gate voltage was applied to the quantum dot that changed its on-site energy relative to the electrodes. The quantum dot was also subjected to a microwave oscillating potential. The ground and first excited single electron states of the quantum dot, ϵ_0 and ϵ_1, respectively, exhibited resonant transport at energies $\epsilon_0 \pm h\nu$ and $\epsilon_1 \pm h\nu$. Figure 2.3 depicts the pumping mechanisms of these systems, where electron pumping assists in transport. Electrons are

Figure 2.4: Current as a function of gate voltage and applied microwave field strength. Figure taken from [94].

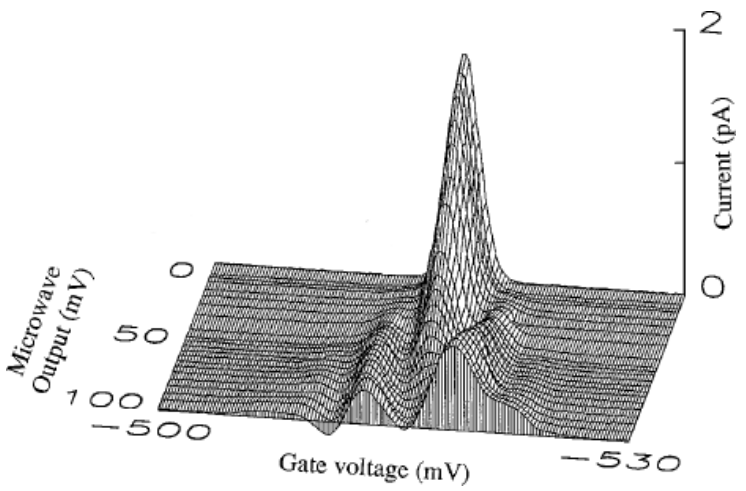

either pumped from the electrode to a given quantum dot state (fig. 2.3 left panels), resonate through the quantum dot states (fig. 2.3 center panels), or are pumped from the quantum dot states to the electrodes (fig. 2.3 right panels). In the case of resonant tunneling directly through the states, two distinct mechanisms are observed. The simpler mechanism involves tunneling through the ground state without the assistance of the microwave pump (fig. 2.3 center top). The second mechanism involves the alleviation of the coulomb blockade by pumping the electron in the ground quantum dot state out to the electrodes (fig. 2.3 center bottom). Figure 2.4 depicts the emergence of resonant current sidebands with increasing microwave field amplitude. The sidebands displaced from the state by the microwave frequency as expected. In this run, the microwave field frequency (110 μeV, or 27 GHz) was kept lower than the ϵ_0 to ϵ_1 excitation energy (110 μeV) to avoid this resonance.

In 1998 Oosterkamp and co-workers[93] performed a photoassisted electronic transport experiment on a two-coupled quantum dot system (fig. 2.5). Through painstaking effort, a single state in each quantum dot was decoupled from the other states in that quantum dot to create a two state system with a tunable coupling coefficient

Figure 2.5: Image of two-coupled quantum dot system. The two quantum dots (l and r) are also coupled to source and drain electrodes. The electrodes 1,2,3 and F are used to vary the dot-dot and dot-electrode interaction energies. Figure taken from [93].

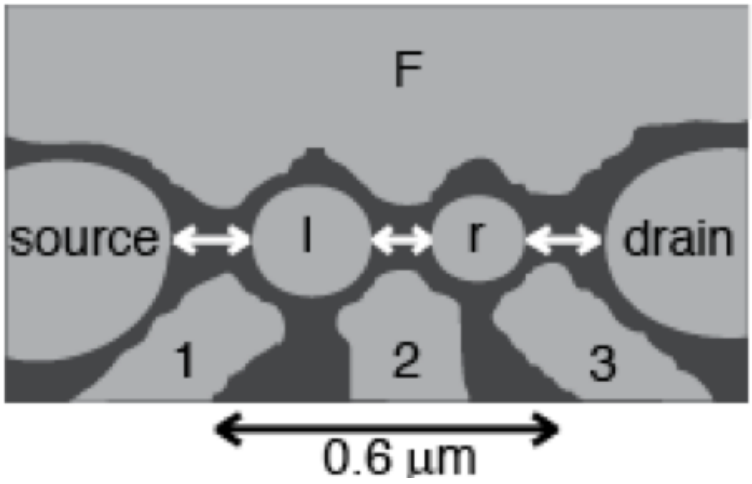

between the states (i.e. and tunable potential barrier between the two quantum dots). When the coupling energy between the two dots was small compared to the applied source-drain bias, each state was localized to a quantum dot. When the coupling strength was large compared to the source-drain bias, the two states were delocalized over both quantum dots forming a bonding and anti-bonding orbital. Oscillating microwave fields of varying frequencies were then applied to the system and current was measured as a function of applied source drain bias. Figure 2.6 shows the current voltage profiles for several cases of microwave carrier frequency. Note that the intensity of current increases at voltages corresponding to the microwave carrier frequency clearly indicating that photon pumping assists in the transport properties of the quantum dot system.

2.2 Theoretical Synopsis

Both steady state and time dependent problems summarized above require a characterization of the electrons' behavior resolved in terms of the electron's energies. In addition, the thermal decoherent nature of the electronic initial conditions require

Figure 2.6: (a-c) photon assisted transport mechanisms above their appropriate regions in d–the solid lines represent single dot state energies (analogous to atomic orbital energies) while the dashed lines represent level of delocalization for coupled two-dot state energies (analogous to molecular orbital energies); (d) I-V profiles for varying microwave frequencies. Figure taken from [93].

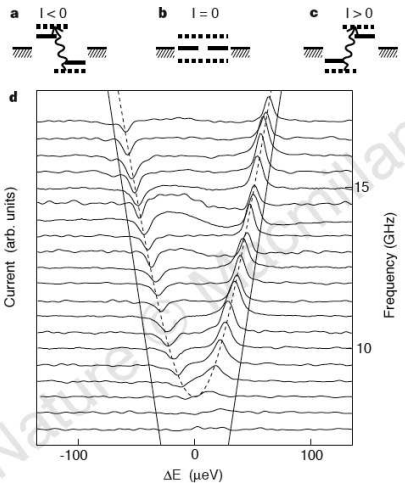

a density matrix description. In a closed system, such as an isolated molecule, these two requirements can be simultaneously met because every diagonal element of the density matrix corresponds to a single state of the system (as seen in the diagonal representation). In an open system, such as a molecular junction, this is no longer true. The density of states for such a system is often dominated by bands of infinite numbers of scattering states in a given conducting channel. Yet the density matrix for the junction is described by a finite number of basis functions and is, therefore, of finite dimension. This difference between open and closed systems is most readily seen from their respective molecular orbital diagrams. Consider, for example, two systems whose electronic structure is described by one p_z orbital on each atom (fig. 2.7). The density matrix, $\boldsymbol{\rho}(t)$, for the closed system (fig. 2.7a) is a 2x2 matrix. Furthermore, there is a one to one correspondence between the matrix elements and the eigenstates. That is, in the diagonalized representation, each diagonal $\rho_{ii}(t)$ gives the population in state i, etc., for $i = 1, 2$. Now, consider the open system

(fig. 2.7b). In this case, the junction is defined by the two central atoms while the two shaded outer atoms represent the electron reservoirs. The coupling between the junction and the reservoirs contributes extra states. There is no longer a one-to-one correspondence between the elements of the density matrix and the states. To resolve this issue, a density matrix representation for the two central atoms that gives dynamical information on the manifold of all four states must be derived. A way of expressing such a density matrix is $\rho_{ij}(E_k, t)$ where, as in the closed system case, $i, j = 1, 2$ are the two central atomic orbital indices and $k = 1, .., 4$ are the indices of the four states. We have gained a third index k that distinguishes between the four states because the indices i, j no longer do.

Figure 2.7: Molecular orbital diagrams for (a) two atom closed (isolated) system; (b) open system composed of two (central) atoms connected to two outer atoms

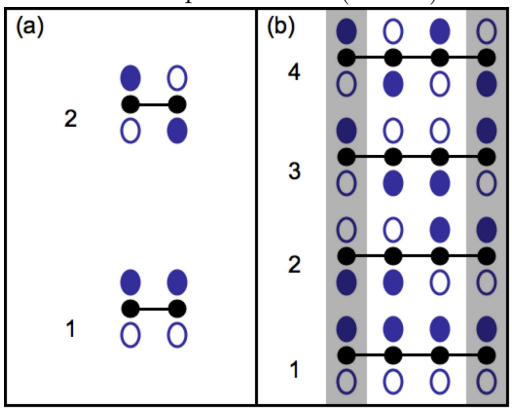

Now, one question remains. What is the meaning (if any) of the elements of the 2x2 density matrix. Note that, unlike the closed system, there is no single 2x2 Hamiltonian for the two central atoms that can simultaneously diagonalize $\rho_{ij}(E_k, t)$ for all four E_k states. This is a consequence of entangling the two central-atom system with the two outer atoms.

On the other hand, the atomic orbital (AO) basis is the set of two p_z orbitals, one on each of the two central atoms. The AO basis functions do not depend on

k. Thus, in the AO representation, the diagonal element $\rho_{ii}^{(AO)}(E_k,t)$ gives the k-th state contribution to the charge density of the i-th atom. The off-diagonal element $\rho_{12}^{(AO)}(E_k,t)$ gives the k-th state contribution to the bond order between the two central atoms. The total AO charge density matrix is found by summing over all four k states:

$$\boldsymbol{\rho}^{(AO)}(t) = \sum_{k=1}^{4} \boldsymbol{\rho}^{(AO)}(E_k,t) \tag{2.1}$$

Furthermore, for any given operator expressed in the two atom AO basis, the trace of $\boldsymbol{\rho}^{(AO)}(E_k,t)$ with this operator gives the k-th state contribution to the expectation value of the operator. Summing over the k traces gives the total expectation value of the operator.

$$\langle \mathbf{O}(t) \rangle = \sum_{k=1}^{4} Tr\left[\boldsymbol{\rho}^{(AO)}(E_k,t)\mathbf{O}\right] \tag{2.2}$$

Finally, this simple example may be extended to the case of a finite junction bonded to two electrodes, each with an infinite number of atoms. Such a system would be represented by a density matrix of not four E_k-states, but rather, an infinite number of E_k-states grouped into continuous energy bands. Mathematically, it becomes more convenient to replace E_k with a continuous variable E. The sum in the equations above is replaced by an integral.

$$\boldsymbol{\rho}^{(AO)}(t) = \int dE \boldsymbol{\rho}^{(AO)}(E,t) \tag{2.3}$$

$$\langle \mathbf{O}(t) \rangle = \int Tr\left[\boldsymbol{\rho}^{(AO)}(E,t)\mathbf{O}\right] dE \tag{2.4}$$

As before $\boldsymbol{\rho}^{(AO)}(E,t)dE$ gives the contribution to the electronic charge (charge densities and bond orders) of the states with energies between E and $E+dE$. The trace of $\boldsymbol{\rho}^{(AO)}(E,t)$ with a given AO operator gives the contribution of the states

with energies between E and $E + dE$ to the expectation value of that operator. The integral over E of the trace of the operator with $\boldsymbol{\rho}^{(AO)}(E, t)$ gives the expectation value of the operator.

Example: Two state system

For example, the wave packet for a two state system can be written as

$$\Psi(\mathbf{r}, t) = a_1 e^{-i\epsilon_1 t}\psi_1(\mathbf{r}) + a_2 e^{-i\epsilon_2 t}\psi_2(\mathbf{r}) \tag{2.5}$$

where ψ_1 and ψ_2 are eigenfunctions of a system described by a given Hamiltonian $\hat{H}$,

$$\hat{H}\psi_i(\mathbf{r}) = \epsilon_i \psi_i(\mathbf{r}). \tag{2.6}$$

For simplicity, we assume that ψ_1 and ψ_2 are real valued. The total electronic density for this wave packet is given by,

$$\rho(\mathbf{r}; t) \equiv |\Psi(\mathbf{r}, t)|^2 = |a_1|^2|\psi_1(\mathbf{r})|^2 + |a_2|^2|\psi_2(\mathbf{r})|^2 + 2a_1 a_2 \psi_1(\mathbf{r})\psi_2(\mathbf{r}) \cos(\Delta\epsilon\, t) \tag{2.7}$$

where the occupation numbers of eigenstates 1 and 2 are given by $|a_1|^2$ and $|a_2|^2$ respectively, and $\Delta\epsilon \equiv \epsilon_2 - \epsilon_1$. Multireference electronic structure methods such as configuration interaction (CI) solve for the ground and excited electronic eigenstates and, more importantly, eigenenergies of a closed molecular system (eqn. 2.6). One can subsequently use this information to construct and propagate wave packets in time (e.g. eqn. 2.5) and calculate time dependent electron densities (e.g. eqn. 2.7).

However, one can consider an alternative representation of the same problem, focusing on the density, but with a crucial change. Instead of calculating expression

2.7, one may define an expression for the *correlated* density,

$$\begin{aligned}\rho_c(\mathbf{r};t,\Delta t) \equiv& \Psi(\mathbf{r},t+\Delta t/2)\Psi^*(\mathbf{r},t-\Delta t/2)\\ =&|a_1|^2 e^{-i\epsilon_1\Delta t}|\psi_1(\mathbf{r})|^2 + |a_2|^2 e^{-i\epsilon_2\Delta t}|\psi_2(\mathbf{r})|^2\\ &+ 2a_1a_2\psi_1(\mathbf{r})\psi_2(\mathbf{r})e^{-i\bar{\epsilon}\Delta t}\cos(\Delta\epsilon\, t).\end{aligned} \tag{2.8}$$

where $\bar{\epsilon} = (\epsilon_1 + \epsilon_2)/2$. Fourier transforming this expression produces an energy resolved correlated density of the form,

$$\begin{aligned}\tilde{\rho}_c(\mathbf{r};E,t) \equiv& \int d(\Delta t) e^{iE\Delta t}\rho_c(\mathbf{r};t,\Delta t)\\ =&\delta(E-\epsilon_1)|a_1|^2|\psi_1(\mathbf{r})|^2 + \delta(E-\epsilon_2)|a_2|^2|\psi_2(\mathbf{r})|^2\\ &+ 2a_1a_2\psi_1(\mathbf{r})\psi_2(\mathbf{r})\delta(E-\bar{\epsilon})\cos(\Delta\epsilon\, t).\end{aligned} \tag{2.9}$$

This energy resolved density matrix captures all of the physics of the given system described by $\hat{H}$. One can now extract certain properties of the system by spatially integrating $\tilde{\rho}_c(\mathbf{r};E,t)$ with a given operator of interest. For example, a spatial integral of $\tilde{\rho}_c(\mathbf{r};E,t)$ produces the *occupied* density of states,

$$\tilde{n}(E,t) \equiv \int d^3\mathbf{r}\tilde{\rho}_c(\mathbf{r};E,t) = \delta(E-\epsilon_1)|a_1|^2 + \delta(E-\epsilon_2)|a_2|^2. \tag{2.10}$$

A color map of $\tilde{n}(E,t)$ (fig. 2.8 - left) is given for $a_1 = 1$, $a_2 = 0.7$ and $\Delta\epsilon = 1$ (in arbitrary units). The delta functions have been replaced by broadened Lorentzian functions for ease of graphing. An important aspect of this representation is the ability to determine an occupation number of a selected state by integrating $\tilde{n}(E,t)$ only over that state. For example,

$$\int_{\epsilon_1-|\delta|}^{\epsilon_1+|\delta|} dE\, \tilde{n}(E,t) = |a_1|^2 \tag{2.11}$$

where δ represents a small window in E about ϵ_1. Note that the integral over all E gives the total occupation number,

$$n(t) = \int dE\, \tilde{n}(E,t) = |a_1|^2 + |a_2|^2. \tag{2.12}$$

In general, if a driving field is applied to the system, the occupation numbers can change in time and the physics of population transfer between states can be explored with this representation. In addition to characterizing population dynamics, this representation can be used to explore quantum interferences between states. For example, a spatial integral of $\tilde{\rho}_c(\mathbf{r}; E, t)$ with the dipole operator will select the interference fringes that indicate a quantum superposition of states (fig. 2.8 - right),

$$\tilde{\mu}(E,t) \equiv \int d^3\mathbf{r}\tilde{\rho}_c(\mathbf{r}; E, t)\mathbf{r} = 2a_1a_2\mu_{12}\delta(E-\bar{\epsilon})\cos(\Delta\epsilon\, t) \tag{2.13}$$

where $\mu_{12} \equiv \langle\psi_1|\hat{\mathbf{r}}|\psi_2\rangle$ is the transition dipole matrix between states 1 and 2. Note that the interference fringes between states 1 and 2 fall exactly in between the energies of these two states. As with the total occupation number, the total dipole response is given by integrating $\tilde{\mu}(E,t)$ over all E,

$$\mu(t) = \int dE\, \tilde{\mu}(E,t) = 2a_1a_2\mu_{12}\cos(\Delta\epsilon\, t). \tag{2.14}$$

For closed systems, this representation may seem redundant, given that it is simpler to calculate the eigenstates of $\hat{H}$ explicitly and then temporally propagate their wave packet or density matrix from initial conditions. Since all eigenstates are known, one can determine the behavior of the system by specifically selecting the eigenstates of interest. However, for an open infinite system, one often has a continuum of states distributed in energy bands, but one is usually only interested in the dynamics of a small subsystem that can be described in terms of a finite discrete set of states. In this case, the energy resolved TD representation described above offers a detailed description of the system as it evolves on a continuum of states, but allows for the use of a finite discrete basis set.

To illustrate this, we now extend the above example from a two state system to a system of arbitrary (even infinite) number of states. In an open system, these

states are often infinitesimally spaced in E and form bands. In this case, the energy resolved density, $\tilde{\rho}_c(\mathbf{r}; E, t)$, becomes

(2.15)

$$\tilde{\rho}_c(\mathbf{r}; E, t) \equiv= \sum_i \delta(E-\epsilon_i)|a_i|^2|\psi_i(\mathbf{r})|^2 + 2\sum_i \sum_{j>i} a_i a_j \psi_i(\mathbf{r})\psi_j(\mathbf{r})\delta(E-\bar{\epsilon}_{ij})\cos(\Delta\epsilon_{ij}t)$$

where the index i spans over all of the states, $\Delta\epsilon_{ij} \equiv \epsilon_j - \epsilon_i$, and $\bar{\epsilon}_{ij} = \frac{\epsilon_i+\epsilon_j}{2}$. For an open system, most of the eigenstates ψ_i are delocalized over a very large volume. One can write these states in terms of a spatially localized basis set $\{\phi_n(\mathbf{r})\}$, such as an atomic orbital (AO) basis set or the p-orbital basis set in figure 2.7,

$$\psi_i(\mathbf{r}) = \sum_n C_n^{(i)} \phi_n(\mathbf{r}). \tag{2.16}$$

In this case, the energy resolved density can be expressed in terms of this localized basis set,

$$\tilde{\rho}_c(\mathbf{r}; E, t) = \sum_{m,n} \tilde{\rho}_{m,n}^{(AO)}(E,t)\phi_n(\mathbf{r})\phi_m(\mathbf{r}) \tag{2.17}$$

where,

(2.18)

$$\tilde{\rho}_{m,n}^{(AO)}(E,t) \equiv \sum_i \delta(E-\epsilon_i)|a_i|^2 C_n^{(i)} C_m^{(i)} + 2\sum_i \sum_{j>i} a_i a_j C_n^{(i)} C_m^{(j)} \delta(E-\bar{\epsilon}_{ij})\cos(\Delta\epsilon_{ij}t).$$

In the case of AOs, for example, the coefficients $\tilde{\rho}_{n,n}^{(AO)}(E,t)$ gives the charge density contribution of the n-th AO, while for $m \neq n$ $\tilde{\rho}_{m,n}^{(AO)}(E,t)$ gives the contribution to the bond order between AOs m and n for the eigenstate located at E. A subsystem of interest can be fully described by selecting and propagating only those coefficients of interest. Thus, for example, the properties of a subsystem, adequately described by two AOs, can be calculated using a 2×2 AO density matrix,

$$\tilde{\rho}^{(AO)}(E,t) = \begin{bmatrix} \tilde{\rho}_{1,1}^{(AO)}(E,t) & \tilde{\rho}_{1,2}^{(AO)}(E,t) \\ \tilde{\rho}_{2,1}^{(AO)}(E,t) & \tilde{\rho}_{2,2}^{(AO)}(E,t) \end{bmatrix}. \tag{2.19}$$

where the only continuous variable is E. In a continuous basis (e.g. plane wave) representation, this calculation would require two continuous variables since the basis indices m and n would become continuous. Dynamic propagation operators must often be expressed as tensors (as will be described in a later chapter). In this case, using a continuous basis would require four continuous indices, instead of the one variable E. This becomes a serious bottleneck since calculation over these indices scales like a power law. For example, a grid of only ten points in E may require 10000 in a continuous basis expansion. This clearly illustrates the advantage of using an energy resolved approach to characterize the dynamic evolution of the manifold of states on an open system. In practice, one must find ways to calculate $\tilde{\rho}^{(AO)}_{m,n}(E,t)$ on a finite discrete localized basis set describing the subsystem of interest *without* having to calculate the entire set of states ψ_i. The approach used to solve this problem will be described in the following chapters.

Having described the positive aspects of this approach, it must be noted that this approach is only exactly applicable to systems described by a time independent Hamiltonian. It is, therefore, a valid approximation to apply to the problem of weak TD classical driving fields where, for example, the Rabi frequency is much smaller than either the transition energy between states or the width of energy bands in question. In the strong field case (where the Rabi frequency is comparable to the transition energy) the physical meaning of E becomes unclear. Hence, a focus is placed on developing a time dependent perturbation theory approach to propagating the dynamics in this energy resolved framework.

The example given above is based on a single particle. The wave packet Ψ is a function of one set of three dimensional coordinates designated by $\mathbf{r}$. Most electronic devices are systems of many electrons and many methods exist for treating

such systems. These approaches reduce the many electron problem to an effective one electron problem. The fundamental problem for such methodologies involves appropriately treating the two electron coulomb repulsion potentials in the Hamiltonian. These approaches fall into two classes, namely, density functional theory (DFT) approaches [9, 11, 10, 110, 87, 24, 23, 65, 104, 29, 101] and non-equilibrium Green function (NEGF) approaches [44, 3, 11, 55, 59, 57, 18, 70, 123, 13, 14, 79].

DFT approaches map these interactions to a one-body mean field potential that is a functional of the density []. These approaches have the advantage that they are purely one variable (t) methodologies. This is ideal for closed systems and very sensible for open systems under the influence of strong TD driving fields where the time independent Hamiltonian states are no longer offer the favored representation. On the other hand, these are typically capable of only calculating ground states accurately. Furthermore, they assume that the number of electrons is held constant while open system problems require that the chemical potential be held constant but allow the number of electrons in the system to vary. Finally, although DFT approaches have been very successful in calculating the overall TD effects of the electron-electron repulsions, it is unclear as to whether the potential energy functionals will be able to properly characterize *energy resolved* effects.

NEGF approaches, on the other hand are not ground state methodologies. In NEGF, the electron density is traced over all possible states, including states of varying electron number. Furthermore, the theory is formulated in the grand canonical statistical picture ensuring that the chemical potential is held constant while the electron number is free to vary. Finally, NEGF is a two variable theory that can easily be reformulated in the energy resolved picture expressed above. This reformulation can also be performed to a great extent on the terms that simulate electron-electron

Figure 2.8: Plots of $n(E,t)$ (left) and $\mu(E,t)$ (right).

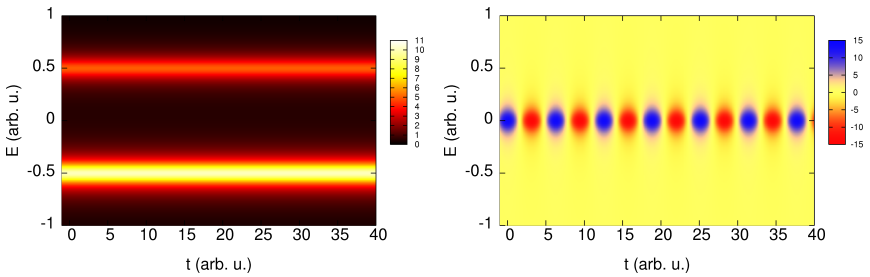

repulsion although a reformulation of this repulsive interaction is the topic of future work and will not be covered here. In NEGF theory, these terms are functionals of the energy resolved density described above.

For these reasons, the methodology derived and implemented here will be based on the NEGF formalism and applied to the problem of weak interacting potentials in the context of time dependent perturbation theory.

To conclude this chapter, it is worth mentioning a note on notation and units. First, the notation in the following chapters differs slightly from the notation used here and one should take note of these changes. The energy variable, E is replaced by $\bar{\omega}$ and the time variable t is replaced by $\bar{t}$. Second, the formalism is written in atomic units where Planck's constant, $\hbar$, and the fundamental unit of charge, e are both set equal to unity.

CHAPTER III

Contour Propagation and Many Body Formalism

3.1 Introduction: The Electronic Hamiltonian

We start with the many electron time-dependent Schrodinger equation:

$$i\frac{\partial}{\partial t}\Psi(\vec{r}_1,...,\vec{r}_n,t) = \hat{H}(\vec{r}_1,...,\vec{r}_n,t)\Psi(\vec{r}_1,...,\vec{r}_n,t). \tag{3.1}$$

Nuclear degrees of freedom are not explicitly stated because we are working within the Born-Oppenheimer approximation where the time-evolution of nuclear motion is orders of magnitude slower than the electron dynamics. In this regime, the electronic Hamiltonian can be decoupled from the nuclear Hamiltonian and the electronic states are assumed to depend parametrically on the nuclear degrees of freedom. This parametric dependence allows us to calculate electron dynamics for fixed nuclear degrees of freedom. The many-body Hamiltonian $\hat{H}(\vec{r}_1,...,\vec{r}_n,t)$ can be expressed in terms of two types of terms, namely, terms that depend only on one coordinate (one-body terms) and interaction terms that depend on two coordinates (two-body) terms,

$$\hat{H}(\vec{r}_1,...,\vec{r}_n,t) = \sum_{i=1}^{n}\hat{h}(\vec{r}_i,t) + \sum_{i=1}^{n}\sum_{j>i}\hat{v}(\vec{r}_i,\vec{r}_j). \tag{3.2}$$

Note that we assume that all time-dependence in the Hamiltonian takes a one-body form. Time dependent classical fields expressed in the dipole approximation meet this criterion. For electronic systems, the one-body terms include the electron kinetic

energy operators, electron-nuclear attraction terms and the applied time-dependent perturbation terms

$$\hat{h}(\vec{r},t) = -\frac{1}{2}\nabla^2_{\vec{r}} - \sum_I \frac{Z_I}{|\vec{r}-\vec{R}_I|} + E(t)\vec{r} \tag{3.3}$$

The two-body terms are the coulomb repulsion terms,

$$\hat{v}(\vec{r}_i,\vec{r}_j) = \frac{1}{|\vec{r}_i-\vec{r}_j|} \tag{3.4}$$

3.2 Propagator Theory And The Keldysh Contour

An open electronic system, such as a molecular junction, is a finite electronic system in contact with an electron reservoir at constant chemical potential (fermi energy) μ. Such a system can exchange electrons with the reservoir and the number of electrons within the system is generally not conserved. At thermal equilibrium, the system is described by a grand-canonical ensemble. The corresponding density and partition function are

$$\hat{\rho}_\circ = \exp[-\beta(\hat{H}-\mu\hat{N})]/Z,\ Z = Tr\{\hat{\rho}_\circ\}. \tag{3.5}$$

where $\hat{H}$ is the time-independent Hamiltonian for the total quantum system. The number operator, $\hat{N}$, commutes with $\hat{H}$. The eigenvalue of $\hat{N}$ is the number of electrons (occupied one-body orbitals) in the eigenstate of $\hat{H}$. The partition function Z traces the grand canonical density operator $\hat{\rho}_\circ$ over all possible numbers of electrons. At the initial steady state the trace ($Tr\{\hat{\rho}_\circ\hat{O}\}$) describes the expectation value of the operator ($\hat{O}$) for the unperturbed (isolated) system with the density operator $\hat{\rho}_\circ$ defined over a complete set of states in the Hilbert space.

We now consider the TD Schrodinger equation (TDSE) in the Heisenberg picture. Let $H(t)$ be the Hamiltonian of a system, which remains at equilibrium up to $t_\circ$, when

it is being perturbed:

$$\hat{H}(t < t_\circ) = \hat{H}_\circ. \tag{3.6}$$

The time evolution of the expectation value of $\hat{O}$ (for $t > t_\circ$) is

$$\begin{aligned} O(t) \equiv & Tr\{\hat{U}(t, t_\circ)\hat{\rho}_\circ \hat{U}(t_\circ, t)\hat{O}\} \\ = & Tr\{\hat{\rho}_\circ \hat{U}(t_\circ, t)\hat{O}\hat{U}(t, t_\circ)\} \\ = & Tr\{\hat{\rho}_\circ \hat{O}_H(t)\}, \end{aligned} \tag{3.7}$$

where $\hat{O}_H(t)$ is the Heisenberg representation of $\hat{O}$. The propagator, $\hat{U}(t, t')$ relates the solution of the TDSE at time t to time t'. It is generally expressed as a time-ordered exponential operator,

$$\begin{aligned} \hat{U}(t, t') = & \hat{T}\left[e^{-i\int_{t'}^{t} dt_1 \left(\hat{H}(t_1) - \mu\hat{N}\right)}\right] \\ = & \hat{1} + \sum_{n=1}^{\infty} \frac{(-i)^n}{n!} \int_{t'}^{t} dt_1 \cdots \int_{t'}^{t} dt_n \hat{T}\left[\hat{H}(t_1)\cdots\hat{H}(t_n)\right]. \end{aligned} \tag{3.8}$$

The time ordering operator $\hat{T}$ ensures that the Hamiltonian operators are positioned from left to right in reverse chronological order. Explicitly, the time ordering operator acting on a set of operators, $\hat{O}_n(t_n)$, can be expressed as follows,

(3.9)

$$\begin{aligned} \hat{T}\left[\hat{O}_1(t_1)\cdots\hat{O}_n(t_n)\right] \equiv & \sum_P \Theta(t_{P(1)} - t_{P(2)})\Theta(t_{P(2)} - t_{P(3)})\cdots\Theta(t_{P(n-1)} - t_{P(n)})\times \\ & \hat{O}_{P(1)}(t_{P(1)})\cdots\hat{O}_{P(n)}(t_{P(n)}). \end{aligned}$$

The sum in eqn. 3.9 is taken over all possible permutation functions, $P(n)$ that map each index in the set $\{1...n\}$ to a given permutation of this set. Each term in the sum has $n-1$ Heaviside step functions $\Theta(t)$ and n time dependent operators $\hat{O}(t)$.

The exponential operator in $\hat{\rho}_\circ$ (eqn. 3.5) can be rewritten as a time-evolution

operator, $\hat{U}$, evaluated on a complex temporal coordinate.

$$
\begin{aligned}
e^{-\beta(\hat{H}_\circ-\mu\hat{N})} = & \\
& e^{-i(\hat{H}_\circ-\mu\hat{N})(-i\beta)} \\
=& e^{-i(\hat{H}_\circ-\mu\hat{N})(t_\circ-i\beta-t_\circ)} \\
=& e^{-i(\hat{H}_\circ-\mu\hat{N})(\int_{t_\circ}^{t_\circ-i\beta} dt_1)} \\
=& \hat{T}_I\left[e^{-i(\int_{t_\circ}^{t_\circ-i\beta} dt_1(\hat{H}(t_1)-\mu\hat{N}))}\right] \\
=& \hat{U}(t_\circ - i\beta, t_\circ)
\end{aligned}
\tag{3.10}
$$

where the total Hamiltonian, $\hat{H}(t)$ is simply extended (analytically continued) onto the complex plain. To ensure that this continuation leads to an analytical Hamiltonian on the complex plane, $\hat{H}(t)$ is conveniently set to the initial time Hamiltonian $H_\circ$ for complex times between $t_\circ$ and $t_\circ - i\beta$. The time ordering operator, $\hat{T}_I$, is defined in a manner analogous to eqn. 3.9.

(3.11)

$$
\begin{aligned}
\hat{T}_I\left[\hat{O}_1(t_1)\cdots\hat{O}_n(t_n)\right] \equiv & \\
& \sum_P \Theta(\tau_{P(1)}-\tau_{P(2)})\Theta(\tau_{P(2)}-\tau_{P(3)})\cdots\Theta(\tau_{P(n-1)}-\tau_{P(n)})\times \\
& \hat{O}_{P(1)}(\tau_{P(1)})\cdots\hat{O}_{P(n)}(\tau_{P(n)}).
\end{aligned}
$$

for times $t_0 - i\tau$ where $0 \leq \tau \leq \beta$. Thus, the expression for $O(t)$ becomes,

$$
O(t) = \frac{Tr\{\hat{U}(t_0 - i\beta, t_0)\hat{U}(t_0, t)\hat{O}\hat{U}(t, t_0)\}}{Tr\{\hat{U}(t_0 - i\beta, t_0)\}}. \tag{3.12}
$$

One can interpret the j-th element (state) within the trace in the numerator of eqn. 3.12 by

$$
\langle E_j, N_j|\{\hat{U}(t_0 - i\beta, t_0)\hat{U}(t_0, t)\hat{O}\hat{U}(t, t_0)\}|E_j, N_j\rangle. \tag{3.13}
$$

This amounts to five steps. First, the ket, $|E_j, N_j\rangle$ is propagated from t_0 to t by $\hat{U}(t, t_0)$. Second, this propagated result is transformed in Hilbert space by the operator $\hat{O}$. Third, this transformed ket vector is propagated back to t_0 by $\hat{U}(t_0, t)$ and, fourth, propagated onto the complex plane by $\hat{U}(t_0 - i\beta, t_0)$. Fifth, this final result is projected onto the state represented by the bra vector, $\langle E_j, N_j|$, in eqn. 3.13. The temporal path of steps one through four is a contour C on the complex plane (fig. 3.1), where the branch from t_0 to t is distinguished from the t to t_0 branch by application of the operator $\hat{O}$. At this point $\hat{O}$ is relabeled as $\hat{O}_t$ to indicate the time at which $\hat{O}$ is applied. The contour C is referred to as the Keldysh contour (KC)[59]. The KC relates a dynamic electronic system experiencing a time-dependent perturbation to its thermally equilibrated initial state.

A contour ordering operator $\hat{T}_C$ is defined in order to combine the separate propagators in eqn. 3.12 and to derive a single equation of motion in terms of a complex time variable on the KC.

(3.14)

$$\hat{T}_C\left[\hat{O}_1(t_1)\cdots\hat{O}_n(t_n)\right] \equiv \sum_P \Theta_C(t_{P(1)}, t_{P(2)})\Theta_C(t_{P(2)}, t_{P(3)})\cdots\Theta_C(t_{P(n-1)}, t_{P(n)})\times \hat{O}_{P(1)}(t_{P(1)})\cdots\hat{O}_{P(n)}(t_{P(n)}).$$

The complex contour step function $\Theta_C(t_1, t_2)$ is one if t_1 is at the same point as t_2 or if t_1 is closer to the end point $t_0 - i\beta$ on the KC. It is zero otherwise. The permutation function, P, retains the same definition as for the case of the time ordering operator $\hat{T}$. This operator is analogous to the time ordering operator. However, it arranges operators from left to right in order of increasing temporal distance from $t_0 - i\beta$ *along the contour*. Thus, a point in time t_1 may be farther away from the end of the contour $t_0 - i\beta$ than a point t_2, even though t_1 may fall chronologically after t_2

Figure 3.1: The Keldysh Contour.

on the real time axis. The propagators in eqn. 3.12 are now combined into a single contour ordered operator (see appendix A),

$$O(t) = \frac{Tr\{\hat{T}_C \left[e^{-i\int_C dt_1(\hat{H}(t_1)-\mu\hat{N})}\hat{O}_t\right]\}}{Tr\{\hat{U}(t_0 - i\beta, t_0)\}}. \tag{3.15}$$

where the integral operator $\int_C dt$ is a path integral over the KC, and t is a complex time variable on the KC. Furthermore (appendix A), this expectation value can be written in terms of KC propagators, $\hat{U}_C(t, t')$,

$$O(t) = \frac{Tr\{\hat{T}_C \left[\hat{U}_C(t_0 - i\beta, t_0)\hat{U}_C(t_0, t)\hat{O}_t\hat{U}_C(t, t_0)\right]\}}{Tr\{\hat{U}_C(t_0 - i\beta, t_0)\}}. \tag{3.16}$$

where,

$$\begin{aligned}\hat{U}_C(t, t') = & \\ & \hat{T}_C \left[e^{-i\int_{C_{t'\to t}} dt_1\left(\hat{H}(t_1)-\mu\hat{N}\right)t_1}\right] \\ & = \hat{1} + \sum_{n=1}^{\infty} \frac{(-i)^n}{n!} \int_{C_{t'\to t}} dt_1 \cdots \int_{C_{t'\to t}} dt_n \hat{T}_C \left[\hat{H}(t_1)\cdots\hat{H}(t_n)\right].\end{aligned} \tag{3.17}$$

and $\int_{C_{t'\to t}} dt_1$ is a path integral on the KC over the portion between t' and t.

Equilibrium vs. Non-equilibrium theory

The difference between an equilibrium theory and a non-equilibrium theory is a fundamental one. In equilibrium theory it is assumed that a system's final state will

be identical to its initial state. This assumption is not made in the non equilibrium picture. In calculating the dynamical expectation value of an operator (eq. 3.7), an equilibrium theory assumes that the system ends in the same state in which it began. Thus, $\hat{U}(t_\circ, t)$ has the same effect on the density operator at t as $\hat{U}(t_f, t)$, where t_f is the final time, and

$$O(t) = Tr\{\hat{\rho}_\circ \hat{U}(t_f, t)\hat{O}\hat{U}(t, t_\circ)\}, \tag{3.18}$$

allowing for the replacement of the contour ordering propagator with the time ordering propagator. The Gellmann-Lowe theorem[44] ensures that this is the case at $t_f \to \infty$ for a density operator defined by the pure ground state at $t_\circ \to -\infty$, namely $\hat{\rho}_\circ = |\Psi_\circ\rangle\langle\Psi_\circ|$. However, in quantum statistical systems, the equilibrium assumption does not generally hold and it is necessary to develop a formalism that does not depend on it. One must then retain the original propagator $\hat{U}(t_\circ, t)$ and resort to contour ordering.

3.3 Electron Book Keeping: Second Quantization

The purpose of second quantization is to reduce the many-body problem to an effective one-body problem while preserving the symmetry properties, and consequently, statistics of the particles. In the context of electronic structure theory for isolated systems, the electronic properties are described entirely by the many-electron state function, a function of the position and spin coordinates of all of the electrons. Second quantization allows these properties to be represented in terms of one set of space-spin coordinates while preserving the anti-symmetric nature of the many-electron state and the resulting Fermi-Dirac statistics. There are several very useful consequences of this representation that will be demonstrated in the sections below. First, the many-electron wave function, with its large set of space-spin

coordinates will be replaced by an electronic charge density expressed in terms of the absolute space-spin coordinates of the molecular system. Second, a direct formal expression for the electron number operator, $\hat{N}$, is obtained. Third, the second quantized representation retains the same form independent of change in the number of electrons in the system. The second and third points may seem insignificant for isolated molecules because $\hat{N}$ does not change. However, for an open system, such as a molecular junction, this number is not conserved and can change. Thus, second quantization becomes a formally very useful approach to handling a molecule with changing number of electrons.

This chapter does not present a full derivation of the second quantized representation of electronic structure. It provides a motivation for the use of such a representation by 'sketching' the steps that one would use to transform a many-electron state representation into a second quantized representation. A detailed derivation of the second quantized representation may be found in chapter 1 of ref. [44].

The expectation value of an N-electron operator, $\hat{O}(\mathbf{x}_1, ..., \mathbf{x}_N)$, (written in terms of the electrons' space-spin coordinates $\mathbf{x}_s$) can be expressed as

$$\langle \hat{O}(t) \rangle = \int ... \int \mathbf{d^4 x}_1 ... \mathbf{d^4 x}_N \Psi^*(\mathbf{x}_1, ..., \mathbf{x}_N, t) \hat{O}(\mathbf{x}_1, ..., \mathbf{x}_N) \Psi(\mathbf{x}_1, ..., \mathbf{x}_N, t) \tag{3.19}$$

where the integrals are over a total of four components (three spatial and one spin). Without loss of generality, a dynamic many-electron wave packet, $\Psi(\mathbf{x}_1, ..., \mathbf{x}_N, t)$ may be expanded as a linear combination of slater determinants of one-electron

orbitals, $\psi_i(\mathbf{x}_s)$ (s-th electron, i-th orbital energy level),

$$\begin{aligned}\Psi(\mathbf{x}_1,...,\mathbf{x}_N,t) = & \\ & \sum_{E_n} C_n(t)\Psi_{E_n}(\mathbf{x}_1,...,\mathbf{x}_N) \\ = & \sum_{E_n} \frac{C_n(t)}{\sqrt{N!}} \mathbf{det}\left(\begin{bmatrix} \psi_{\epsilon_j}(\hat{\mathbf{x}_1}) & \dots & \psi_{\epsilon_k}(\hat{\mathbf{x}_1}) \\ \vdots & \ddots & \vdots \\ \psi_{\epsilon_j}(\hat{\mathbf{x}_N}) & \dots & \psi_{\epsilon_k}(\hat{\mathbf{x}_N}) \end{bmatrix}\right).\end{aligned} \tag{3.20}$$

where the one-electron orbitals ψ_{ϵ_j} are occupied within the many electron eigenstate $\Psi_{E_n}(\mathbf{x}_1,...,\mathbf{x}_N)$ with energy E_n and occupation number N. In the second quantized representation, a given eigenstate $\Psi_{E_n}(\mathbf{x}_1,...,\mathbf{x}_N)$ is replaced by an abstract ket-vector $|E_n; n_i...n_j...n_k\rangle$ where n_i is the occupation number of the i-th single electron orbital, ψ_{ϵ_i} (0 or 1 for electrons). In this representation, eqn. 3.19 takes a form similar to,

$$\begin{aligned}\langle\hat{O}(t)\rangle = & \\ & \int ... \int \mathbf{d^4x}_1...\mathbf{d^4x}_N \Psi^*(\mathbf{x}_1,...,\mathbf{x}_N,t)\hat{O}(\mathbf{x}_1,...,\mathbf{x}_N)\Psi(\mathbf{x}_1,...,\mathbf{x}_N,t) \\ = & \sum_{m,n} \int ... \int \mathbf{d^4x}_1...\mathbf{d^4x}_N C_m^*(t)C_n(t)\times \\ & \Psi^*_{E_m}(\mathbf{x}_1,...,\mathbf{x}_N)\hat{O}(\mathbf{x}_1,...,\mathbf{x}_N)\Psi_{E_n}(\mathbf{x}_1,...,\mathbf{x}_N) \\ = & \sum_{m,n} C_m^*(t)C_n(t)\times \\ & \langle E_m; n_i...n_j...n_k| \left(\int \mathbf{d^4x}\hat{O}(\mathbf{x})\right) |E_n; n'_i...n'_j...n'_k\rangle\end{aligned} \tag{3.21}$$

where the number of spin-space coordinates has been reduced to one set, $\mathbf{x}$.

3.3.1 Non-interacting operators

To motivate this, we first look at a general non-interacting operator,

$$\hat{O}(\mathbf{x_1},...,\mathbf{x_N}) = \sum_{s=1}^{N} \hat{o}(\mathbf{x_s},t) \tag{3.22}$$

Most operators of interest can be expressed in this form, including the number operator and the non-interacting Hamiltonian. Examples will be given below. A slater determinant can be written as a sum of products of one-body orbitals,

$$\mathbf{det}\left(\begin{bmatrix} \psi_{\epsilon_j}(\hat{\mathbf{x}_1}) & \dots & \psi_{\epsilon_k}(\hat{\mathbf{x}_1}) \\ \vdots & \ddots & \vdots \\ \psi_{\epsilon_j}(\hat{\mathbf{x}_N}) & \dots & \psi_{\epsilon_k}(\hat{\mathbf{x}_N}) \end{bmatrix}.\right) = \sum_P (-1)^{N_P} \psi_{P(\epsilon_j)}(\hat{\mathbf{x}_1}) ... \psi_{P(\epsilon_k)}(\hat{\mathbf{x}_N}) \tag{3.23}$$

where the sum is carried out over all possible permutations P of the orbital energy indices ϵ_j and N_P is the number of interchanges required to take the product back to its canonical order $\psi_{\epsilon_j}(\hat{\mathbf{x}_1}) ... \psi_{\epsilon_k}(\hat{\mathbf{x}_N})$ as expressed by multiplying the orbitals along the diagonal of the slater matrix. in order. Hence, the expectation value of a many particle operator can be decomposed into a linear combination of terms of the form,

$$\begin{aligned} \int ... \int \mathbf{d^4 x}_1 ... \mathbf{d^4 x}_N \psi^*_{\epsilon_i}(\mathbf{x}_1) \cdots \psi^*_{\epsilon_j}(\mathbf{x}_s) \cdots \psi^*_{\epsilon_k}(\mathbf{x}_N) \hat{O}(\mathbf{x}_1, ..., \mathbf{x}_N) \times \\ \psi_{\epsilon'_i}(\mathbf{x}_1) \cdots \psi_{\epsilon'_j}(\mathbf{x}_s) \cdots \psi_{\epsilon'_k}(\mathbf{x}_N) \end{aligned} \tag{3.24}$$

Substituting eqn. 3.22 into eqn. 3.24 transforms eqn. 3.24 into the following form.

$$\begin{aligned} &\int ... \int \mathbf{d^4 x}_1 ... \mathbf{d^4 x}_N \psi^*_{\epsilon_i}(\mathbf{x}_1) \cdots \psi^*_{\epsilon_j}(\mathbf{x}_s) \cdots \psi^*_{\epsilon_k}(\mathbf{x}_N) \hat{O}(\mathbf{x}_1, ..., \mathbf{x}_N) \times \\ &\quad \psi_{\epsilon'_i}(\mathbf{x}_1) \cdots \psi_{\epsilon'_j}(\mathbf{x}_s) \cdots \psi_{\epsilon'_k}(\mathbf{x}_N) \\ &= \sum_{s=1}^{N} \int \mathbf{d^4 x}_s \psi^*_{\epsilon_j}(\mathbf{x}_s) \hat{o}(\mathbf{x}_s) \psi_{\epsilon'_j}(\mathbf{x}_s) \times \\ &\quad \int ... \int \mathbf{d^4 x}_1 ... \mathbf{d^4 x}_N [\psi^*_{\epsilon_i}(\mathbf{x}_1) \cdots \psi^*_{\epsilon_{j_-}}(\mathbf{x}_{s-1}) \psi^*_{\epsilon_{j_+}}(\mathbf{x}_{s+1}) \cdots \psi^*_{\epsilon_k}(\mathbf{x}_N) \times \\ &\quad \psi_{\epsilon'_i}(\mathbf{x}_1) \cdots \psi_{\epsilon'_{j_-}}(\mathbf{x}_{s-1}) \psi_{\epsilon'_{j_+}}(\mathbf{x}_{s+1}) \cdots \psi_{\epsilon'_k}(\mathbf{x}_N)] \end{aligned} \tag{3.25}$$

The factor $\int \psi^*_{\epsilon_j} \hat{0} \psi_{\epsilon'_j}$ in the last term of eqn. 3.25 is a one-body integral. For a given term $\int \Psi_{E_m} \hat{O} \Psi_{E_n}$ in eqn. 3.21, every product of the form eqn. 3.25 will produce such a one body integral with the specific indices j and j', but over differing values of the index s. However, the variable of integration in such integrals is a dummy

variable and, thus, all of the terms of the form eqn. 3.25 that compose the term $\int \Psi_{E_m} \hat{O} \Psi_{E_n}$ can be gathered together and written using the abstract ket vectors, $|E_n; n_i ... n_j ... n_k\rangle$ as follows.

(3.26)

$$\begin{aligned}
&\int ... \int \mathbf{d^4 x}_1 ... \mathbf{d^4 x}_N \Psi^*_{E_m}(\mathbf{x}_1, ..., \mathbf{x}_N) \hat{O}(\mathbf{x}_1, ..., \mathbf{x}_N) \Psi_{E_n}(\mathbf{x}_1, ..., \mathbf{x}_N) \\
&\quad = \int \mathbf{d^4 x} \psi^*_{\epsilon_j}(\mathbf{x}) \hat{o}(\mathbf{x}) \psi_{\epsilon'_j}(\mathbf{x}) \langle n_i ... n_{j_-} n_{j_+} ... n_k | n'_i ... n'_{j_-} n'_{j_+} ... n'_k \rangle \\
&\quad = \langle E_m; n_i ... n_{j_-} n_{j_+} ... n_k | \left(\int \mathbf{d^4 x} \psi^*_{\epsilon_j}(\mathbf{x}) \hat{o}(\mathbf{x}) \psi_{\epsilon'_j}(\mathbf{x}) \right) | E_n; n'_i ... n'_{j_-} n'_{j_+} ... n'_k \rangle
\end{aligned}$$

where the indices j_- and j_+ refer to the orbitals that originally came immediately before and after the j-th orbital, $\psi^*_{\epsilon_j}(\mathbf{x}_s)$, respectively. This inner product must now be rewritten to correspond to the original states $|E_n; n_i ... n_j ... n_k\rangle$ (i.e. states that include the orbitals ψ_{ϵ_j}, $\psi_{\epsilon'_j}$. To this end, we note that

$$|E_n; n_i ... n_{j_-} n_{j_+} ... n_k\rangle = \hat{a}_j |E_n; n_i ... n_j ... n_k\rangle \tag{3.27}$$

where $\hat{a}_j$ is an operator that removes the orbital ψ_{ϵ_j} from a state Ψ_{E_m} if it exists. If it does not exist, it annihilates the entire state,

$$\hat{a}_j |E_n; n_i ... n_{j_-} n_{j_+} ... n_k\rangle = 0 \tag{3.28}$$

Likewise, the conjugate transpose of $\hat{a}_j$, $\hat{a}^\dagger_j$ adds the orbital ψ_{ϵ_j} to a state that does not have it

$$|E_n; n_i ... n_j ... n_k\rangle = \hat{a}^\dagger_j |E_n; n_i ... n_{j_-} n_{j_+} ... n_k\rangle \tag{3.29}$$

and annihilates a state that does possess it,

$$\hat{a}^\dagger_j |E_n; n_i ... n_j ... n_k\rangle = 0 \tag{3.30}$$

These addition and removal operators and the properties (shown above) that allow them to preserve the Pauli exclusion principle, lead to the following anti-commutation relations [44],

$$\{\hat{a}_i, \hat{a}_j\} = \{\hat{a}_i^\dagger, \hat{a}_j^\dagger\} = 0 \tag{3.31}$$

$$\{\hat{a}_i, \hat{a}_j^\dagger\} = \delta_{ij} \tag{3.32}$$

The fact that the relations are anti-commutative is intuitively expected since permuting two orbitals within a state Ψ_{E_n} causes a π phase shift in the state. Hence, all Fermi-Dirac statistics are elegantly captured by these anti-commutation relations. Using these operators, eqn. 3.26 can be written as,

$$\begin{aligned}\int ... \int \mathbf{d^4 x}_1 ... \mathbf{d^4 x}_N \Psi^*_{E_m}(\mathbf{x}_1, ..., \mathbf{x}_N) \hat{O}(\mathbf{x}_1, ..., \mathbf{x}_N) \Psi_{E_n}(\mathbf{x}_1, ..., \mathbf{x}_N) \\ = \langle E_m; n_i ... n_j ... n_k | \left(\int \mathbf{d^4 x} \psi^*_{\epsilon_j}(\mathbf{x}) \hat{a}_j^\dagger \hat{o}(\mathbf{x}) \psi_{\epsilon'_j}(\mathbf{x}) \hat{a}_j \right) | E_n; n'_i ... n'_j ... n'_k \rangle\end{aligned} \tag{3.33}$$

This procedure can be carried out for all values of j and j' giving a field operator representation for $\hat{O}$ in the abstract Hilbert space of states $|E_n; n_i ... n_j ... n_k\rangle$, of the form,

$$\hat{O} = \int \mathbf{d^4 x} \hat{\psi}^\dagger(\mathbf{x}) o(\mathbf{x}) \hat{\psi}(\mathbf{x}) \tag{3.34}$$

where,

$$\hat{\psi}(\mathbf{x}) = \sum_{j=1}^{\infty} \psi_{\epsilon_j}(\mathbf{x}) \hat{a}_j \tag{3.35}$$

In summary, replacing the state $\Psi_{E_n}(\mathbf{x}_1, ..., \mathbf{x}_N)$ by $|E_n; n_i ... n_j ... n_k\rangle$ requires replacement of the operator $\hat{O}(\mathbf{x}_1, ..., \mathbf{x}_N)$ by $\hat{O}$ as defined in eqn. 3.34. These field operators have anti-commutation relations similar to (and readily derivable from) equations3.31, 3.32

$$\{\hat{\psi}(\mathbf{x}), \hat{\psi}(\mathbf{x}')\} = \{\hat{\psi}^\dagger(\mathbf{x}), \hat{\psi}^\dagger(\mathbf{x}')\} = 0 \tag{3.36}$$

$$\{\hat{\psi}(\mathbf{x}), \hat{\psi}^{\dagger}(\mathbf{x}')\} = \delta(\mathbf{r} - \mathbf{r}')\delta_{\alpha,\alpha'} \tag{3.37}$$

where the space-spin coordinates $\mathbf{x}_1$, $\mathbf{x}_2$ have been divided into their respective spatial and spin parts, $\mathbf{r}$, $\mathbf{r}'$ and α, α'. We now show several examples of important non-interacting operators.

Number Density Operator

The number density operator for a system of N electrons, each at a position $\vec{r}_n$, is

$$\hat{n}(\mathbf{x}_1, ...\mathbf{x}_N) = \sum_{n=1}^{N} \delta(\vec{r}_n - \vec{r}). \tag{3.38}$$

The expectation value of $\hat{n}$ is the dynamic electron number density,

$$\begin{aligned} \langle \hat{n}(t) \rangle = & \\ & \int ... \int \mathbf{d^4 x}_1 ... \mathbf{d^4 x}_N \Psi^*(\mathbf{x}_1, ..., \mathbf{x}_N, t) \hat{n}(\mathbf{x}_1, ..., \mathbf{x}_N) \Psi(\mathbf{x}_1, ..., \mathbf{x}_N, t) \\ & = \sum_{m,n} C_m^*(t) C_n(t) \psi_{\epsilon_m}^*(\mathbf{r}) \psi_{\epsilon_n}^*(\mathbf{r}) \delta_{\alpha_m, \alpha_n} \end{aligned} \tag{3.39}$$

The scalar part of the second quantized representation of this operator, becomes

$$n(\mathbf{x}') = \delta(\vec{r}' - \vec{r}) \tag{3.40}$$

and the second quantized representation is itself,

$$\hat{n}(\mathbf{r}) = \int \mathbf{d^4 x}' \hat{\psi}^{\dagger}(\mathbf{x}') \delta(\vec{r}' - \vec{r}) \hat{\psi}(\mathbf{x}') = \hat{\psi}_{\uparrow}^{\dagger}(\mathbf{r}) \hat{\psi}_{\uparrow}(\mathbf{r}) + \hat{\psi}_{\downarrow}^{\dagger}(\mathbf{r}) \hat{\psi}_{\downarrow}(\mathbf{r}) \tag{3.41}$$

where, for example, $\hat{\psi}_{\downarrow}(\mathbf{r})$ is the field operator summing over all spatial orbitals with spin $-1/2$,

$$\hat{\psi}_{\downarrow}(\mathbf{r}) = \sum_{j=1}^{\infty} \psi_{\epsilon_j, \downarrow}(\mathbf{r}) \hat{a}_{j,\downarrow} \tag{3.42}$$

An explicit form for the number operator $\hat{N}$ is now attainable,

$$\hat{N} = \int \mathbf{d^3 r} \hat{n}(\mathbf{r}) = \sum_{j=1}^{N} \left[\hat{a}_{j\uparrow}^{\dagger} \hat{a}_{j\uparrow} + \hat{a}_{j\downarrow}^{\dagger} \hat{a}_{j\downarrow} \right] \tag{3.43}$$

which is very instrumental in explicitly expressing the grand-canonical density operator and its formal consequences.

Current Density Operator

The current density operator is given by,

$$\hat{\mathbf{j}}(\mathbf{x}_1, ..., \mathbf{x}_N) = -i \sum_{j=1}^{N} \left[\nabla_{\mathbf{r}_j} \delta(\mathbf{r}_j - \mathbf{r}) + \delta(\mathbf{r}_j - \mathbf{r}) \vec{\nabla}_{\mathbf{r}_j} \right]. \tag{3.44}$$

The scalar part of the second quantized operator is,

$$\mathbf{j}(\mathbf{x}) = -i \left[\nabla_{\mathbf{r}'} \delta(\mathbf{r}' - \mathbf{r}) + \delta(\mathbf{r}' - \mathbf{r}) \vec{\nabla}_{\mathbf{r}'} \right]. \tag{3.45}$$

and the second quantized form is,

$$\begin{aligned} \hat{\mathbf{j}} = & \\ & - i \int \mathbf{d^4 x'} \hat{\psi}^{\dagger}(\mathbf{x'}) \left[\nabla_{\mathbf{r}'} \delta(\mathbf{r}' - \mathbf{r}) + \delta(\mathbf{r}' - \mathbf{r}) \vec{\nabla}_{\mathbf{r}'} \right] . \hat{\psi}(\mathbf{x}') \\ = & i \sum_{\alpha = \uparrow, \downarrow} \left[\left(\nabla_{\mathbf{r}} \hat{\psi}_{\alpha}^{\dagger}(\mathbf{r}) \right) \hat{\psi}_{\alpha}(\mathbf{r}) - \hat{\psi}_{\alpha}^{\dagger}(\mathbf{r}) \left(\vec{\nabla}_{\mathbf{r}} \hat{\psi}_{\alpha}(\mathbf{r}) \right) \right]. \end{aligned} \tag{3.46}$$

The final term in eqn. 3.46 is expressed in terms of spatial field operators (eqn. 3.42) and presents an alternative way of writing the scalar portion of the current density operator that will be useful in later chapters, namely,

$$\mathbf{j}(\mathbf{x}, \mathbf{x}') = i \delta \mathbf{r} - \mathbf{r}_0 \lim_{\mathbf{r}' \to \mathbf{r}} \left[\nabla_{\mathbf{r}'} - \vec{\nabla}_{\mathbf{r}} \right]. \tag{3.47}$$

where the primed gradient acts on the electron addition field operator, $\hat{\psi}^{\dagger}$, the unprimed gradient acts on the electron removal operator, $\hat{\psi}$ and the current density is given at $\mathbf{r}_0$.

Dipole operator

The dipole operator is given by,

$$\hat{\mu}(\mathbf{x}_1, ..., \mathbf{x}_N, t) = \sum_{j=1}^{N} \hat{\mathbf{r}}_j \tag{3.48}$$

The scalar portion of the second quantized represented dipole operator is,

$$\mu(\mathbf{x}) = \mathbf{r} \tag{3.49}$$

The second quantized representation is,

$$\hat{\mu} = \sum_{\alpha=\uparrow,\downarrow} \int d^3r' \hat{\psi}^{\dagger}_{\alpha}(\mathbf{r}) \mathbf{r} \hat{\psi}_{\alpha}(\mathbf{r}) \tag{3.50}$$

Non-Interacting Hamiltonian

A non-interacting many-electron Hamiltonian with a time-dependent classical driving potential of the form

$$\hat{v}(\mathbf{x}_1, ..., \mathbf{x}_N, t) = v(t) \sum_{j=1}^{N} \hat{f}(\mathbf{r}_j) \tag{3.51}$$

can be expressed as,

$$\hat{h}(\mathbf{x}_1, ..., \mathbf{x}_N, t) = \sum_{I=1}^{N} \left[-\frac{1}{2} {\nabla_{\mathbf{r_i}}}^2 - \sum_{I} \frac{Z_I}{|\mathbf{r}_i - \mathbf{R}_I|} + v(t) \hat{f}(\mathbf{r}_j) \right] \tag{3.52}$$

where the index I runs over the $\mathbf{R}_I$ nuclear coordinates. The scalar portion of the second quantized Hamiltonian is the one-electron Hamiltonian.

$$h(\mathbf{x}) = -\frac{1}{2} {\nabla_{\mathbf{r}}}^2 - \sum_{I} \frac{Z_I}{|\mathbf{r} - \mathbf{R}_I|} + v(t) \hat{f}(\mathbf{r}) \tag{3.53}$$

This fact will allow for the reduction of the many-body time-dependent equations of motion into effective one-body equations of motion. The second quantized representation is,

$$\hat{h} = \sum_{\alpha=\uparrow,\downarrow} \int d^3r' \hat{\psi}^{\dagger}_{\alpha}(\mathbf{r}) \left[-\frac{1}{2} {\nabla_{\mathbf{r}}}^2 - \sum_{I} \frac{Z_I}{|\mathbf{r} - \mathbf{R}_I|} + v(t) \hat{f}(\mathbf{r}) \right] \hat{\psi}_{\alpha}(\mathbf{r}) \tag{3.54}$$

3.3.2 Pairwise Interacting Operators

Pairwise interacting operators take the form,

$$\hat{O}(\mathbf{x_1}, ..., \mathbf{x_N}) = \sum_{s=1}^{N} \sum_{t \geq s} \hat{o}(\mathbf{x_s}, \mathbf{x_t}) \tag{3.55}$$

where there is an interaction between every two particles. The most common example of a pairwise operator in the context of electronic structure is the coulomb repulsion between electrons, described by,

$$\hat{o}(\mathbf{x}_1, \mathbf{x}_2) = \frac{2}{|\mathbf{r}_1 - \mathbf{r}_2|} \tag{3.56}$$

Note that the electron repulsion operator does not depend on the spin coordinates. The procedure for constructing a second quantized representation of a pairwise interacting operator is an extension of the procedure for a non-interacting operator 3.3.1. Only now, a pair of electronic orbitals is pulled from each state Ψ_{E_n} (instead of a single orbital). The field operator representation for a pairwise interacting operator thus becomes,

$$\hat{O} = \int \mathbf{d^4 x}_1 \int \mathbf{d^4 x}_2 \hat{\psi}^\dagger(\mathbf{x}_2) \hat{\psi}^\dagger(\mathbf{x}_1) \hat{o}(\mathbf{x}_1, \mathbf{x}_2) \hat{\psi}(\mathbf{x}_1) \hat{\psi}(\mathbf{x}_2) \tag{3.57}$$

Total Hamiltonian

Thus, the total Hamiltonian can be written as,

$$\hat{H}(t) = \int d\vec{x} \hat{\Psi}^\dagger(\vec{x}) h(\vec{x}, t) \hat{\Psi}(\vec{x}) + \int d\vec{x} \int d\vec{x}' \hat{\Psi}^\dagger(\vec{x}) \hat{\Psi}^\dagger(\vec{x}') J(\vec{x}, \vec{x}') \hat{\Psi}(\vec{x}) \hat{\Psi}(\vec{x}'). \tag{3.58}$$

In this expression J corresponds to two-particle interactions and h is the one particle Hamiltonian, which includes the kinetic energy and a possible time-dependent applied external perturbation ($v(\vec{x}, t)$).

3.3.3 Field Operators in the Heisenberg Representation

Finally, the field operators can, like all other operators, be expressed in the Heisenberg picture. This is the picture in which the Green function is defined. In our case however, the temporal variable, t, is defined on the KC and derivatives with respect to t are taken on the KC.

$$\hat{\psi}_H(x) = \hat{U}_C(t_0, t)\hat{\psi}(\mathbf{x})\hat{U}_C(t, t_0) \tag{3.59}$$

$$\hat{\psi}^\dagger_H(x) = \hat{U}_C(t_0, t)\hat{\psi}^\dagger(\mathbf{x})\hat{U}_C(t, t_0) \tag{3.60}$$

where $x = (\mathbf{x}, t)$. The Heisenberg equations of motion remain the same for the KC as for the real time axis.

$$i\frac{\partial}{\partial t}\hat{\psi}_H(x) = \hat{U}_C(t_0, t)\left[\hat{\psi}(\mathbf{x}), \hat{H}(t)\right]\hat{U}_C(t, t_0) \tag{3.61}$$

$$i\frac{\partial}{\partial t}\hat{\psi}^\dagger_H(x) = \hat{U}_C(t_0, t)\left[\hat{\psi}^\dagger(\mathbf{x}), \hat{H}(t)\right]\hat{U}_C(t, t_0) \tag{3.62}$$

One can apply the Heisenberg equations of motion to the total Hamiltonian (eqn. 3.58). Using the anti-commutation relations for field operators (eqn. 3.36, 3.37) and the assumption that $J(\mathbf{x}_1, \mathbf{x}_2) = J(\mathbf{x}_2, \mathbf{x}_1)$, these equations of motion become,

$$i\frac{\partial}{\partial t}\hat{\psi}_H(x) = h(x)\hat{\psi}_H(x) + \int \mathbf{d^4x'}J(\mathbf{x}, \mathbf{x}')\hat{\psi}^\dagger_H(x')\hat{\psi}_H(x')\hat{\psi}_H(x) \tag{3.63}$$

$$i\frac{\partial}{\partial t}\hat{\psi}^\dagger_H(x) = -h(x)\hat{\psi}^\dagger_H(x) - \int \mathbf{d^4x'}J(\mathbf{x}, \mathbf{x}')\hat{\psi}^\dagger_H(x)\hat{\psi}^\dagger_H(x')\hat{\psi}_H(x') \tag{3.64}$$

CHAPTER IV

The one body Green Function

4.1 Definitions

The central quantities of Keldysh and NEGF formalisms are the one-body Green Functions (GF)[44, 57, 18] or propagators, which are functions of two space-spin and time coordinates ($x = \vec{x}, t$), with time variables defined on the Keldysh contour (KC) shown in figure 3.1). The two variable nature of these functions will allow for the energy resolved characterization of the system as described in chapter I. The need for the two variables is also a direct consequence of the nature of the electronic structure, which involves two body electrostatic Coulomb interactions. These two time variables are ordered on the contour, where their relative positions determine the type of GF. The propagators are defined by the pair of field operators ($\hat{\psi}(\mathbf{x})$ and $\hat{\psi}^{\dagger}(\mathbf{x}')$) at times t and t' respectively:

$$\begin{aligned} G(x,x') &\equiv -i\frac{\sum_n \langle E_n, N_n|\hat{U}_C(t_0 - i\beta, t_0)\hat{\mathcal{T}}_C[\hat{\psi}_H(x)\hat{\psi}^{\dagger}_H(x')]|E_n, N_n\rangle}{\sum_n \langle E_n, N_n|\hat{U}_C(t_0 - i\beta, t_0)|E_n, N_n\rangle} \\ &= -i\frac{Tr[\hat{U}_C(t_0 - i\beta, t_0)\hat{\mathcal{T}}_C[\hat{\psi}_H(x)\hat{\psi}^{\dagger}_H(x')]]}{Tr[\hat{U}_C(t_0 - i\beta, t_0)]} \end{aligned} \tag{4.1}$$

where the trace $Tr[...]$ is taken over all states $|E_n, N_n\rangle = |E_n; n_i \cdots n_j \cdots n_k\rangle$ with state energy E_n and occupation number N_n. In the Heisenberg picture, these operators take the form (eqns. 3.59, 3.60):

$$\hat{\psi}_H(x) = \hat{U}_C(t_0, t)\hat{\psi}(\mathbf{x})\hat{U}_C(t, t_0) \tag{4.2}$$

$$\hat{\psi}_H^\dagger(x) = \hat{U}_C(t_0, t)\hat{\psi}^\dagger(\mathbf{x})\hat{U}_C(t, t_0) \tag{4.3}$$

The contour ordering operator is defined in a slightly different manner from $\hat{T}_C$ in eqn. 3.14. For single field operators ($\hat{O}_j \in \{\hat{\psi}(\mathbf{x}), \hat{\psi}^\dagger(\mathbf{x})\}$), it has the property that every consecutive permutation of field operators on the KC changes the sign of the contour ordered product.

$$\begin{aligned} &\hat{\mathcal{T}}_C\left[\hat{O}_1(t_1)\cdots\hat{O}_n(t_n)\right] \equiv \\ &\sum_P (-1)^{N_P}\Theta_C(t_{P(1)}, t_{P(2)})\Theta_C(t_{P(2)}, t_{P(3)})\cdots\Theta_C(t_{P(n-1)}, t_{P(n)})\times \\ &\hat{O}_{P(1)}(t_{P(1)})\cdots\hat{O}_{P(n)}(t_{P(n)}). \end{aligned} \tag{4.4}$$

where all quantities are, as defined in section 3.2 and N_P is the number of consecutive permutations necessary to return the product to the form on the left side of eqn. 4.4.

Equation 4.4 can be used to expand the total GF (eqn. 4.1), allowing it to be expressed as a sum over two types of GFs related to the relative positions of the two time variables on the KC:

$$G(x, x') = \Theta_C(t, t')G^>(x, x') + \Theta_C(t', t)G^<(x, x'), \tag{4.5}$$

where the step function, $\Theta_C(t, t')$, is 1 if t is later than t' on the Keldysh contour. The lesser GF, $G^<(x, x')$ and greater GF, $G^>(x, x')$ have the following forms.

$$G^<(x, x') \equiv i\frac{Tr[\hat{U}_C(t_0 - i\beta, t_0)\hat{\psi}_H^\dagger(x')\hat{\psi}_H(x)]}{Tr[\hat{U}_C(t_0 - i\beta, t_0)]}. \tag{4.6}$$

$$G^>(x, x') \equiv -i\frac{Tr[\hat{U}_C(t_0 - i\beta, t_0)\hat{\psi}_H(x)\hat{\psi}_H^\dagger(x')]}{Tr[\hat{U}_C(t_0 - i\beta, t_0)]}. \tag{4.7}$$

The GF of greatest interest is the lesser GF, which (as is shown in section 4.2) gives the electronic number density when evaluated at on the real branch of the KC. However, both the lesser and greater GFs are used to define several other GFs that

correspond to different branches of the KC. These GFs allow for the evaluation of the lesser GF from the given Hamiltonian. We start with the definition of the Matsubara GF,

$$G^M(x_\tau, x'_{\tau'}) = \Theta(\tau - \tau')G^>(x_\tau, x'_{\tau'}) + \Theta(\tau' - \tau)G^<(x_\tau, x'_{\tau'}) \tag{4.8}$$

where $x_\tau = (\mathbf{x}, t_0 - i\tau)$ and $x'_{\tau'} = (\mathbf{x}', t_0 - i\tau')$. The active time variable $t_0 - i\tau$ and $t_0 - i\tau'$ are found on the complex branch of the Keldysh contour. Note that the imaginary axis describes the thermally equilibrated system as explained in the previous chapter. Next, we restrict $G^<$ and $G^>$ to the real branches of the Keldysh contour. Note that, since the contour ordering operator $\hat{\mathbf{T}}_C$ has been removed in defining $G^<$ and $G^>$, the contour ordered propagators $\hat{U}_C$ can, for real t and t', be replaced with real time propagators $\hat{U}$. We thus define the retarded GF, G^R and the advanced GF G^A on the real time axis as,

$$\begin{aligned} G^R(x, x') =& \Theta(t - t') \left[G^>(x, x') - G^<(x, x')\right] \\ =& -i\Theta(t - t') \frac{Tr\left[\hat{U}_C(t_0 - i\beta, t_0)\left\{\hat{\psi}_H(x), \hat{\psi}^\dagger_H(x')\right\}\right]}{Tr[\hat{U}_C(t_0 - i\beta, t_0)]} \end{aligned} \tag{4.9}$$

$$\begin{aligned} G^A(x, x') =& -\Theta(t' - t) \left[G^>(x, x') - G^<(x, x')\right] \\ =& i\Theta(t' - t) \frac{Tr\left[\hat{U}_C(t_0 - i\beta, t_0)\left\{\hat{\psi}_H(x), \hat{\psi}^\dagger_H(x')\right\}\right]}{Tr[\hat{U}_C(t_0 - i\beta, t_0)]} \end{aligned} \tag{4.10}$$

The Matsubara, retarded and advanced GFs play an instrumental role in describing the steady state physics of the system and in providing the initial conditions for a dynamic treatment of the system. Finally, we divide the lesser GF into two real time branches, where

$$G^<_1(x, x') = \Theta(t - t')G^<(x, x') \tag{4.11}$$

$$G^<_2(x, x') = \Theta(t' - t)G^<(x, x') \tag{4.12}$$

Note that $G^<(x,x') = G_1^<(x,x') + G_2^<(x,x')$. These forms are necessary for a proper energy regime description of the manifold of states as described in chapter V.

4.2 Properties

In this section, certain important properties of and relations between the various GFs described above are derived. In particular, the relation between the lesser GF and the energy resolved electron density is shown. This leads to the connection between the lesser GF and the occupied density of states. Furthermore, the relation between this GF and the expectation value of a non interacting operator is derived. Finally, various conjugate transform identities and the Kubo-Martin-Schwinger (KMS) boundary conditions are derived. These relations assist in finding a closed for for the equilibrated lesser GF in terms of the Hamiltonian.

4.2.1 Green Function of Time Independent Hamiltonian

For the case of a time independent Hamiltonian, one can show that the Green function (eqn. 4.1) and all of its branch restricted forms (eqns. 4.6-4.12) become temporally dependent only on the difference between the two time variables $\Delta t = t - t'$.

$$G(x,x') = G(\mathbf{x},\mathbf{x}';t-t') \tag{4.13}$$

To show this, one simple substitutes the explicit form for the propagator of a time independent Hamiltonian,

$$\hat{U}(t,t_0) = e^{-i(\hat{H}_0 - \mu\hat{N})(t-t_0)} \tag{4.14}$$

into the definition of the Green function (eqn. 4.1). This is shown for $G^<$. A similar derivation can be performed for $G^>$ and thus this rule is valid for the total GF, G. Likewise G^R and G^A can be shown to obey this property. The Matsubara GF, G^M

always obeys this property since the Hamiltonian is always time independent on the complex part of the KC. Using the cyclic property of the trace,

(4.15)
$$\begin{aligned} G^{<}(x,x') =& i\frac{Tr[e^{-\beta(\hat{H}_0-\mu\hat{N})}e^{-i(\hat{H}_0-\mu\hat{N})(t_0-t')}\hat{\psi}^{\dagger}(\mathbf{x}')e^{-i(\hat{H}_0-\mu\hat{N})(t'-t)}\hat{\psi}(\mathbf{x})e^{-i(\hat{H}_0-\mu\hat{N})(t-t_0)}]}{Tr[e^{-\beta(\hat{H}_0-\mu\hat{N})}]} \\ =& i\frac{Tr[e^{-\beta(\hat{H}_0-\mu\hat{N})}\hat{\psi}^{\dagger}(\mathbf{x}')e^{i(\hat{H}_0-\mu\hat{N})(\Delta t)}\hat{\psi}(\mathbf{x})e^{-i(\hat{H}_0-\mu\hat{N})(\Delta t)}]}{Tr[e^{-\beta(\hat{H}_0-\mu\hat{N})}]}. \end{aligned}$$

For G^M, the same property can be verified, namely,

$$G^M(x_\tau, x'_{\tau'}) = G(\mathbf{x},\mathbf{x}';\tau-\tau') \tag{4.16}$$

provided that, as long as the time variable is not conjugated in the complex time propagator,

$$\hat{U}(t_\tau,t_0) = e^{-i(\hat{H}_0-\mu\hat{N})(t_0-(t_0-i\tau))} = e^{(\hat{H}_0-\mu\hat{N})\tau} = \hat{U}^{\dagger}(t_\tau,t_0) \neq \hat{U}^{\dagger}(t_0,t_\tau). \tag{4.17}$$

where $t_\tau = t_0 - i\tau$.

4.2.2 Populated Density of States

For the case of a time independent Hamiltonian, one can show that the Fourier transform of the spatially integrated lesser Green function with respect to Δt, gives the populated density of states. That is,

$$\begin{aligned} \rho(\bar{\omega}) =& \\ & -i\int \mathbf{d^4x} G^{<}_m(\mathbf{x},\mathbf{x};\bar{\omega}) \\ =& \sum_{n,k}\frac{e^{-\beta(E_n-\mu N_n)}}{Z}\delta(\bar{\omega}-(\Delta E^{-}_n(k)-\mu)) \end{aligned} \tag{4.18}$$

where,

$$G^{<}_m(\mathbf{x},\mathbf{x}';\bar{\omega}) \equiv \int_{-\infty}^{\infty} d(\Delta t) e^{i\bar{\omega}\Delta t} G^{<}(\mathbf{x},\mathbf{x}';\Delta t), \tag{4.19}$$

Z is the grand canonical partition function (eqn. 3.5) and $\Delta E_n^-(k)$ is the energy required to remove an electron from an occupied orbital ψ_{ϵ_k} in the many body state $|E_n, N_n\rangle$. Furthermore, selecting one of the peaks, $\Delta E_n^-(k)$ in eqn. 4.18 without spatially integrating, gives the electronic density of the k-th orbital, $|\psi_{\epsilon_k}|^2$, in state $|E_n, N_n\rangle$.

$$\lim_{\delta\to 0^+}\int_{\Delta E_n^-(k)-\mu-\delta}^{\Delta E_n^-(k)-\mu+\delta} d\bar{\omega} G_m^<(\mathbf{x},\mathbf{x};\bar{\omega}) = \frac{e^{-\beta(E_n-\mu N_n)}}{Z}|\psi_{\epsilon_k}(\mathbf{x})|^2. \tag{4.20}$$

To show this, we start by expanding the equation of the lesser Green function for a time independent Hamiltonian,

(4.21)

$$\begin{aligned} G^<(\mathbf{x},\mathbf{x};\Delta t) =& i\frac{\sum_n \langle E_n, N_n|e^{-\beta(\hat{H}_0-\mu\hat{N})}\hat{\psi}^\dagger(\mathbf{x})e^{i(\hat{H}_0-\mu\hat{N})(\Delta t)}\hat{\psi}(\mathbf{x})e^{-i(\hat{H}_0-\mu\hat{N})(\Delta t)}|E_n, N_n\rangle}{Tr[e^{-\beta(\hat{H}_0-\mu\hat{N})}]} \\ =& \frac{i}{Z}\sum_{n,m}\langle E_n, N_n|e^{-\beta(\hat{H}_0-\mu\hat{N})}\hat{\psi}^\dagger(\mathbf{x})|E_m, N_m\rangle\langle E_m, N_m|\times \\ & e^{i(\hat{H}_0-\mu\hat{N})(\Delta t)}\hat{\psi}(\mathbf{x})e^{-i(\hat{H}_0-\mu\hat{N})(\Delta t)}|E_n, N_n\rangle \\ . =& i\frac{e^{-\beta(E_n-\mu N_n)}}{Z}\sum_{n,m} e^{-i(\Delta E_{nm}-\mu\Delta N_{nm})(\Delta t)}|\langle E_m, N_m|\hat{\psi}(\mathbf{x})|E_n, N_n\rangle|^2 \end{aligned}$$

where $E_{nm} \equiv E_n - E_m$ and $N_{nm} \equiv N_n - N_m$. Fourier transforming this result with respect to Δt gives

(4.22)

$$G^<(\mathbf{x},\mathbf{x};\bar{\omega}) = i\frac{e^{-\beta(E_n-\mu N_n)}}{Z}\sum_{n,m}\delta(\bar{\omega}-(\Delta E_{nm}-\mu\Delta N_{nm}))|\langle E_m, N_m|\hat{\psi}(\mathbf{x})|E_n, N_n\rangle|^2$$

The coefficient $\langle E_m, N_m|\hat{\psi}(\mathbf{x})|E_n, N_n\rangle$ is non-zero only when the state $|E_n, N_n\rangle$ has one less electron than the state $|E_m, N_m\rangle$, that is, $|E_m, N_m\rangle = |E_m, N_n - 1\rangle$ The field operator will *probe* for the vacant orbital in $|E_n, N_m - 1\rangle$. If, for example, the j-th orbital is occupied in $|E_n, N_n\rangle$ and unoccupied in $|E_m, N_m\rangle$ then the states are written in abstract Hilbert space as,

$$|E_n, N_n\rangle = |E_n, n_i...n_j...n_k\rangle \tag{4.23}$$

$$|E_m, N_m\rangle = |E_m, n_i ... n_{j-} n_{j+} ... n_k\rangle \tag{4.24}$$

In this case,

$$\begin{aligned}\langle E_m, N_m|\hat{\psi}(\mathbf{x})|E_n, N_n\rangle = & \\ & \sum_l \psi_{\epsilon_l}(\mathbf{x})\langle E_m, n_i ... n_{j-} n_{j+} ... n_k|\hat{a}_l|E_n, n_i ... n_j ... n_k\rangle \\ =& \psi_{\epsilon_j}(\mathbf{x})\end{aligned} \tag{4.25}$$

and,

$$G^<(\mathbf{x}, \mathbf{x}; \bar{\omega}) = i\frac{e^{-\beta(E_n - \mu N_n)}}{Z}\sum_{n,k}\delta(\bar{\omega} - (\Delta E_{nm} - \mu \Delta N_{nm}))|\psi_{\epsilon_k}(\mathbf{x})|^2 \tag{4.26}$$

Integrating this spatially gives eqn. 4.18, since $\int \mathbf{d^4x}|\psi|^2(\mathbf{x}) = 1$. Likewise, selectively integrating over the energy of a specific state without integrating spatially gives eqn. 4.20.

4.2.3 Expectation Value

The lesser GF can be used to calculate the expectation value of a non-interacting operator (eqn. 3.22). To show this, we note that the expectation value of an operator is given, in the Heisenberg picture, by eqn. 3.7. Substituting the field operator representation of a non-interacting operator (eqn. 3.34) into this equation gives,

$$\begin{aligned} O(t) &= \int \mathbf{d^4x} Tr\{\hat{\rho}_\circ \hat{U}(t_\circ, t)\hat{\psi}^\dagger(\mathbf{x})o(\mathbf{x})\hat{\psi}(\mathbf{x})\hat{U}(t, t_\circ)\} \\ &= \int \mathbf{d^4x} \lim_{\mathbf{x'}\to\mathbf{x}}\Big[o(\mathbf{x})Tr\{\hat{\rho}_\circ \hat{U}(t_\circ, t)\hat{\psi}^\dagger(\mathbf{x'})\hat{\psi}(\mathbf{x})\hat{U}(t, t_\circ)\}\Big] \\ &= \int \mathbf{d^4x} \lim_{x'\to x}\Big[o(\mathbf{x})Tr\{\hat{\rho}_\circ \hat{U}(t_\circ, t')\hat{\psi}^\dagger(\mathbf{x'})\hat{U}(t', t)\hat{\psi}(\mathbf{x})\hat{U}(t, t_\circ)\}\Big] \\ &= \int \mathbf{d^4x} \lim_{x'\to x}\Big[o(\mathbf{x})Tr\{\hat{\rho}_\circ \hat{\psi}^\dagger_H(x')\hat{\psi}_H(x)\}\Big] \\ &= -i\int \mathbf{d^4x} \lim_{x'\to x}[o(\mathbf{x})G^<(x, x')] \end{aligned} \tag{4.27}$$

where we have assumed that $\hat{\rho}_\circ$ is already normalized by the grand canonical partition function (i.e. $Tr[\hat{\rho}_\circ] = 1$). We now define a mixed representation lesser GF,

$G^<_m(\mathbf{x},\mathbf{x}';\bar{t},\bar{\omega})$, where the word *mixed* implies that one variable is temporal, $\bar{t}$, while the other is spectral $\bar{\omega}$.

$$G^<_m(\mathbf{x},\mathbf{x}';\bar{t},\bar{\omega}) \equiv \int_{-\infty}^{\infty} d(\Delta t) e^{i\bar{\omega}\Delta t} G^<(\mathbf{x}\bar{t}+\Delta t/2, \mathbf{x}'\bar{t}-\Delta t/2) \tag{4.28}$$

where $\mathbf{x}t$ is a short-hand form of $(\mathbf{x},t)$. Note that, for $G^<(x,x')$, $\bar{t} \equiv (t+t')/2$ and $\Delta t = t - t'$. For this GF, the expectation value of an operator becomes,

$$\begin{aligned} O(t) =& -i \int \mathbf{d^4x} \lim_{x'\to x} [o(\mathbf{x}) G^<(x',x)] \\ =& -i\frac{1}{2\pi} \int \mathbf{d^4x} \lim_{x'\to x} \left[o(\mathbf{x}) \int_{-\infty}^{\infty} d\bar{\omega} e^{i\bar{\omega}\Delta t} G^<_m(\mathbf{x},\mathbf{x}';\bar{t},\bar{\omega}) \right] \\ =& -i\frac{1}{2\pi} \int \mathbf{d^4x} \int_{-\infty}^{\infty} d\bar{\omega} \lim_{\mathbf{x}'\to\mathbf{x}} [o(\mathbf{x}) G^<_m(\mathbf{x},\mathbf{x}';\bar{t},\bar{\omega})] \end{aligned} \tag{4.29}$$

Equations 4.27 and 4.29 show that the expectation value of a non-interacting operator can be calculated by integrating the scalar form of the operator $o(\mathbf{x})$ with the lesser GF. We now use, as examples, the operators listed in section 3.3. Before proceeding, it is worth reviewing the notation used for different variables. In the following examples, the variable x is the covariant notation for including both space-spin and time coordinates. That is, $x = (\mathbf{x},t)$ where $\mathbf{x}$ represents the spacial, $\mathbf{r}$, and spin, α, coordinates, and t represents the time.

Number Density

The scalar form of the second quantized electron number density at $\mathbf{r}_0$ is given by $n(\mathbf{x}) = \delta(\mathbf{r}-\mathbf{r}_0)$ (eqn. 3.40),

$$\begin{aligned} n(x) =& -i \int \mathbf{d^4x} \lim_{x'\to x} [\delta(\mathbf{r}-\mathbf{r}_0) G^<(x',x)] \\ =& -i \left[G^<_{\uparrow,\uparrow}(\mathbf{r}_0 t, \mathbf{r}_0 t) + G^<_{\downarrow,\downarrow}(\mathbf{r}_0 t, \mathbf{r}_0 t) \right] \end{aligned} \tag{4.30}$$

where the arrows represent the spin state. Thus, the lesser GF evaluated at $x' = x$ gives the time dependent electron number density of the system. The systems in this

work are either closed (spin singlet) or spinless systems. In this case,

$$n(x) = -iG^{<}(\mathbf{r}_0 t, \mathbf{r}_0 t) \tag{4.31}$$

The expectation value of the number operator in the mixed representation (for the spinless case) is,

$$\begin{aligned} n(\mathbf{x}\bar{t}) =& -i\frac{1}{2\pi}\int \mathbf{d^4x}\int_{-\infty}^{\infty} d\bar{\omega}\lim_{\mathbf{x}'\to\mathbf{x}}\left[\delta(\mathbf{r}-\mathbf{r}_0)G_m^{<}(\mathbf{x},\mathbf{x}';\bar{t},\bar{\omega})\right] \\ =& -i\int_{-\infty}^{\infty} d\bar{\omega} G^{<}(\mathbf{r}_0,\mathbf{r}_0;\bar{t},\bar{\omega}) \end{aligned} \tag{4.32}$$

Note that eqn. 4.13 states that $n(\mathbf{x}\bar{t})$ will only be $\bar{t}$-dependent if the Hamiltonian contains a time dependent driving potential. If this driving potential is weak compared with the transition energies (or widths of energy bands) of the time independent Hamiltonian $\hat{H}_\circ$, then eqn. 4.18 becomes approximately correct for the time-dependent case as well and $-iG^{<}(\mathbf{r}_0,\mathbf{r}_0;\bar{t},\bar{\omega})d\bar{\omega}$ gives the dynamically ($\bar{t}$) evolving electron number density contribution of states with electron removal energies between $\bar{\omega}$ and $\bar{\omega}+d\bar{\omega}$. Thus, the mixed representation form for the lesser GF, $G^{<}(\mathbf{x},\mathbf{x}';\bar{t},\bar{\omega})$, gives the energy resolved density matrix described in chapter I in the position representation. This quantity, which forms the basis of this work has now been formally defined. What is left is to derive an equation of motion for it.

Current Density

Likewise, the scalar form for the second quantized current density operator (eqn. 3.45) is given by $\hat{\mathbf{j}}(\mathbf{x}) = i\left[\nabla_{\mathbf{r}'} - \vec{\nabla}_{\mathbf{r}}\right]$. The expectation value of the current density is given by (for a spinless system),

$$\begin{aligned} \mathbf{j}(x) =& \int \mathbf{d^4x}\lim_{x'\to x}\left[\delta\mathbf{r}-\mathbf{r}_0\left[\nabla_{\mathbf{r}'}-\vec{\nabla}_{\mathbf{r}}\right]G^{<}(x',x)\right] \\ =& \lim_{\mathbf{r}'\to\mathbf{r}}\left[\nabla_{\mathbf{r}'}-\vec{\nabla}_{\mathbf{r}}\right]G^{<}(\mathbf{r}t,\mathbf{r}'t) \end{aligned} \tag{4.33}$$

or alternatively, in the mixed representation form, by

$$\begin{aligned}\mathbf{j}(\mathbf{x}\bar{t}) =& \frac{1}{2\pi}\int \mathbf{d^4x}\int_{-\infty}^{\infty} d\bar{\omega}\lim_{\mathbf{x'}\to\mathbf{x}}\left[\left[\nabla_{\mathbf{r'}}-\vec{\nabla}_{\mathbf{r}}\right]G_m^<(\mathbf{x},\mathbf{x'};\bar{t},\bar{\omega})\right] \\ =& \lim_{\mathbf{r'}\to\mathbf{r}}\left[\nabla_{\mathbf{r'}}-\vec{\nabla}_{\mathbf{r}}\right]G_m^<(\mathbf{r},\mathbf{r'};\bar{t},\bar{\omega})\end{aligned} \tag{4.34}$$

One may define an energy resolved current density $\mathbf{J}(\mathbf{r},\bar{t},\bar{\omega})$ analogous to the energy resolved number density, $-iG^<(\mathbf{r},\mathbf{r};\bar{t},\bar{\omega})$, where $\mathbf{J}(\mathbf{r},\bar{t},\bar{\omega})d\bar{\omega}$ gives the contribution to the total current density of the states with electron removal energy between $\bar{\omega}$ and $\bar{\omega}+d\bar{\omega}$. A similar procedure can be followed for other operators of interest, such as the dipole operator and the non-interacting Hamiltonian.

The Wealth of Information contained in $G^<$

Note that , if the electronic orbitals, ψ_{ϵ_j} are purely real, than the number density, dipole and Hamiltonian operators will be purely real, while the current density operator is pure imaginary (see eqn. 4.29). Real operators will select the imaginary part of $G^<$ (real part of the density) since tracing with the real part must give zero, or the expectation value will be complex. On the other hand, an imaginary operator, such as the current density operator, selects the real part of $G^<$. Thus, the lesser Green function contains a wealth of information. Density related information, such as electron number density and dipole moment is carried by the imaginary part of $G^<$ while gradient related information, such as current density (flux), is typically carried by the real part of $G^<$.

4.2.4 Boundary Conditions and Conjugate Transpose Relations

Finally, we list several important properties of the various branch defined GFs. We start with an important relation between $G^{>}(\mathbf{x}t, \mathbf{x}'t)$ and $G^{<}(\mathbf{x}t, \mathbf{x}'t)$,

(4.35)

$$\begin{aligned} G^{>}(\mathbf{x}t, \mathbf{x}'t) - G^{<}(\mathbf{x}t, \mathbf{x}'t) = & \\ & - i\frac{Tr\left[\hat{U}_C(t_0 - i\beta, t_0)\left\{\hat{\psi}_H(\mathbf{x}t), \hat{\psi}_H^{\dagger}(\mathbf{x}'t)\right\}\right]}{Tr[\hat{U}_C(t_0 - i\beta, t_0)]} \\ & - i\frac{Tr\left[\hat{U}_C(t_0 - i\beta, t_0)\left\{\hat{U}_C(t_0, t)\hat{\psi}(\mathbf{x}), \hat{\psi}^{\dagger}(\mathbf{x})\hat{U}_C(t, t_0)\right\}\right]}{Tr[\hat{U}_C(t_0 - i\beta, t_0)]} \\ = & - i\delta(\mathbf{r} - \mathbf{r}')\delta_{\alpha,\alpha'} \end{aligned}$$

where we have used the anticommutation relation for field operators given by eqn. 3.37 and the space-spin coordinates $\mathbf{x}_1$, $\mathbf{x}_2$ have been divided into their respective spatial and spin parts, $\mathbf{r}$, $\mathbf{r}'$ and α, α'. Next, we elaborate on the conjugate transform relation for $G^{<}$,

(4.36)

$$\begin{aligned} G^{<*}(x, x') = & \\ & - i\frac{Tr\left[\left[\hat{U}_C(t_0 - i\beta, t_0)\hat{\psi}_H^{\dagger}(x')\hat{\psi}_H(x)\right]^{\dagger}\right]}{Tr[\hat{U}_C^{\dagger}(t_0 - i\beta, t_0)]} \\ = & - i\frac{Tr\left[\hat{\psi}_H^{\dagger}(x)\hat{\psi}_H(x')\hat{U}_C^{\dagger}(t_0 - i\beta, t_0)\right]}{Tr[\hat{U}_C(t_0 - i\beta, t_0)]} \\ = & - i\frac{Tr\left[\hat{\psi}_H^{\dagger}(x)\hat{\psi}_H(x')\hat{U}_C(t_0 - i\beta, t_0)\right]}{Tr[\hat{U}_C(t_0 - i\beta, t_0)]} \\ = & - i\frac{Tr\left[\hat{U}_C(t_0 - i\beta, t_0)\hat{\psi}_H^{\dagger}(x)\hat{\psi}_H(x')\right]}{Tr[\hat{U}_C(t_0 - i\beta, t_0)]} \\ = & - G^{<}(x', x) \end{aligned}$$

where, in the last step, we have used the cyclic property of the trace. Furthermore, it can be shown that the $G^{<}(x, x)$ must be purely imaginary even if $G^{<}(x, x')$ has

real components. Thus, the density is purely real as expected. To demonstrate this $G^<(x,x)$ is expressed in terms of its real and imaginary components and relation 4.36 is applied,

$$\begin{aligned} G^{<*}(x,x) =& \Re[G^<(x,x)] - i\Im[G^<(x,x)] \\ =& - G^<(x,x) \\ =& - \Re[G^<(x,x)] - i\Im[G^<(x,x)]. \end{aligned} \tag{4.37}$$

Equation 4.37 gives,

$$2\Re[G^<(x,x)] = 0 \tag{4.38}$$

as stated. With a similar approach, one can derive similar properties for the other branch restricted GFs,

$$G_1^{<*}(x,x') = -G_2^<(x',x) \tag{4.39}$$

$$G^{R*}(x,x') = G^A(x',x). \tag{4.40}$$

Now we derive the conjugation property for the mixed representation lesser GF, $G_m^<$,

$$\begin{aligned} G_m^{<*}(\mathbf{x},\mathbf{x}';\bar{t},\bar{\omega}) =& \\ & - \int_{-\infty}^{\infty} d(\Delta t) e^{-i\bar{\omega}\Delta t} G^<(\mathbf{x}\bar{t} - \Delta t/2, \mathbf{x}'\bar{t} + \Delta t/2) \\ =& - \int_{-\infty}^{\infty} d(\Delta t) e^{\bar{\omega}\Delta t} G^<(\mathbf{x}\bar{t} + \Delta t/2, \mathbf{x}'\bar{t} - \Delta t/2) \\ =& - G_m^<(\mathbf{x}',\mathbf{x};\bar{t},\bar{\omega}) \end{aligned} \tag{4.41}$$

The second line is an application of relation 4.36 and the third line comes about with the substitution $\Delta t \to -\Delta t$ in the integration variable. Likewise,

$$G_{1m}^{<*}(\mathbf{x},\mathbf{x}';\bar{t},\bar{\omega}) = -G_{2m}^<(\mathbf{x}',\mathbf{x};\bar{t},\bar{\omega}) \tag{4.42}$$

$$G_m^{R*}(\mathbf{x},\mathbf{x}';\bar{t},\bar{\omega}) = G_m^{A}(\mathbf{x}',\mathbf{x};\bar{t},\bar{\omega}) \tag{4.43}$$

for the other (analogously defined) mixed represented branch restricted GFs.

Finally, we derive the Kubo-Martin-Schwinger (KMS) relations between $G^<$ and $G^>$. These temporal *boundary conditions* are instrumental in deriving a form for the Matsubara GF, G^M. We note that,

$$\begin{aligned}
G^>(\mathbf{x}t_0 - i\beta, x') = & \\
& - i\frac{Tr\left[\hat{U}_C(t_0 - i\beta, t_0)\hat{\psi}_H(\mathbf{x}t_0 - i\beta)\hat{\psi}_H^\dagger(x')\right]}{Tr[\hat{U}_C^\dagger(t_0 - i\beta, t_0)]} \\
& = - i\frac{Tr\left[e^{-\beta(\hat{H}_0-\mu\hat{N})}\left[e^{\beta(\hat{H}_0-\mu\hat{N})}\hat{\psi}(\mathbf{x})e^{-\beta(\hat{H}_0-\mu\hat{N})}\right]\hat{\psi}_H^\dagger(x')\right]}{Tr[\hat{U}_C(t_0 - i\beta, t_0)]} \\
& = - i\frac{Tr\left[\hat{\psi}(\mathbf{x})e^{-\beta(\hat{H}_0-\mu\hat{N})}\hat{\psi}_H^\dagger(x')\right]}{Tr[\hat{U}_C(t_0 - i\beta, t_0)]} \\
& = - i\frac{Tr\left[e^{-\beta(\hat{H}_0-\mu\hat{N})}\hat{\psi}_H^\dagger(x')\hat{\psi}(\mathbf{x})\right]}{Tr[\hat{U}_C(t_0 - i\beta, t_0)]} \\
& = - G^<(\mathbf{x}t_0, x')
\end{aligned} \tag{4.44}$$

Similarly, one can show that

$$G^<(x,\mathbf{x}'t_0 - i\beta) = -G^>(x,\mathbf{x}'t_0) \tag{4.45}$$

4.3 Equations of Motion

The general equations of motion are derived by taking the partial derivatives of $G^(x,x')$ with respect to t and t', and using the equations of motion for field operators (eqns. 3.63, 3.64). This gives equations of motion in terms of one-body GFs,

$$\begin{aligned}
i\frac{\partial}{\partial t}G(x,x') = & \delta_C(t,t')\delta(\vec{x}-\vec{x}') + h(x)G(x,x') \\
& - i\int \mathbf{d^4x}''J(\mathbf{x},\mathbf{x}'')\frac{Tr[\hat{\mathcal{T}}_C[\hat{\psi}_H(x)\hat{\psi}_H^\dagger(x')\hat{\psi}_H^\dagger(\mathbf{x}''t)\hat{\psi}_H(\mathbf{x}''t)]]}{Tr[\hat{U}(t_0 - i\beta, t_0)]}
\end{aligned} \tag{4.46}$$

$$
\begin{aligned}
-i\frac{\partial}{\partial t}G(x,x') =& \delta_C(t,t')\delta(\vec{x}-\vec{x}') + h(x)G(x,x') \\
&- i\int \mathbf{d^4x}'' J(\mathbf{x}',\mathbf{x}'')\frac{Tr[\hat{\mathcal{T}}_C[\hat{\psi}_H(x)\hat{\psi}^\dagger_H(x')\hat{\psi}^\dagger_H(\mathbf{x}''t')\hat{\psi}_H(\mathbf{x}''t')]]}{Tr[\hat{U}(t_0-i\beta,t_0)]}
\end{aligned} \tag{4.47}
$$

that depend on a term with two pairs of field operators. This four operator term is expressed as a variational ansatz[57, 18, 13, 14],

$$
\begin{aligned}
&-i\int \mathbf{d^4x}'' J(\mathbf{x},\mathbf{x}'')\frac{Tr[\hat{\mathcal{T}}_C[\hat{\psi}_H(x)\hat{\psi}^\dagger_H(x')\hat{\psi}^\dagger_H(\mathbf{x}''t)\hat{\psi}_H(\mathbf{x}''t)]]}{Tr[\hat{U}(t_0-i\beta,t_0)]} \\
&\quad = \int d\vec{x}'' \int_C dt'' \Sigma_J[G](x,x'')G(x'',x')
\end{aligned} \tag{4.48}
$$

$$
\begin{aligned}
&-i\int \mathbf{d^4x}'' J(\mathbf{x}',\mathbf{x}'')\frac{Tr[\hat{\mathcal{T}}_C[\hat{\psi}_H(x)\hat{\psi}^\dagger_H(x')\hat{\psi}^\dagger_H(\mathbf{x}''t')\hat{\psi}_H(\mathbf{x}''t')]]}{Tr[\hat{U}(t_0-i\beta,t_0)]} \\
&\quad = \int d\vec{x}'' \int_C dt'' G(x,x'')\Sigma_J[G](x'',x')
\end{aligned} \tag{4.49}
$$

Thus, the GFs satisfy the electronic equation of motion:

(4.50)

$$
i\frac{\partial}{\partial t}G(x,x') = \delta_C(t,t')\delta(\vec{x}-\vec{x}') + h(x)G(x,x') + \int d\vec{x}'' \int_C dt'' \Sigma_J[G](x,x'')G(x'',x'),
$$

(4.51)

$$
-i\frac{\partial}{\partial t'}G(x,x') = \delta_C(t,t')\delta(\vec{x}-\vec{x}') + h(x')G(x,x') + \int d\vec{x}'' \int_C dt'' G(x,x'')\Sigma_J[G](x'',x'),
$$

where the space-spin coordinate integral $\int d\vec{x}''$ is taken over the entire spatial (and spin) space and the time integral $\int_C dt''$ is taken on the Keldysh contour (denoted C). The delta function $\delta_C(t,t')$, like the step function $\Theta_C(t,t')$, is also defined on the Keldysh contour. The complete one body Hamiltonian $h(x) = h_0(\vec{x}) + v(x)$ contains the electron kinetic energy and electron nuclear attractions h_0, and the time dependent external potential acting on the electrons $v(x)$. Note that Σ_J is assumed to be a functional of the one body Green function. Applying variational calculus to this ansatz produces a dynamic equation of motion for Σ_J that, together with eqns. 4.50-4.51 is typically solved self-consistently[123]. The equations for Σ_J

may be propagated directly or expanded perturbatively (diagramatically) assuming that a perturbative approximation is valid for the coulomb repulsion.

A full propagation of eqns. 4.50-4.51 together with the dynamic equations of motion for Σ_J is computationally very costly. It is thus essential to taylor these equations to specific classes of problems. This work focuses on the problem of weak resonant driving fields applied to *open* systems dominated by bands of highly delocalized states. Thus, as a first approximation, Σ_J is neglected with the assumption that significant coulomb repulsion effects are included modelistically within an effective noninteracting Hamiltonian. The equations of motion then become,

$$i\frac{\partial}{\partial t}G(x,x') = \delta_C(t,t')\delta(\vec{x}-\vec{x}') + h(x)G(x,x') \tag{4.52}$$

$$-i\frac{\partial}{\partial t'}G(x,x') = \delta_C(t,t')\delta(\vec{x}-\vec{x}') + h(x')G(x,x'). \tag{4.53}$$

The remainder of this work will focus on solving for $G^<$ in this limit. The electron correlation self-energy can ultimately be introduced in a limited fashion as needed, but its effects are not covered in this work. We now take eqns. 4.52-4.53, where t and t' are on the KC and specialize them to the branches on which $G^<$, G^R, G^A and G_M are defined. We start with $G^<$. As, with $G(x,x')$, one can differentiate $G^<(x,x')$ separately with respect to t or t' and substitute the field operator equations of motion in the absence of a pairwise potential,

$$i\frac{\partial}{\partial t}\hat{\psi}_H(x) = h(x)\hat{\psi}_H(x) \tag{4.54}$$

$$i\frac{\partial}{\partial t}\hat{\psi}^\dagger_H(x) = -h(x)\hat{\psi}^\dagger_H(x) \tag{4.55}$$

to give,

$$i\frac{\partial}{\partial t}G^<(x,x') = h(x)G^<(x,x') \tag{4.56}$$

$$-i\frac{\partial}{\partial t'}G^{<}(x,x') = h(x')G^{<}(x,x'). \tag{4.57}$$

A similar approach can be taken with $G^{>}$ to give,

$$i\frac{\partial}{\partial t}G^{>}(x,x') = h(x)G^{>}(x,x') \tag{4.58}$$

$$-i\frac{\partial}{\partial t'}G^{>}(x,x') = h(x')G^{>}(x,x'). \tag{4.59}$$

Note that substituting eqn. 4.5 into eqns. 4.52-4.53 will also give eqns. 4.56-4.59. With the same approach, one can show that,

$$i\frac{\partial}{\partial t}G^{\{R,A\}}(x,x') = \delta(t-t')\delta(\vec{x}-\vec{x}') + h(x)G^{\{R,A\}}(x,x') \tag{4.60}$$

$$-i\frac{\partial}{\partial t'}G^{\{R,A\}}(x,x') = \delta(t-t')\delta(\vec{x}-\vec{x}') + h(x')G^{\{R,A\}}(x,x'). \tag{4.61}$$

where $G^{\{R,A\}}$ is either the retarded or advanced GF. Finally,

$$-\frac{\partial}{\partial \tau}G^{M}(x,x') = i\delta(\tau-\tau')\delta(\vec{x}-\vec{x}') + h(x)G^{M}(x,x') \tag{4.62}$$

$$\frac{\partial}{\partial \tau'}G^{M}(x,x') = i\delta(\tau-\tau')\delta(\vec{x}-\vec{x}') + h(x')G^{M}(x,x'). \tag{4.63}$$

Equations 4.56-4.63 are known as the Kadanoff-Baym (K-B) equations[57, 70] and correspond to the application of eqns. 4.52,4.53 to different branches of the KC.

4.4 Non-orthogonal basis set

Localized non-orthogonal basis functions, such as atomic orbital basis functions, are used to convert the equations in sections 4.1-4.3 from a spatial grid representation to a matrix representation that increases the computational efficiency. For certain non-orthogonal basis sets, such as those composed of gaussian basis functions, the spatial part of the problem can be calculated analytically, leaving only the

temporal portion to non-analytical computation. If, for a molecular junction, there is a monotonic relationship between the arrangement of the basis functions and the spatial coordinate that starts at the beginning of one electrode, traverses through the junction and ends at the end of the second electrode then such a basis set can be used to define the projection of the electrodes' manifold of states onto the junction region. The total GF can be defined as,

$$G(x,x') = \sum_{i,j} G_{i,j}(t,t')\phi_i(\mathbf{x})\phi_j^*(\mathbf{x}'). \tag{4.64}$$

where $\phi_i(\mathbf{x})$ is an element of the non-orthogonal basis set. In a similar fashion, the branch restricted GFs can be expressed,

$$G^{\{<,>,R,A\}}(x,x') = \sum_{i,j} G_{i,j}^{\{<,>,R,A\}}(t,t')\phi_i(\mathbf{x})\phi_j^*(\mathbf{x}'). \tag{4.65}$$

$$G_{1,2}^{<}(x,x') = \sum_{i,j} G_{1,2;i,j}^{<}(t,t')\phi_i(\mathbf{x})\phi_j^*(\mathbf{x}'). \tag{4.66}$$

and,

$$G^{M}(\mathbf{x}\tau,\mathbf{x}'\tau') = \sum_{i,j} G_{i,j}^{M}(\tau,\tau')\phi_i(\mathbf{x})\phi_j^*(\mathbf{x}'). \tag{4.67}$$

Likewise, in the mixed representation,

$$G_{m}^{\{<,>,R,A\}}(\mathbf{x},\mathbf{x}',\bar{t},\bar{\omega}) = \sum_{i,j} G_{m;i,j}^{\{<,>,R,A\}}(\bar{t},\bar{\omega})\phi_i(\mathbf{x})\phi_j^*(\mathbf{x}'). \tag{4.68}$$

4.4.1 Expectation Values in the Non-orthogonal Basis

The expectation value of a non-interacting operator can be written in terms of the lesser GF (eqn. 4.27). Applying the basis set form for the lesser GF gives,

$$\begin{aligned} O(t) &= -i \int \mathbf{d^4x} \lim_{x' \to x} [o(\mathbf{x}) G^<(x, x')] \\ &= -i \int \mathbf{d^4x} \lim_{x' \to x} \left[o(\mathbf{x}) \sum_{i,j} G_{i,j}^{\{<,>,R,A\}}(t, t') \phi_i(\mathbf{x}) \phi_j^*(\mathbf{x}') \right] \\ &= -i \sum_{i,j} \left[\int \mathbf{d^4x} \phi_j^*(\mathbf{x}) o(\mathbf{x}) \phi_i(\mathbf{x}) \right] G_{i,j}^<(t, t) \\ &= -iTr\left[\mathbf{o}\mathbf{G}^<(t, t)\right] \end{aligned} \tag{4.69}$$

where,

$$\mathbf{o}_{ij} \equiv \int \mathbf{d^4x} \phi_j^*(\mathbf{x}) o(\mathbf{x}) \phi_i(\mathbf{x}) \tag{4.70}$$

Likewise, for the mixed representation lesser GF,

$$O(t) = -i \int d\bar{\omega} Tr\left[\mathbf{o}\mathbf{G}_m^<(\bar{t}, \bar{\omega})\right] \tag{4.71}$$

We now give some examples.

Electron Number

One can show that the total number of electrons in a system is given by,

$$N(t) = -i \int d\bar{\omega} Tr\left[\mathbf{S}\mathbf{G}_m^<(\bar{t}, \bar{\omega})\right] \tag{4.72}$$

where $\mathbf{S}$ is the overlap matrix,

$$\mathbf{S}_{ij} \equiv \int \mathbf{d^4x} \phi_j^*(\mathbf{x}) \phi_i(\mathbf{x}). \tag{4.73}$$

Note that for an orthonormal basis, $\mathbf{S} = \mathbf{1}$.

Electron Current Density

Note that the current density operator becomes a spatially dependent matrix due to the delta function in eqn. 3.47.

$$\mathbf{j}(\mathbf{r}t) = -i \int d\bar{\omega} Tr \left[\mathbf{j}(\mathbf{r}) \mathbf{G}_m^<(\bar{t}, \bar{\omega})\right] \tag{4.74}$$

where $\mathbf{j}(\mathbf{r})$ is a three spatial-component matrix ($\mathbf{j}(\mathbf{r}) = \hat{\mathbf{i}}\mathbf{j}_x(\mathbf{r}) + \hat{\mathbf{j}}\mathbf{j}_y(\mathbf{r}) + \hat{\mathbf{k}}\mathbf{j}_z(\mathbf{r})$) that, when traced with $\mathbf{G}^<$ gives the spatially resolved *vector* current density. This current density operator, in basis form, becomes

$$\mathbf{j}_{ij}(\mathbf{r}) = i\delta_{\alpha\alpha'} \left[\phi_i(\mathbf{r}) \nabla_{\mathbf{r}} \phi_j^*(\mathbf{r}) - \phi_j^*(\mathbf{r}) \nabla_{\mathbf{r}} \phi_i(\mathbf{r})\right]. \tag{4.75}$$

where α and α' represent the spin components of the basis functions.

Dipole Operator

In a similar fashion, the expectation value of the dipole moment is given by,

$$d(t) = -i \int d\bar{\omega} Tr \left[\mathbf{d} \mathbf{G}_m^<(\bar{t}, \bar{\omega})\right] \tag{4.76}$$

where $\mathbf{d}$ is the transition dipole matrix,

$$\mathbf{d}_{ij} \equiv \int \mathbf{d^4x} \phi_j^*(\mathbf{x}) \mathbf{r} \phi_i(\mathbf{x}). \tag{4.77}$$

Note that $d(t)$ can be Fourier transformed to give the excitation spectrum,

$$d(\Delta\omega) = \int dt e^{i\Delta\omega t} d(t). \tag{4.78}$$

4.4.2 Boundary Conditions and Conjugation Relations in the Non-orthogonal Basis

We now show the basis-set representation of relations in section 4.2.4. We start with eqn. 4.35 and, for simplicity, assume a spinless system,

$$\begin{aligned} G^{>}(\mathbf{x}t,\mathbf{x}'t) - G^{<}(\mathbf{x}t,\mathbf{x}'t) = & \\ & \sum_{i,j}\left[G^{>}_{ij}(t,t) - G^{<}_{ij}(t,t)\right]\phi_i(\mathbf{x})\phi^*_j(\mathbf{x}') \\ & = -i\delta(\mathbf{r}-\mathbf{r}'). \end{aligned} \tag{4.79}$$

Multiplying both sides of eqn. 4.79 by $\phi^*_k(\mathbf{x})$ and integrating with respect to volume in $\mathbf{x}$ gives,

$$\begin{aligned} & \sum_{i,j}\mathbf{S}_{ki}\left[G^{>}_{ij}(t,t) - G^{<}_{ij}(t,t)\right]\phi^*_j(\mathbf{x}') \\ & = -i\phi^*_k(\mathbf{x}') \\ & = -i\sum_j \delta_{kj}\phi^*_j(\mathbf{x}'). \end{aligned} \tag{4.80}$$

Rewriting this equation, gives,

$$\sum_j\left\{\sum_i \mathbf{S}_{ki}\left[G^{>}_{ij}(t,t) - G^{<}_{ij}(t,t)\right] + i\sum_j\delta_{kj}\right\}\phi^*_j(\mathbf{x}') = 0. \tag{4.81}$$

In order to satisfy eqn. 4.81 independent of the spatial form of the basis functions $\phi_i(\mathbf{x})$, each factor that multiplies $\phi^*_j(\mathbf{x}')$ in this equation must be set equal to zero. Thus, the basis set dependent form of eqn. 4.35 becomes,

$$\mathbf{G}^{>}(t,t) - \mathbf{G}^{<}(t,t) = -i\mathbf{S}^{-1} \tag{4.82}$$

Next, we express the conjugate transform relation for the lesser GF (eqn. 4.36) in

the basis set representation,

$$
\begin{aligned}
G^{<*}(x,x') = & \\
& \sum_{i,j} G^{<*}_{i,j}(t,t')\phi^*_i(\mathbf{x})\phi_j(\mathbf{x}') \\
&= \sum_{j,i} G^{<*}_{j,i}(t,t')\phi^*_j(\mathbf{x})\phi_i(\mathbf{x}') \qquad (4.83)\\
&= - G^{<}(x',x) \\
&= - \sum_{i,j} G^{<}_{i,j}(t',t)\phi_i(\mathbf{x}')\phi^*_j(\mathbf{x}).
\end{aligned}
$$

Thus,

$$\sum_{j,i} \left[G^{<*}_{j,i}(t,t') + G^{<}_{i,j}(t',t)\right] \phi^*_j(\mathbf{x})\phi_i(\mathbf{x}') = 0. \qquad (4.84)$$

As before, the factor multiplying the basis functions must be identically zero, and thus,

$$\mathbf{G}^{<\dagger}(t,t') = -\mathbf{G}^{<}(t',t) \qquad (4.85)$$

Similarly,

$$\mathbf{G}_1^{<\dagger}(t,t') = -\mathbf{G}_2^{<}(t',t) \qquad (4.86)$$

$$\mathbf{G}^{R\dagger}(t,t') = -\mathbf{G}^{A}(t',t) \qquad (4.87)$$

$$\mathbf{G}_m^{<\dagger}(\bar{t},\bar{\omega}) = -\mathbf{G}_m^{<}(\bar{t},\bar{\omega}) \qquad (4.88)$$

and finally, the boundary conditions for $\mathbf{G}^{<}$ and $\mathbf{G}^{>}$ involving the complex branch of the KC,

$$\mathbf{G}^{>}(t_0 - i\beta, t') = -\mathbf{G}^{<}(t_0,t') \qquad (4.89)$$

$$\mathbf{G}^{<}(t, t_0 - i\beta) = -\mathbf{G}^{>}(t,t_0) \qquad (4.90)$$

4.4.3 Equations of Motion in the Non-orthogonal Basis

With the same approach used to derive eqn. 4.82, one can show that, in the basis set representation, the equations of motion are,

$$\left[i\mathbf{S}\frac{\partial}{\partial t} - \mathbf{h}(t)\right]\mathbf{G}^{<}(t,t') = 0 \tag{4.91}$$

$$-i\frac{\partial}{\partial t'}\mathbf{G}^{<}(t,t')\mathbf{S} - \mathbf{G}^{<}(t,t')\mathbf{h}(t') = 0 \tag{4.92}$$

$$\left[i\mathbf{S}\frac{\partial}{\partial t} - \mathbf{h}(t)\right]\mathbf{G}^{\{R,A\}}(t,t') = \delta(t-t')\mathbf{1} \tag{4.93}$$

$$-i\frac{\partial}{\partial t'}\mathbf{G}^{\{R,A\}}(t,t')\mathbf{S} - \mathbf{G}^{\{R,A\}}(t,t')\mathbf{h}(t') = \delta(t-t')\mathbf{1} \tag{4.94}$$

$$\left[-\mathbf{S}\frac{\partial}{\partial t} - \mathbf{h}(t)\right]\mathbf{G}^{M}(t,t') = i\delta(t-t')\mathbf{1} \tag{4.95}$$

$$\frac{\partial}{\partial t'}\mathbf{G}^{\{R,A\}}(t,t')\mathbf{S} - \mathbf{G}^{M}(t,t')\mathbf{h}(t') = i\delta(t-t')\mathbf{1} \tag{4.96}$$

where $h_{i,j}(t) = \int \mathbf{d^4x}\phi_i^*(\vec{x})h(x)\phi_j(\vec{x})$. Note that we have only listed the branch restricted equations of motion.

4.4.4 Orthogonalization

An orthogonalized basis set, where $\mathbf{S} = \mathbf{1}$ can be defined and is related to the non-orthogonal (atomic orbital) basis set as follows. For GFs,

$$\mathbf{G}_{\perp} = \mathbf{S}^{1/2}\mathbf{G}\mathbf{S}^{1/2} \tag{4.97}$$

while for operators (such as $\mathbf{h}(t)$ or $\mathbf{j}$) are transformed to,

$$\mathbf{o}_{\perp} = \mathbf{S}^{-1/2}\mathbf{o}\mathbf{S}^{-1/2} \tag{4.98}$$

where the symbol "$\perp$" represents the operator in the orthogonal representation. This, for example transforms the above equations of motion for the lesser GF into,

$$\left[i\mathbf{1}\frac{\partial}{\partial t} - \mathbf{h}_{\perp}(t)\right]\mathbf{G}^{<}_{\perp}(t,t') = 0 \tag{4.99}$$

$$-i\frac{\partial}{\partial t'}\mathbf{G}^{<}_{\perp}(t,t') - \mathbf{G}^{<}_{\perp}(t,t')\mathbf{h}_{\perp}(t') = 0 \tag{4.100}$$

The equations of motion for the other branch restricted GFs can be transformed in a similar fashion. Note that $\mathbf{h}$ is not diagonalized. It has simply been rotated into a basis that produces an orthogonal overlap. This basis projects the overlap couplings onto the Hamiltonian. For a typical atomic orbital basis (one composed of slater type orbitals), this orthogonalization procedure will delocalize the atomic orbitals, extending them typically over nearest to third nearest neighbors. The orthogonalized basis, however, will still typically follow the coordinate that traverses from the left electrode through the junction to the right electrode making it feasible within the atomic orbital projection schemes describe in the next chapter.

4.4.5 A Specific Example: One Electron Gaussian Basis Set

Gaussian basis functions are frequently employed in quantum chemistry packages because matrix elements of most pertinent operators can be solved analytically with a gaussian basis. Those that cannot be solved completely analytically, such as coulomb interaction terms, can often be reduced to expressions of the error function, and thus, numerically evaluated by most programming languages. These basis functions are real valued and therefore, I will neglect the complex conjugation notation when referring to them. For a detailed explanation of basis sets see the section on polyatomic basis sets in [117]. Here we will provide a synopsis of how the operators relevant to this work are calculated using simple s-type gaussian basis functions of

the form,

$$\phi_\alpha(\mathbf{r}, \mathbf{R}_A) = \left(\frac{2\alpha}{\pi}\right)^{3/4} e^{-\alpha|\mathbf{r}-\mathbf{R}_A|^2} \tag{4.101}$$

where $\mathbf{r}$ is the spatial coordinate of electronic charge density and $\mathbf{R}_A$ is the nuclear position coordinate of atom A. Both $\mathbf{r}$ and $\mathbf{R}_A$ are taken relative to one absolute origin (e.g. the center of mass of the molecule in the body frame of reference). We assume, for simplicity, that each atom has one electron and therefore one orbital is associated with each nucleus. Furthermore, the system is assumed to be spinless, and therefore, reduces from four dimensions (3-spatial and 1-spin, denoted by $\mathbf{x}$ in previous sections) to three dimensions (all spatial, denoted by $\mathbf{r}$)). The operators of my focus are the overlap operator (eqn. 4.73), the dipole operator (eqn. 4.77), the current density operator (eqn. 4.75), and the current operator. The Hamiltonians considered in this work are expressed as either model tight-binding matrices, or semi-empirical functions of the overlap operator. Thus kinetic energy and coulomb interaction operators are not considered here. For a detailed derivation of these operators, see appendix A of reference [117].

The overlap matrix element between electron on atom A and electron on atom B (eqn. 4.73) is given by[117],

(4.102)

$$S_{AB} = \int \mathbf{d^3r}\phi_\alpha(\mathbf{r}_A, \mathbf{R}_A)\phi_\beta(\mathbf{r}_B, \mathbf{R}_B) = (\alpha\beta)^{3/4}(\frac{2}{\alpha+\beta})^{3/2} \exp\left[\frac{\alpha\beta}{\alpha+\beta}|\mathbf{R}_A - \mathbf{R}_B|^2\right].$$

Note that, the on-site overlap element S_{AA} ($\mathbf{R}_A = \mathbf{R}_B$) is unity.

Next, we focus on the dipole operator (eqn. 4.77). Due to the vector nature of this operator, we factor the basis function into its cartesian one-dimensional component functions.

$$\phi_\alpha(\mathbf{r}_A, \mathbf{R}_A) = \mathcal{X}_\alpha(x_A, X_A)\mathcal{Y}_\alpha(y_A, Y_A)\mathcal{Z}_\alpha(z_A, Z_A) \tag{4.103}$$

where, for example,

$$\mathcal{X}_\alpha(x_A, X_A) = \left(\frac{2\alpha}{\pi}\right)^{1/4} e^{-\alpha(x_A - X_A)^2}. \tag{4.104}$$

Using the above form, the matrix elements of the dipole operator are expressed as follows,

(4.105)

$$\begin{aligned}
\mathbf{d}_{AB} = & \\
& \mathbf{e}_x d_{AB_x} + \mathbf{e}_y d_{AB_y} + \mathbf{e}_z d_{AB_z} \\
=& \mathbf{e}_x \int dx \mathcal{X}_\alpha(x_A, X_A) x \mathcal{X}_\beta(x_B, X_B) \int dy \mathcal{Y}_\alpha(y_A, Y_A) \mathcal{Y}_\beta(y_B, Y_B) \int dz \mathcal{Z}_\alpha(z_A, Z_A) \mathcal{Z}_\beta(z_B, Z_B) \\
& + \mathbf{e}_y \int dx \mathcal{X}_\alpha(x_A, X_A) \mathcal{X}_\beta(x_B, X_B) \int dy \mathcal{Y}_\alpha(y_A, Y_A) y \mathcal{Y}_\beta(y_B, Y_B) \int dz \mathcal{Z}_\alpha(z_A, Z_A) \mathcal{Z}_\beta(z_B, Z_B) \\
& + \mathbf{e}_z \int dx \mathcal{X}_\alpha(x_A, X_A) \mathcal{X}_\beta(x_B, X_B) \int dy \mathcal{Y}_\alpha(y_A, Y_A) \mathcal{Y}_\beta(y_B, Y_B) \int dz \mathcal{Z}_\alpha(z_A, Z_A) z \mathcal{Z}_\beta(z_B, Z_B)
\end{aligned}$$

where $\mathbf{e}_x, \mathbf{e}_y, \mathbf{e}_z$ represent the unit vector components in each of the cartesian directions x, y and z. We now focus on the evaluation of the dipole matrix element's x component, given that the y and z components are analogous in their evaluation. In particular, we focus on the dipole integral over the x coordinate.

(4.106)

$$\begin{aligned}
\int dx \mathcal{X}_\alpha(x_A, X_A) x \mathcal{X}_\beta(x_B, X_B) = & \\
& \left(\frac{2}{\pi}\right)^{1/2} (\alpha\beta)^{1/4} \int dx x e^{-\alpha(x_A - X_A)^2} e^{-\beta(x_B - X_B)^2} \\
=& \left(\frac{2}{\pi}\right)^{1/2} (\alpha\beta)^{1/4} \exp\left[-\frac{\alpha\beta}{\alpha+\beta}(X_A - X_B)^2\right] \int dx x e^{-p(x - X_P)^2} \\
=& \left(\frac{2}{\pi}\right)^{1/2} (\alpha\beta)^{1/4} \exp\left[-\frac{\alpha\beta}{\alpha+\beta}(X_A - X_B)^2\right] \times \\
& \left[\int dx (x - X_P) e^{-p(x - X_P)^2} + X_P \int dx e^{-p(x - X_P)^2}\right] \\
=& \left(\frac{2}{\pi}\right)^{1/2} (\alpha\beta)^{1/4} \exp\left[-\frac{\alpha\beta}{\alpha+\beta}(X_A - X_B)^2\right] X_P \int dx e^{-p(x - X_P)^2} \\
=& X_P \int dx \int dx \mathcal{X}_\alpha(x_A, X_A) \mathcal{X}_\beta(x_B, X_B)
\end{aligned}$$

where $p = \alpha + \beta$ and $X_P = (\alpha X_A + \beta X_B)/(\alpha + \beta)$. Substituting the result from eqn. 4.106 into eqn. 4.105 and repeating this procedure for the y and z components gives the final result,

$$\mathbf{d}_{AB} = \frac{\alpha \mathbf{R}_A + \beta \mathbf{R}_B}{\alpha + \beta} S_{AB}. \tag{4.107}$$

Thus, the dipole matrix element between two gaussian s-type orbitals is simply the gaussian reciprocal square width weighted average of position scaled by the overlap matrix element between the two centers A and B . Note that, the on-site dipole matrix element is simply equal to the position of the respective nucleus ($\mathbf{d}_{AA} = \mathbf{R}_A$) as expected.

Finally, we consider the current density operator representation in this simple basis set. Like the dipole operator, the current density operator is a vector operator (eqn. 4.75). Substituting equation 4.101 into eqn. 4.75 gives,

$$\mathbf{j}_{AB}(\mathbf{r}) = 2i \left[(\alpha - \beta)\mathbf{r} + \beta \mathbf{R}_B - \alpha \mathbf{R}_A \right] \phi_\alpha(\mathbf{r}, \mathbf{R}_A) \phi_\beta(\mathbf{r}, \mathbf{R}_B). \tag{4.108}$$

One can use this operator to calculate the total current operator through a given plane. For example, the current through the xy-plane that intersects the z-axis at $z = z_0$ will involve integrating the above expression, (evaluated at z_0) over the area of the xy plane. In this case, only the z-component is necessary because the differential area vector on the xy-plane is oriented in the z direction (i.e. $d\mathbf{A} = \mathbf{e}_z dxdy$). Performing this planar integral gives,

$$\begin{aligned} I_{AB_z} =& \int dxdy \times j_z(x, y, z_0) \\ =& i \frac{2^{5/2} (\alpha\beta)^{3/4}}{\pi^{1/2}(\alpha + \beta)} \exp\left[\frac{\alpha\beta}{\alpha + \beta} \left[(X_A - X_B)^2 + (Y_A - Y_B)^2 \right] \right] \times \\ & \exp\left[- \left[\alpha(z_0 - Z_A)^2 + \beta(z_0 - Z_B)^2 \right] \right] \left[(\alpha - \beta) z_0 + \beta Z_B - \alpha Z_A \right]. \end{aligned} \tag{4.109}$$

Note that, as the distance between either nucleus (A or B) and the plane increases, the matrix element drops off sharply (as a gaussian) in magnitude. Thus, one can confine the current operator to a finite device region in most molecular systems.

Dipole and current operators for a simple two state system

To gain physical insight, we will often deal with non-molecular systems that are described by tight binding models where a Hamiltonian is composed merely of "on-site" energies and nearest neighbor "hopping" energies. A concrete basis set such as the one described above is often not defined for such systems. Only the initial Hamiltonian and overlap matrix are defined by the tight binding conditions. It is therefore useful to elaborate on some guidelines for deriving dipole and current operators from the structure of the initial Hamiltonian. For simplicity, we assume that the initial Hamiltonian describes a symmetric system. We start with the dipole matrix. Given an already diagonalized two-state initial Hamiltonian of the form,

$$\mathbf{H}_{diag} = \begin{bmatrix} \epsilon_1 & 0 \\ 0 & \epsilon_2 \end{bmatrix}. \tag{4.110}$$

the dipole operator will take the form,

$$\mu_{diag} = \begin{bmatrix} 0 & \mu \\ \mu & 0 \end{bmatrix}. \tag{4.111}$$

The diagonal elements of this operator must be zero for a system symmetric about the origin (but not necessarily zero for a non-symmetric system). This is because the individual states for such a system will also be symmetrically distributed and therefore, cannot produce a dipole moment. On the other hand, a tight-binding Hamiltonian of the form,

$$\mathbf{H}_{tb} = \begin{bmatrix} \epsilon & \beta \\ \beta & \epsilon \end{bmatrix}. \tag{4.112}$$

will produce a dipole operator of the form,

$$\mu_{tb} = \begin{bmatrix} \mu & 0 \\ 0 & -\mu \end{bmatrix}. \tag{4.113}$$

Physically, the two diagonal elements of a tight-binding Hamiltonian each describe a geometric "site" in the system (e.g. an individual atom in a diatomic molecule). Assuming that this system is symmetric and centered at the origin, the off diagonal elements must be zero and the diagonal elements represent a ramping potential. This can be seen mathematically by applying eqn. 4.107 to each element with $\alpha = \beta$ (system symmetry) and $\mathbf{R}_A = -\mathbf{R}_B$ (center at origin).

We now focus on a practical approach for deriving the current operator from the Hamiltonian. To do this, we must first understand where the derivation of the current density operator in the spatial representation (eqn. 3.45) originates. We note that, by the assumption of spatial probability continuity, the probability current through an interface can be monitored by calculating the rate of change of the probability on one side of the interface. For example, in a one dimensional system, the probability current through a point $x = x_0$ is given by,

$$\begin{aligned} I(x_0) =& \frac{\partial}{\partial t} \int_{x_0}^{\infty} dx P(x,t) \\ =& \sum_E \int_{-\infty}^{\infty} dx \psi_E^*(x) \frac{\partial}{\partial t} \left[\hat{U}(0,t;x) \Theta(x - x_0) \hat{U}(t,0;x) \right] \psi_E(x) \end{aligned} \tag{4.114}$$

where $P(x,t)$ is the normalized TD probability density as a function of the single spatial coordinate x and E is the eigenenergy of eigenstate $\psi_E^(x)$. The last term in eqn. 4.114 is written in the Heisenberg representation, where Θ is the Heaviside step function that counts population for $x > x_0$, and $\hat{U}(t',t;x)$ is the time dependent propagator from t to t' written in the spatial (x) representation. Applying the

Heisenberg equation of motion, we note that,

(4.115)

$$\frac{\partial}{\partial t}\left[\hat{U}(0,t;x)\Theta(x-x_0)\hat{U}(t,0;x)\right] = i\hat{U}(0,t)\left[\hat{H}(x,t),\Theta(x-x_0)\right]\hat{U}(t,0)$$
$$= -\frac{i}{2}\hat{U}(0,t)\left[\frac{\partial^2}{\partial x^2},\Theta(x-x_0)\right]\hat{U}(t,0)$$
$$= -\frac{i}{2}\hat{U}(0,t)\left(\frac{\partial}{\partial x}\delta(x-x_0)+\delta(x-x_0)\frac{\partial}{\partial x}\right)\hat{U}(t,0).$$

We assume that the time dependent terms in the Hamiltonian and the Coulomb interaction terms commute with $\Theta(x)$. The final step employs the commutation relation $[\hat{A}\hat{B},\hat{C}] = \hat{A}[\hat{B},\hat{C}] + [\hat{A},\hat{C}]\hat{B}$. From this form, the Schrodinger form of the operator is apparent,

(4.116)
$$j(x) = -\frac{i}{2}\left(\frac{\partial}{\partial x}\delta(x-x_0)+\delta(x-x_0)\frac{\partial}{\partial x}\right)$$

This treatment can be extended to three dimensions to give the previously stated result (eqn. 3.45).

This treatment can approximately be extended to deriving a probability current operator for a tight-binding Hamiltonian for which an explicit spatial basis is not specified. The approach is approximate because the probability current is defined as the transfer of probability from one *site* to the other. That is, the tight-binding equivalent to the above step function, $\Theta(x-x_0)$, is,

(4.117)
$$\mathbf{\Theta}_{tb} = \begin{bmatrix} 0 & 0 \\ 0 & 1 \end{bmatrix}.$$

This is different from the scenario described above, where probability is transfered from one spatial region to the other because the basis functions for a given site will often overlap slightly with other sites. Typical overlaps, however, tend to be

small and this approximation is reasonable and particularly useful for qualitative models. As noted above, the probability current operator in the Schrodinger picture is given by $i[\hat{H}_{tb}, \Theta_{tb}]$. Hence, for a tight-binding Hamiltonian, the probability current operator is,

$$\begin{aligned} \mathbf{j}_{tb} =& i \left[\begin{bmatrix} \mu & \beta \\ \beta & \mu \end{bmatrix}, \begin{bmatrix} 0 & 0 \\ 0 & 1 \end{bmatrix} \right] \\ =& i \begin{bmatrix} 0 & \beta \\ -\beta & 0 \end{bmatrix}. \end{aligned} \tag{4.118}$$

CHAPTER V

Steady State Theory

This chapter provides a detailed summary of the NEGF approach as applied to a statistically equilibrated time independent system. An explicit form for the lesser Green function in terms of the time independent Hamiltonian is derived. Furthermore, the partition free approach for calculating the device properties of an open equilibrated system (fig. 1.1) is described.[71, 38, 134, 19, 35] In this approach, electrode effects are contained in a self energy (SE) term that is added to the Hamiltonian.[37] The SE depends only on the isolated Hamiltonian of the electrode and can often be calculated analytically or by rapid iterative approaches. Calculation of SEs eliminates the need to exactly compute the states of the total system (eqn. 2.6). Finally, two commonly used approaches to compute SEs are briefly summarized, namely, the wide band approximation and the decimation approach.

5.1 Equations of Motion

In this section, the steady state formalism is derived. This formalism contains the fundamental expressions on which steady state transport is based. It also defines the system in the absence of a driving field and therefore serves as the initial point of the time propagation treatment discussed in later chapters. The proper thermalization of the full system has to be treated correctly. The initial $\mathbf{G}_0^<$ (*i.e.*

the unperturbed equilibrated system) must describe well the steady state, which is thermally equilibrated with the electron baths. We emphasize that in this physically proper non-partitioned view[30] the different subsystems are allowed to reach thermal equilibration as one system. Namely, their coupling is not part of the turned on perturbation. This has been highlighted by several recent studies.[110, 65, 112] The Keldysh formalism is used to properly account for the thermal equilibration of the device with the electrodes and its affect on $G^<$.

5.1.1 Time independent Hamiltonian: Real Branch of the Keldysh Contour

In section 4.2 it is shown that the variable $\bar{\omega}$ (the Fourier conjugate to Δt) is the independent variable for the populated density of states. In the absence of the time dependent driving fields, $G^<$, the GF that contains all information regarding the electron density, depends temporally only on Δt and therefore, only on $\bar{\omega}$. Thus, to solve the steady-state problem, we will now focus on solving for $\mathbf{G}^<(\bar{\omega})$, the basis set represented lesser GF for a time independent Hamiltonian. Since $\bar{\omega}$ is conjugate to Δt for real times, we will restrict ourselves in this subsection to solving for the equations of motion on the real branch of the Keldysh contour.

We start, however, by solving for the retarded GF for the case of a time independent Hamiltonian, $G^R(\bar{\omega})$ because this Green function is necessary for defining the evolving lesser GF in terms of the Hamiltonian of the equilibrated system. In the basis set representation, the equation of motion for the retarded GF is,

$$\left[i\mathbf{S}\frac{\partial}{\partial(\Delta t)} - \mathbf{h}_0\right]\mathbf{G}^R(\Delta t) = \delta(\Delta t)\mathbf{1} \tag{5.1}$$

Here, we have substituted the time differential relation

$$\begin{aligned}\frac{\partial}{\partial t} =& \frac{\partial(\Delta t)}{\partial t}\frac{\partial}{\partial(\Delta t)} + \frac{\partial(\bar{t})}{\partial t}\frac{\partial}{\partial(\bar{t})} \\ =& \frac{\partial}{\partial(\Delta t)} + \frac{1}{2}\frac{\partial}{\partial(\bar{t})} \\ =& \frac{\partial}{\partial(\Delta t)}\end{aligned} \tag{5.2}$$

into eqn. 4.93 noting that, for a time independent Hamiltonian, G^R is not dependent on $\bar{t}$. The step function in the definition of G^R (eqn. 4.9) makes non-zero only for positive Δt. Equation. 5.1 is therefore Fourier transformed with an infinitesimal positive imaginary displacement in $\bar{\omega}$, labeled η. That is, the Fourier transform operation performed on eqn. 5.1 is of the form,

$$\lim_{\eta \to 0^+} \int_{-\infty}^{\infty} d(\Delta t) e^{i(\bar{\omega}+i\eta)\Delta t} \tag{5.3}$$

to ensure that $\lim_{\Delta t \to \infty} G^R(\Delta t) = 0$. Applying eqn. 5.3 to eqn. 5.1 gives

$$\left[(\bar{\omega} + i\eta)\mathbf{S} - \mathbf{h}_0\right] \mathbf{G}^R(\bar{\omega}) = \tilde{\mathbf{h}}^R(\bar{\omega})\mathbf{G}^R(\bar{\omega}) = \mathbf{1} \tag{5.4}$$

or,

$$\mathbf{G}^R(\bar{\omega}) = \left[(\bar{\omega} + i\eta)\mathbf{S} - \mathbf{h}_0\right]^{-1} \tag{5.5}$$

The Electrode Self Energy

Electrode self energy expressions are widely used in formalisms implementing the Landauer approach (described later in this chapter) and its more sophisticated self-consistent field extension. In these schemes, the Hamiltonian of a cluster model is subdivided into three regions. The subspaces within the cluster model include two surface regions connected by the junction region.

If h_0 is the Hamiltonian for the entire (electrode-junction-electrode) system then $\mathbf{S}$, $\mathbf{h}_0$, $\mathbf{1}$ and $\mathbf{G}^R(\bar{\omega})$, in the atomic orbital representation, are matrices of infinite

dimension. We are interested in the small finite dimensional submatrix of $\mathbf{G}^R(\bar{\omega})$ that contains information about the junction (denoted by index C), but under the influence of the left and right electrodes (denoted by indices L and R respectively). To calculate this submatrix, eqn. 5.4 is partitioned into these L, C and R regions,

$$\begin{bmatrix} \tilde{\mathbf{h}}_{0LL} & \tilde{\mathbf{h}}_{0LC} & 0 \\ \tilde{\mathbf{h}}_{0CL} & \tilde{\mathbf{h}}_{0CC} & \tilde{\mathbf{h}}_{0CR} \\ 0 & \tilde{\mathbf{h}}_{0RC} & \tilde{\mathbf{h}}_{0RR} \end{bmatrix} \begin{bmatrix} \mathbf{G}^R_{LL}(\bar{\omega}) & \mathbf{G}^R_{LC}(\bar{\omega}) & 0 \\ \mathbf{G}^R_{CL}(\bar{\omega}) & \mathbf{G}^R_{CC}(\bar{\omega}) & \mathbf{G}^R_{CR}(\bar{\omega}) \\ 0 & \mathbf{G}^R_{RC}(\bar{\omega}) & \mathbf{G}^R_{RR}(\bar{\omega}) \end{bmatrix} = \begin{bmatrix} \mathbf{1}_{LL} & 0 & 0 \\ 0 & \mathbf{1}_{CC} & 0 \\ 0 & 0 & \mathbf{1}_{RR} \end{bmatrix} \tag{5.6}$$

Note that $\tilde{\mathbf{h}}^R_{LR}(\bar{\omega})$ and $\tilde{\mathbf{h}}^R_{RL}(\bar{\omega})$ are both assumed to be $\mathbf{0}$ In other words there is no direct interaction between the two electrodes. All interactions occur via the junction. This partitioned matrix equation of motion gives three submatrix equations,

$$\tilde{\mathbf{h}}_{0CL}\tilde{\mathbf{G}}^R_{LC}(\bar{\omega}) + \tilde{\mathbf{h}}_{0CC}\tilde{\mathbf{G}}^R_{CC}(\bar{\omega})\tilde{\mathbf{h}}_{0CR}\tilde{\mathbf{G}}^R_{RC}(\bar{\omega}) = \mathbf{1}_{CC} \tag{5.7}$$

$$\tilde{\mathbf{h}}_{0LL}\tilde{\mathbf{G}}^R_{LC}(\bar{\omega}) + \tilde{\mathbf{h}}_{0LC}\tilde{\mathbf{G}}^R_{CC}(\bar{\omega}) = 0 \tag{5.8}$$

$$\tilde{\mathbf{h}}_{0RC}\tilde{\mathbf{G}}^R_{CC}(\bar{\omega})\tilde{\mathbf{h}}_{0RR}\tilde{\mathbf{G}}^R_{RC}(\bar{\omega}) = 0 \tag{5.9}$$

Solving equations 5.8 and 5.9 for $\mathbf{G}^R_{LC}(\bar{\omega})$ and $\mathbf{G}^R_{RC}(\bar{\omega})$ respectively and substituting into eqn. 5.7 gives

$$\left[(\bar{\omega} + i\eta)\mathbf{S}_{CC} - \mathbf{h}_{0CC} - \mathbf{\Sigma}^R_L(\bar{\omega}) - \mathbf{\Sigma}^R_R(\bar{\omega})\right]\mathbf{G}^R_{CC}(\bar{\omega}) = \mathbf{1}_{CC} \tag{5.10}$$

where the left and right electrode self-energies, respectively,

$$\mathbf{\Sigma}^R_L(\bar{\omega}) \equiv \tilde{\mathbf{h}}^R_{CL}(\bar{\omega})\mathbf{g}^R_{LL}(\bar{\omega})\tilde{\mathbf{h}}^R_{LC}(\bar{\omega}) \tag{5.11}$$

$$\mathbf{\Sigma}^R_R(\bar{\omega}) \equiv \tilde{\mathbf{h}}^R_{CR}(\bar{\omega})\mathbf{g}^R_{RR}(\bar{\omega})\tilde{\mathbf{h}}^R_{RC}(\bar{\omega}) \tag{5.12}$$

include the projected effect of the electrodes on the junction region and have the same matrix dimension as the junction Hamiltonian (C). The retarded GFs for the electrodes are given by

$$\mathbf{G}^R_{LL}(\bar{\omega}) = \left[(\bar{\omega} + i\eta)\mathbf{S}_{LL} - \mathbf{h}_{0LL}\right]^{-1} \tag{5.13}$$

$$\mathbf{G}^R_{RR}(\bar{\omega}) = \left[(\bar{\omega} + i\eta)\mathbf{S}_{RR} - \mathbf{h}_{0RR}\right]^{-1} \tag{5.14}$$

for the left and right electrodes respectively. These functions are by definition of very large (e.g. infinite) dimension (L, R) because they represent the semi-infinite electrodes bonded to the junction. Consequently, eqn. 5.13-5.14 are very seldom evaluated in their explicit form. Generally, approximations, iterative approaches that capitalize on the periodicity of the electrode, or analytical forms and used. We will use two such models in future sections (i.e. the wide-band limit approximation and the tight-binding decimation technique).

To summarize, the retarded GF of the junction, $\mathbf{G}^R_{CC}(\bar{\omega})$ can be written as

$$\mathbf{G}^R_{CC}(\bar{\omega}) = \left[(\bar{\omega} + i\eta)\mathbf{S}_{CC} - \mathbf{h}_{0CC} - \mathbf{\Sigma}^R_L(\bar{\omega}) - \mathbf{\Sigma}^R_R(\bar{\omega})\right]^{-1} \tag{5.15}$$

The lesser GF

We now solve for the lesser GF, $\mathbf{G}^<(\bar{\omega})$. We start from the lesser GF in the time domain, which can be written as $\mathbf{G}^<(\Delta t) = \mathbf{G}^<_1(\Delta t) + \mathbf{G}^<_2(\Delta t)$ (see eqns. 4.11, 4.12) and apply eqn. 4.86 along with Fourier transform eqn. 5.3 to give,

$$\mathbf{G}^<(\bar{\omega}) = \mathbf{G}^<_1(\bar{\omega}) - \mathbf{G}^{<\dagger}_1(\bar{\omega}) \tag{5.16}$$

Thus, a solution to $\mathbf{G}^<_1(\bar{\omega})$ is necessary to find a solution to $\mathbf{G}^<(\bar{\omega})$.

We can solve for $\mathbf{G}^<_1(\bar{\omega})$ by developing an equation of motion for it in terms of Δt and Fourier transforming this equation as above. Differentiating $\mathbf{G}^<_1(\bar{\omega})$ with respect

to Δt and applying eqn. 4.91 for a time independent Hamiltonian gives the following equation of motion for $\mathbf{G}_1^<(\Delta t)$.

$$\left[i\mathbf{S}\frac{\partial}{\partial \Delta t} - \mathbf{h}_0\right]\mathbf{G}_1^<(\Delta t) = i\mathbf{S}\mathbf{G}^<(t_0,t_0)\delta(\Delta t) \tag{5.17}$$

We note that $\mathbf{G}_1^<(\Delta t)$, like $\mathbf{G}^R(\Delta t)$ is written in terms of a step function of Δt (eqn. 4.8), making it non-zero only for positive Δt. Thus, the same approach that was used for $\mathbf{G}^R(\Delta t)$ above, can be applied to $\mathbf{G}_1^<(\Delta t)$. Fourier transforming this equation with eqn. 5.3, gives

$$\tilde{h}\mathbf{G}_\mathbf{1}^<(\bar{\omega}) = i\mathbf{G}^<(t_0,t_0). \tag{5.18}$$

This equation of motion can be partitioned just as for the case of the retarded GF, giving,

$$\mathbf{G}_{\mathbf{1CC}}^<(\bar{\omega}) = i\mathbf{G}^{\mathbf{R}}{}_{CC}(\bar{\omega})\mathbf{G}^<{}_p(\bar{\omega}). \tag{5.19}$$

where

$$\mathbf{G}^<{}_p(\bar{\omega}) = \mathbf{G}^<{}_{CC}(t_0,t_0) - \tilde{\mathbf{h}}_{CL}^R\mathbf{g}_{LL}^R(\bar{\omega})\mathbf{G}^<{}_{LC}(t_0,t_0) - \tilde{\mathbf{h}}_{CR}^R\mathbf{g}_{RR}^R(\bar{\omega})\mathbf{G}^<{}_{RC}(t_0,t_0) \tag{5.20}$$

All that is required now is to solve for $G^<(t_0,t_0)$. To this end, we employ the Matsubara function and its equation of motion.

$\mathbf{G}^<(t_0,t_0)$ and the Matsubara GF

We now employ the use of the Matsubara GF, $\mathbf{G}^M$ in order to solve for $\mathbf{G}^<(t_0,t_0)$. The Matsubara GF (G^M), which corresponds entirely to the imaginary part of the Keldysh contour, describes exactly the system at thermal equilibrium. We restrict ourselves to the representation in which the overlap is orthogonal and, consequently, $\mathbf{h}_0$ commutes with the overlap operator. To solve for the Matsubara GF correctly, we

must satisfy four relations. The first is the definition of $\mathbf{G^M}$ (eqn. 4.8) in basis-set form,

$$\mathbf{G}^M(\Delta\tau) = \Theta(\Delta\tau)\mathbf{G}^>(\Delta\tau) + \Theta(-\Delta\tau)\mathbf{G}^<(\Delta\tau) \tag{5.21}$$

where $G^M(\mathbf{x}\tau, \mathbf{x}'\tau')$ has been replaced by the short-hand notation $G^M(\Delta\tau)$ and $\Delta\tau \equiv \tau - \tau'$ is an imaginary time (see eqn. 4.8 and thereafter). The second relation of significance, is the equation of motion for the Matsubara GF, (eqn. 4.62),

$$\left[-\mathbf{1}\frac{\partial}{\partial\Delta\tau} - \mathbf{h}_0\right] G^M(\Delta\tau) = i\delta(\Delta\tau)\mathbf{1} \tag{5.22}$$

We have converted the equation of motion for $\mathbf{G}^M$ (eqn. 4.62) to an equation in terms of $\Delta\tau$ (eqn. 5.22) by employing the same strategy used for the retarded GF in section 5.1.1. The third and fourth relations are the KMS conditions (eqns. 4.89-4.90),

$$\mathbf{G}^>(\tau' - \beta) = -\mathbf{G}^>(\tau') \tag{5.23}$$

$$\mathbf{G}^<(\beta - \tau) = -\mathbf{G}^>(-\tau). \tag{5.24}$$

We now assume an ansatz of the form,

$$\mathbf{G}^M(\Delta\tau) = \Theta(\Delta\tau)e^{\mathbf{h}_0(\Delta\tau - b)}\mathbf{B} + \Theta(-\Delta\tau)e^{\mathbf{h}_0(\Delta\tau - a)}\mathbf{A} \tag{5.25}$$

which satisfies eqn. 5.21. Imposing the KMS relations on this ansatz requires that $\mathbf{A} = -\mathbf{B}$ and $\beta + a = b$. This gives the ansatz the form,

$$\mathbf{G}^M(\Delta\tau) = \left[\Theta(-\Delta\tau)e^{\mathbf{h}_0(\Delta\tau - a)} - \Theta(\Delta\tau)e^{\mathbf{h}_0(\Delta\tau - a - \beta)}\right]\mathbf{A} \tag{5.26}$$

Substituting eqn. 5.26 into the equation of motion (eqn. 5.22) and setting $a = 0$ gives

$$\mathbf{A} = -i\left[\mathbf{1} + e^{-\beta\mathbf{h}_0}\right]^{-1} \tag{5.27}$$

giving a final form for the Matsubara GF,

$$\mathbf{G}^{M}(\Delta\tau) = i\left[\Theta(\Delta\tau)e^{\mathbf{h}_0(\Delta\tau-\beta)} - \Theta(-\Delta\tau)e^{\mathbf{h}_0(\Delta\tau}\right] \times \left[\mathbf{1} + e^{-\beta\mathbf{h}_0}\right]^{-1} \tag{5.28}$$

and thus,

$$\mathbf{G}^{<}(\Delta\tau) = ie^{\mathbf{h}_0(\Delta\tau-\beta)}\left[\mathbf{1} + e^{-\beta\mathbf{h}_0}\right]^{-1} \tag{5.29}$$

$$\mathbf{G}^{>}(\Delta\tau) = i\left[\mathbf{1} + e^{-\beta\mathbf{h}_0}\right]^{-1} \tag{5.30}$$

Consequently, at initial time t_0 (i.e. when $\Delta\tau = 0$),

$$\mathbf{G}^{<}(t_0, t_0) = ie^{-\beta\mathbf{h}_0}\left[\mathbf{1} + e^{-\beta\mathbf{h}_0}\right]^{-1} \tag{5.31}$$

$$\mathbf{G}^{>}(t_0, t_0) = i\left[\mathbf{1} + e^{-\beta\mathbf{h}_0}\right]^{-1} \tag{5.32}$$

Note that in the diagonalized representation, equation, $\mathbf{G}^{<}(0)$ ascribes, to each eigenvalue of $\mathbf{h}_0$, its Fermi-Dirac occupation number. On the other hand, $\mathbf{G}^{>}(0)$ gives the complement, or Fermi-Dirac vacancy number for a given eigenenergy. Therefore, at t_0, the lesser GF amounts to defining the occupation numbers for the states that will be evolving in time.

5.2 Self Energy Models

The treatment of the device-electrode interaction, where the effect of the electrodes on the molecular electronic states has to be well described, is a fundamental challenge in modeling molecular conductance. The coupling of a molecule to the macroscopic electrodes mixes the discrete molecular levels with the continuum of states in the electrode. New molecular states emerge from the manifold of states contributed electrode. Furthermore, conduction is an irreversible process that can

be defined only with the presence of the dissipating bath. Thus, conductivity calculations need to address the interaction between the molecule and its environment in non-equilibrium conditions.

Clearly, the use of a truncated model in describing an open system leads to difficulties arising from the varying number of electrons within the model. This has been addressed by different approaches. The simplest involves the jellium models for representing the leads[48, 69, 68, 40]. The partition free approach described above, however, naturally leads to the use of self energy (SE) models to represent the coupling of the molecule to the lead.[37] The SE matrices are projections of the bulk electronic properties of the electrode, which is characterized by its chemical potential, to a finite subspace under the influence of the device, as described above.

5.2.1 Wide Band Limit

The wide band approximation assumes that the density of states of the electrode is dominated by a wide band of states and is, therefore, independent of $\bar{\omega}$. For a non-orthogonal basis, the density of states, $\rho(\bar{\omega})$ can be related to the retarded GF by[37],

$$\rho(\bar{\omega}) = \frac{i}{\pi} Tr[\mathbf{G}^R(\bar{\omega})\mathbf{S}] \tag{5.33}$$

where $\mathbf{S}$ is the overlap matrix. Assuming $\rho(\bar{\omega}) = \rho_0$ one can easily show that a suitable (but not necessarily unique) form for the retarded GF is,

$$\mathbf{g_L^R} = -i\frac{1}{\pi\rho_0}\mathbf{S_{LL}^{-1}}, \tag{5.34}$$

where an equivalent $\mathbf{g_{rr}^R}$ for the right electrode is also used. This model can be enhanced to represent a finite band width by setting the surface GF to zero at energy regions beyond the modeled band structure.

The wide band limit approach may be implemented, for example, for gold electrodes, where the DOS is dominated by the S band.[119]

5.2.2 Decimation Approach

Unlike the wide band approximation above, the decimation approach makes no trivial assumptions about the electrode density of states. The semi-infinite electrode is assumed to be periodic. A subspace of an extended molecular model is used to provide a surface and bulk unit cell and their interactions with their nearest neighbor cell.

This assumption of periodicity has been used to express an iterative set of equations for deriving the portion of the retarded GF of the electrode projected onto the electrode's surface layer:[77, 84]

$$\gamma_{i+1}(E) = \gamma_i(E) g_{b,i}(E) \gamma_i(E) \tag{5.35}$$

$$\beta_{i+1}(E) = \beta_i(E) g_{b,i}(E) \beta_i(E) \tag{5.36}$$

$$g_{s,i+1}(E) = [g_{s,i}^{-1}(E) - \gamma_i(E) g_{b,i}(E) \beta_i(E)]^{-1} \tag{5.37}$$

$$g_{b,i+1}(E) = [g_{b,i}^{-1}(E) - \gamma_i(E) g_{b,i}(E) \beta_i(E) - \beta_i(E) g_{b,i}(E) \gamma_i(E)]^{-1}, \tag{5.38}$$

where g_s is the surface GF, G_b is the bulk GF and the process is initiated by the electronic integrals matrices calculated at the appropriate DFT level with:

$$g_{b,0} \equiv g_{s,0} = \alpha^{-1}; \quad \gamma_{i,0} = \beta^{\dagger}; \quad \beta_{i,0} = \beta \tag{5.39}$$

This calculation is repeated at every value of $\bar{\omega}$ leading to a SE that is non-trivially energy dependent.

When applying this decimation approach to the calculation of SEs, one should be aware that these SEs are defined by providing limits on the device region and the bulk repeating unit. In principle, this partitioning should not affect calculated

properties, such as conductivity, when the models used in the calculation are well converged. However, if, for example, only a margin of the surface, which is greatly altered by the adsorption, is included in the calculation, the model is bound to fail in describing faithfully transport properties. It is thus important electrode regions that carry significant populations of the localized device states in the device region.

CHAPTER VI

Time Dependent Theory

A related problem of high interest is the study of conductance under the influence of a TD perturbation such as an alternating-current (AC) field or a laser field. A large body of research has revealed a host of fascinating quantum effects associated with photoassisted conductance in mesoscopic systems such as absolute negative conductance, Coulomb blockade and Kondo effects driven by AC fields.[62, 58, 94, 76, 89, 98, 128] Even more fundamental is the inability of most treatments to describe deviation from DC conductance under steady conditions of molecular or nanoscale electronic channels.[55, 3, 11] More recently, AC response to a potential pulse ("ringing" mode) has been associated with the presence of bound states.[39, 109] These states are localized to the device. Consequently they do not facilitate resonant tunneling through broadening in contrast to conducting molecular states entangled with the electrodes.

This underlies most of the motivation for implementing TD treatments as an alternative to the widely-used NEGF scheme for describing electron transport. Some of these treatments use TD-DFT formalism. [9, 11, 10, 110, 87, 24, 23, 65, 104, 29, 101] These TD treatments have the potential to describe time-dependent effects related to the applied potential bias and the transient conductance evolving towards a steady

state. However, the coupling of the propagated electronic density to electron reservoirs results with difficulties for achieving reliable modeling. The time propagation of open systems as referred to above is especially challenging due to the need to properly treat dissipation effects. These effects mainly originate from the non-equilibrium nature of the extended systems. The Kadanoff-Baym (K-B) equations of motion (e.o.ms) as defined by the Keldysh contour[57, 18, 70, 13, 14] inherently account for all quantum-mechanical states of an *open* system including all ionization states. Namely, all possible occupation numbers are used in averaging through the use of the Grand-canonical probability expression. The particle exchange with the baths leads to system equilibration that broadens the device region based energy states.

A formal expression describing TD conductance based on Keldysh NEGF formalism was developed over a decade ago[55]. In Keldysh formalism, the complexity of the full TD description requires using temporally non-local electron-electron interaction self-energy[13, 14] (SE) terms. For steady state descriptions, on the other hand, more tractable one-variable expressions can be used. A full Keldysh NEGF-based approach employing a mixed time-frequency representation by integrating a TD Dyson equation has been reported.[79] Treatments that use DFT to describe the electron-electron SEs through a high level mean field expression in Keldysh formalism have also been achieved.[110, 65, 111] These treatments provide useful insight to the time-dependence of the modeled conducting channel responding to different forms of a TD bias pulse.

Most descriptions of dynamic transport, that are based on many body GFs-based formalisms, follow the seminal work of Jauho et al., where a partitioning scheme is utilized for describing the unperturbed system[55]. In this picture the coupling of the two bulks through the device region is turned on only as part of the perturbation

to which the dynamical response is studied. In this case, the unperturbed system's components are kept each in thermal isolation. A more meaningful description includes equilibration of the device-based conducting channels with the electron baths infinitely prior to switching on the perturbation. This physically more appropriate non-partitioned approach was suggested first by Cini for a simple model system [30] and was recently used in several real time based propagations.[110, 65, 112] The equilibration in the initial electronic density accounts for dipoles induced across the different regions. These initial state effects might be dissipated in the steady-state description (if convergence is achieved). They are, however, crucial for addressing transient effects upon the application of the potential bias perturbation.

The propagated electronic device states undergo broadening to form energy bands due to their coupling to an extended system. Our approach is based on solving the K-B electronic equations of motions (e.o.ms) as defined by the Keldysh contour with SEs expressed in the frequency domain. This is performed within the non-partitioned scheme, where we time-propagate an open system with bulk-induced broaden electronic states. In this scheme, the response of the device discrete states to the band structure is directly accounted for by the propagated electronic density.

It is important to emphasize several key ingredients and features of our approach. Our frequency space based scheme provides a desirable and efficient alternative to procedures which are based on real time propagation schemes [110, 65, 112] as difficulties in defining efficient time propagation or stepping techniques are avoided. These difficulties are especially important when dealing with dissipation effects due to open systems. This is achieved here by using SE expressions in the frequency domain and utilizing highly efficient perturbation approaches. In general, the SE models defined in the frequency domain (FD) are also more compact in represent-

ing energy-coherence driving time-dependent perturbations, whereas the real time representations of the SEs result with more complex expressions. Pure real-TD expansions require using (sufficiently) larger models of the bulk for reliably describing electron flow.

6.1 The mixed representation

In this section, we derive a master equation projecting the full system to the device region in the mixed time-frequency representation. An analytical expression is subsequently implemented and used to study TD aspects of the electron transport, where a wide-band type of an approximation is used for the bulk. In our approach, we directly calculate the time dependence of frequency resolved current, namely, the energy resolved, or Wigner form of the current distribution. This provides the most fundamental physical insight of the device response to the applied potential.

The brute force solution of an expansion involving two-time-domain variables is computationally intensive (eqns. 4.91, 4.92). Most steady state descriptions, on the other hand, utilize the ability to simplify the expression by collapsing the two time-variables to a single time difference variable. Pure time-domain representations require using sufficiently large clusters to reliably treat conductance through a device region. In the frequency domain on the other hand self-energy expressions can use a cluster model to effectively represent an open system. Here we note that the convergence of bulk-coupling self energy models with their size has been analyzed by us.[100] Frequency domain bulk-SE models are employed in our TD approach.

6.1.1 Equation of Motion

We now focus on the e.o.m. for the transformed GF: $\mathbf{G}^{<}(\bar{t},\bar{\omega})$. This mixed time-frequency representation, as used below, provides substantial physical insight into the

electronic response aspects of the propagated model system. We combine equations 4.99 and 4.100 by rewriting in terms of the time variables: $\bar{t} \equiv \frac{t_1+t_2}{2}$ and $\Delta t \equiv t_1 - t_2$ and noting that $\partial/\partial\bar{t} = \partial/\partial t_1 + \partial/\partial t_2$.

$$\frac{\partial}{\partial \bar{t}}\mathbf{G}^{<}(\bar{t},\Delta t) = i\left[\mathbf{G}^{<}(\bar{t},\Delta t)\mathbf{h}(\bar{t}-\frac{\Delta t}{2}) - \mathbf{h}(\bar{t}+\frac{\Delta t}{2})\mathbf{G}^{<}(\bar{t},\Delta t)\right] \tag{6.1}$$

The Fourier transform (eqn. 4.19) is applied to the re-expressed time domain K-B equation (eq. 6.1) to give,

$$\begin{aligned}\frac{\partial}{\partial \bar{t}}\mathbf{G}^{<}(\bar{t},\bar{\omega}) = \\ i\left[\mathbf{G}^{<}(\bar{t},\bar{\omega}),\mathbf{h}_0\right] + i\int d\omega'[\mathbf{G}^{<}(\bar{t},\bar{\omega}+\omega')\mathbf{v}(\bar{t},\omega') - \mathbf{v}(\bar{t},\omega')\mathbf{G}^{<}(\bar{t},\bar{\omega}-\omega')].\end{aligned} \tag{6.2}$$

where,

$$\mathbf{v}(\bar{t},\bar{\omega}) = \frac{1}{\pi}e^{-i2\bar{\omega}\bar{t}}\int_{-\infty}^{\infty} dt e^{i(2\bar{\omega})t}\mathbf{v}(t) = \frac{1}{\pi}e^{-i2\bar{\omega}\bar{t}}\tilde{\mathbf{v}}(2\bar{\omega}) \tag{6.3}$$

The combination of the two adjoined K-B equations (eq. 6.1) facilitates the use of time-dependent perturbation theory as the propagation method. Here, both the perturbation $\mathbf{v}(t)$ and $\mathbf{h_0}$ are Hermitian as they still represent the full (not truncated) system. Furthermore, we rewrite $\mathbf{G}^{<}(\bar{t},\bar{\omega})$ as the sum of a contribution in the absence of a perturbation $\mathbf{G}^{0,<}(\bar{\omega})$ and the remainder $\mathbf{\Delta G}^{<}(\bar{t},\bar{\omega}) \equiv \mathbf{G}^{<}(\bar{t},\bar{\omega}) - \mathbf{G}^{0,<}(\bar{\omega})$. The $\mathbf{G}^{0,<}(\bar{\omega})$ is $\bar{t}$ independent by definition of the GF (eq. 4.1). This allows us to rewrite eq. 6.2 in a form suitable for TDPT where the zeroth order term is the lesser GF in the absence of a perturbation (see appendix for further discussion):

$$\begin{aligned}\frac{\partial}{\partial \bar{t}}\mathbf{\Delta G}^{<}(\bar{t},\bar{\omega}) = \\ i\left[\mathbf{\Delta G}^{<}(\bar{t},\bar{\omega}),\mathbf{h}_0\right] + i\int d\omega'[\mathbf{G}^{<}(\bar{t},\bar{\omega}+\omega')\mathbf{v}(\bar{t},\omega') - \mathbf{v}(\bar{t},\omega')\mathbf{G}^{<}(\bar{t},\bar{\omega}-\omega')].\end{aligned} \tag{6.4}$$

We recast eq. (6.2) into an iterative equation by writing $\mathbf{G}^{<}(\bar{t},\bar{\omega})$ as a dressed form,

$$\mathbf{\Delta G}^{<}(\bar{t},\bar{\omega}) = \mathbf{e}^{-i\mathbf{h}_0(\bar{t}-t_0)}\mathbf{\Delta \mathcal{G}}^{<}(\bar{t},\bar{\omega})\mathbf{e}^{i\mathbf{h}_0(\bar{t}-t_0)}. \tag{6.5}$$

thus eliminating the terms with $\mathbf{h}_0$ in eq. (6.2) and leaving only the perturbing terms with $\mathbf{v}(\bar{t},\bar{\omega})$. The resulting time-differential equation is expressed as:

$$\frac{\partial}{\partial \bar{t}}\mathcal{G}^{<}(\bar{t},\bar{\omega}) = \tag{6.6}$$
$$i\int_{-\infty}^{\infty} d\omega' \mathbf{e}^{i\mathbf{h}_0(\bar{t}-t_0)}\left[\mathbf{G}^{<}(\bar{t},\bar{\omega}+\omega')\mathbf{v}(\bar{t},\omega') - \mathbf{v}(\bar{t},\omega')\mathbf{G}^{<}(\bar{t},\bar{\omega}-\omega')\right]\mathbf{e}^{-i\mathbf{h}_0(\bar{t}-t_0)}$$

Integrating provides:

$$\mathcal{G}^{<}(\bar{t},\bar{\omega}) = \mathcal{G}^{<}(t_\circ,\bar{\omega}) - i\int_{-\infty}^{\bar{t}} d\bar{t}' \int d\omega' \tag{6.7}$$
$$\left\{\mathbf{e}^{i\mathbf{h}_0(\bar{t}'-t_0)}\left[\mathbf{G}^{<}(\bar{t}',\bar{\omega}+\omega')\mathbf{v}(\bar{t}',\omega') - \mathbf{v}(\bar{t}',\omega')\mathbf{G}^{<}(\bar{t}',\bar{\omega}-\omega')\right]\mathbf{e}^{-i\mathbf{h}_0(\bar{t}'-t_0)}\right\}$$

Hence, the solution for this e.o.m. by time-dependent perturbation expansion is provided by:

$$\mathbf{G}^{<}(\bar{t},\bar{\omega}) = \mathbf{G}^{\mathbf{0},<}(\bar{\omega}) + \tag{6.8}$$
$$i\int_{t_0}^{\bar{t}} d\bar{t}' e^{-i\mathbf{h}_0(\bar{t}-\bar{t}')}\int d\omega'\left[\mathbf{G}^{<}(\bar{t}',\bar{\omega}+\omega')\mathbf{v}(\bar{t}',\omega') - \mathbf{v}(\bar{t}',\omega')\mathbf{G}^{<}(\bar{t}',\bar{\omega}-\omega')\right]\mathbf{e}^{i\mathbf{h}_0(\bar{t}-\bar{t}')}.$$

We note through an appropriate choice of $\mathbf{h}_0$ as discussed above, $\mathbf{G}^{<}(\bar{t},\bar{\omega}) = \mathbf{G}^{\mathbf{0},<}(\bar{\omega})$ in the absence of a perturbation. Thus, $\bar{t}$-independence of the initial GF is satisfied and no TD artifacts are introduced at the unperturbed conditions.

Here we also note that h_0 represents the full system and is still assumed to be Hermitian. However, upon defining a finite space for propagation and due to coupling to the bulks, non-hermitian terms have to be added to the propagation Hamiltonian. In the next subsection we implement a master equation, which properly represents the bulk effects within a finite (device) region. In treating molecular or nanoscale electron transport one naturally refers to the device region as the propagated space under the effect of coupling to the two electrodes.

A general master equation to project onto the device region is derived by rewriting

eq. 6.2:

$$
\begin{aligned}
i\frac{\partial}{\partial \bar{t}}\mathbf{\Delta G}^{<}_{cc}(\bar{t},\bar{\omega}) = &[\mathbf{h}_{cc}, \mathbf{\Delta G}^{<}_{cc}(\bar{t},\bar{\omega})] \\
&+ \int d\omega' [\mathbf{v_{cc}}(\bar{t},\omega')\mathbf{G}^{<}_{cc}(\bar{t},\bar{\omega}-\omega') - \mathbf{G}^{<}_{cc}(\bar{t},\bar{\omega}+\omega')\mathbf{v_{cc}}(\bar{t},\omega')] \\
&+ \int_{-\infty}^{\infty} dt' [\mathbf{\Sigma^R}(\bar{t}-t')\mathbf{\Delta G_{cc}}^{<}(t',\bar{\omega})e^{-i\mathbf{h_{cc}}(\bar{t}-t')} \\
&- e^{i\mathbf{h_{cc}}(\bar{t}-t')}\mathbf{\Delta G_{cc}}(t',\bar{\omega})\Sigma^A(t'-\bar{t})].
\end{aligned}
\tag{6.9}
$$

The subscript cc refers to the device central subspace and $G^{<}_{cc}(\bar{t},\bar{\omega}) = G^{0,<}_{cc}(\bar{\omega}) + \Delta G^{<}_{cc}(\bar{t},\bar{\omega})$. The full derivation of the last equation is provided in the appendix.

Wide Band Limit

We simplify the SE expressions by assuming

$$
\mathbf{\Sigma(t)} = \mathbf{\Sigma_0}\delta(\mathbf{t}).
\tag{6.10}
$$

The general master equation in the mixed representation (eq. 6.9) takes the following form:

$$
\begin{aligned}
i\frac{\partial}{\partial \bar{t}}\mathbf{\Delta G}^{<}_{cc}(\bar{t},\bar{\omega}) = &\left[(\mathbf{h}_{cc}+\mathbf{\Sigma^R_0})\mathbf{\Delta G}^{<}_{cc}(\bar{t},\bar{\omega}) - \mathbf{\Delta G}^{<}_{cc}(\bar{t},\bar{\omega})(\mathbf{h}_{cc}+\mathbf{\Sigma^A_0})\right] \\
&+ i\int_{-\infty}^{\infty} d\omega' [\mathbf{v_{cc}}(\bar{t},\omega')\mathbf{G}^{<}_{cc}(\bar{t},\bar{\omega}-\omega') - \mathbf{G}^{<}_{cc}(\bar{t},\bar{\omega}+\omega')\mathbf{v_{cc}}(\bar{t},\omega')].
\end{aligned}
\tag{6.11}
$$

This transforms the imaginary part of the general relation (eq. 6.8) by the appropriate decay factor. This leads to a time propagation equation, which is the WBL form of the general master equation (see eq. 6.9):

$$
\begin{aligned}
\mathbf{G}^{<}_{cc}(\bar{t},\bar{\omega}) = &\mathbf{G}^{0,<}_{cc}(\bar{\omega}) + i\int_{t_0}^{\bar{t}} d\bar{t}' \mathbf{e}^{-i(\mathbf{h}_{cc}+\mathbf{\Sigma^R_0})(\bar{t}-\bar{t}')} \int d\omega' \times \\
&[\mathbf{G}^{<}_{cc}(\bar{t}',\bar{\omega}+\omega')\mathbf{v_{cc}}(\bar{t}',\omega') - \mathbf{v_{cc}}(\bar{t}',\omega')\mathbf{G}^{<}_{cc}(\bar{t}',\bar{\omega}-\omega')]\, \mathbf{e}^{i(\mathbf{h}_{cc}+\mathbf{\Sigma^A_0})(\bar{t}-\bar{t}')}.
\end{aligned}
\tag{6.12}
$$

The complexity in this expression is due to the convolution integral in $\bar{\omega}$ and the infinite nature of the system contributing dissipation effects. We use TD perturbation theory to simplify the full propagation solution for $(\mathbf{G}^{<}(\bar{t},\bar{\omega}))$. The first order treatment corresponds to single photon transition dynamics, or alternatively, yields the conductance at zero bias for a simple potential bias perturbation. A second order expansion is required to treat two photon excitations. The first order TD expansion of the GF is:

$$\begin{aligned}\mathbf{G}^{<}_{cc}(\bar{t},\bar{\omega}) =&\mathbf{G}^{0,<}_{cc}(\bar{\omega}) + i\int_{t_0}^{\bar{t}} d\bar{t}'\mathbf{e}^{-i(\mathbf{h}_{cc}+\Sigma^{R}_{0})(\bar{t}-\bar{t}')}\int d\omega'\times \\ &\left[\mathbf{G}^{0,<}_{cc}(\bar{\omega}+\omega')\mathbf{v}_{cc}(\bar{t}',\omega') - \mathbf{v}_{cc}(\bar{t}',\omega')\mathbf{G}^{0,<}_{cc}(\bar{\omega}-\omega')\right]\mathbf{e}^{i(\mathbf{h}_{cc}+\Sigma^{A}_{0})(\bar{t}-\bar{t}')}\end{aligned} \tag{6.13}$$

where $\mathbf{G}^{0,<}_{cc}(\bar{\omega})$ is the propagated (zeroth order) GF. At any given time step, $\bar{t}=t_n$, $\mathbf{G}^{<}(\bar{t},\bar{\omega})$ can be updated from the previous time step, t_{n-1}, with a proper shift by the propagator. We also note that, for simulations involving a larger time-step to pulse duration ratio, fewer frequency convolution data points are required for obtaining a well converged result. This leads to an efficient and manageable simulation. Here, this mixed representation is used in evaluating the current on a model system as described next.

6.2 The two-frequency representation

The two-frequency representation of the formalism allows for the treatment of electrodes via self energies of non-trivial energy dependence on the same level as the time independent Hamiltonian. Equations of motion are derived for the quantity:

$$\boldsymbol{G}^{<}(\Delta\omega,\bar{\omega}) \equiv \int_{-\infty}^{\infty} d\bar{t}e^{i\Delta\omega\bar{t}}\boldsymbol{G}^{<}(\bar{t},\bar{\omega}) \tag{6.14}$$

One can then retrieve the mixed representation by Fourier transforming $\Delta\omega$ back to $\bar{t}$. Alternatively, one may propagate the mixed representation using a finite difference method. This method, however, requires the calculation of the memory term at

every $\bar{t}$ and $\bar{\omega}$. This approach becomes ideally suited for short times and necessary for driving fields strong enough so that a Rabi oscillation cannot be approximated by an n-th order time dependent perturbation expansion within the temporal domain of interest. However, such an approach can become expensive at moderate to long times because the memory term must be calculated for every time and frequency. Even in the case of short pulses, there is a limit defined by the time-energy uncertainty principle that requires us to include larger domains in $\bar{\omega}$ for smaller domains in $\bar{t}$. For all of these reasons, a two-frequency approach is more suited to weak fields of moderate to long temporal duration since the memory term is much easier to calculate in this representation for such problems. However, the two frequency approach presents an interesting dilemma to be described in the derivation. This dilemma involves a choice between artificially imposing the equilibrium constraint (sec 3.2) or introducing high frequency oscillations into the two frequency spectrum.

6.2.1 Equation of Motion

One may choose to Fourier transform the generalized quantum master equation in the mixed representation (eq. 6.9). However, Fourier transforming the time derivative term in eq. 6.9 will introduce the term $\mathbf{\Delta G}^{<}_{cc}(\bar{t} \rightarrow \infty, \bar{\omega})$, producing an equation that requires knowledge of the very solution that is being sought. Such an approach would be acceptable if the equilibrium assumption (sec. 3.2) is made at the microcanonical level. Then the term $\mathbf{\Delta G}^{<}_{cc}(\bar{t} \rightarrow \infty, \bar{\omega})$, would exactly cancel with the term $\mathbf{\Delta G}^{<}_{cc}(\bar{t} \rightarrow -\infty, \bar{\omega})$, that is also introduced by Fourier transforming the time derivative term in eq. 6.9. Thus, a formalism that is independent of both, the equilibrium assumption and the need for a-priori knowledge of the final solution requires a different starting point, namely, the integrated form of eq. 6.9 in the

representation where $\mathbf{h}_{cc}$ is diagonalized,

(6.15)

$$
\begin{aligned}
i\Delta G^{<}_{cc,ij}(\bar{t},\bar{\omega}) = & \\
& \int_{-\infty}^{\infty} dt'\,\Theta(\bar{t}-t')e^{-i\Delta\epsilon_{ij}(\bar{t}-t')}\times \\
& \left\{\int d\omega'[\mathbf{v_{cc}}(t',\omega')\mathbf{G}^{<}_{cc}(t',\bar{\omega}-\omega') - \mathbf{G}^{<}_{cc}(t',\bar{\omega}+\omega')\mathbf{v_{cc}}(t',\omega')]_{ij}\right\} \\
& + \int_{-\infty}^{\infty}\Theta(\bar{t}-t')e^{-i\Delta\epsilon_{ij}(\bar{t}-t')}\int_{-\infty}^{\infty}dt''\sum_{k,l}[\Gamma_{ijkl}(t'-t'')\Delta G^{<}_{cc,kl}(t'',\bar{\omega})]
\end{aligned}
$$

where $t_0 \to -\infty$ and $\int_{-\infty}^{\bar{t}} dt' \to \int_{-\infty}^{\infty} dt'\Theta(\bar{t}-t')$ and the electron reservoirs (electrodes) are described by a memory kernel of the form,

$$
\Gamma_{ijkl}(t) \equiv \Sigma^{R}_{ik}(t)e^{i\epsilon_j t}\delta_{lj} - \Sigma^{A}_{lj}(-t)e^{-i\epsilon_i t}\delta_{ik} \tag{6.16}
$$

Applying the Fourier transform to eqn. 6.15 gives

$$
\begin{aligned}
\Delta G^{<}_{CC,ij}(\Delta\omega,\bar{\omega}) = & \\
& \mathcal{G}_{ij}(\Delta\omega)\left[\mathbf{v}_{CC}(\Delta\omega)\mathbf{G}^{0,<}_{CC}(\bar{\omega}-\Delta\omega/2) - \mathbf{G}^{0,<}_{CC}(\bar{\omega}+\Delta\omega/2)\mathbf{v}_{CC}(\Delta\omega)\right]_{ij} \\
& + \frac{1}{\pi}\mathcal{G}_{ij}(\Delta\omega)\int d\omega'[\mathbf{v}_{CC}(2\omega')\boldsymbol{\Delta G}^{<}_{CC}(\bar{\omega}-\omega',\Delta\omega-2\omega') \\
& - \boldsymbol{\Delta G}^{<}_{CC}(\bar{\omega}+\omega',\Delta\omega-2\omega')\mathbf{v}_{CC}(2\omega')]_{ij} \\
& + \mathcal{G}_{ij}(\Delta\omega)\sum_{k,l}\Gamma_{ijkl}(\Delta\omega)\Delta G^{<}_{cc,kl}(\Delta\omega,\bar{\omega})
\end{aligned} \tag{6.17}
$$

where,

$$
\Gamma_{ijkl}(\Delta\omega) \equiv \int dt e^{i\Delta\omega t}\Gamma_{ijkl}(t) = \Sigma^{R}_{ik}(\epsilon_j+\Delta\omega)\delta_{lj} - \Sigma^{A}_{lj}(\epsilon_i-\Delta\omega)\delta_{ik} \tag{6.18}
$$

Note that

$$
\mathcal{G}_{ij}(\Delta\omega) \equiv -i\int_{-\infty}^{\infty} dt e^{i\Delta\omega t}\Theta(t)e^{-i\Delta\epsilon_{ij}t} = \frac{1-e^{i(\Delta\omega-\Delta\epsilon_{ij})(t\to\infty)}}{\Delta\omega-\Delta\epsilon_{ij}} \tag{6.19}
$$

The exponential term $e^{i(\Delta\omega-\epsilon_{ij})(t\to\infty)}$ is formally significant because it accounts for the non-equilibrium nature of the system. Namely, it preserves the fact that the

final state is not necessarily the same as the initial state, as discussed in section 3.2. This term does, however introduce oscillations of infinite frequency in this spectral picture, making it potentially difficult to analyze spectra. Thus, here we take the typical approach prescribed to Green functions expressed in the frequency domain. We introduce a small positive broadening η that allows $e^{i(\Delta\omega-\epsilon_{ij})(t\to\infty)} \to 0$. In this case, the retarded propagator above becomes

$$\mathcal{G}_{ij}(\Delta\omega) = \frac{1}{\Delta\omega + i\eta - \Delta\epsilon_{ij}} \tag{6.20}$$

However, this broadening has the effect of ensuring that eventually ($t \to \infty$) the state will return to its initial equilibrium configuration. Ironically, it imposes the equilibrium assumption described in section 3.2. In practice, any finite grid method in the frequency domain requires an artificial broadening to resolve infinitesimally narrow peaks (discrete states) and an artificial equilibrium constraint is inadvertently imposed. On the other hand, the broadening can be considered realistic if it approximates thermal effects within the system (e.g. vibrational collisions) that replenish the discrete state in a thermal lifetime. The present formalism uses the approach of including a broadening and assumes that the temporal range of the calculation is large enough to include the system's approach to equilibrium.

Finally, this gives

$$\begin{aligned}\sum_{k,l} \boldsymbol{\mathcal{H}}_{ijkl}(\Delta\omega)\boldsymbol{\Delta G}^{<}_{CC,kl}(\Delta\omega,\bar{\omega}) = \\ \big[\mathbf{v}_{CC}(\Delta\omega)\mathbf{G}^{0,<}_{CC}(\bar{\omega}-\Delta\omega/2) - \mathbf{G}^{0,<}_{CC}(\bar{\omega}+\Delta\omega/2)\mathbf{v}_{CC}(\Delta\omega)\big]_{ij} \\ +\frac{1}{\pi}\int d\omega' [\mathbf{v}_{CC}(2\omega')\boldsymbol{\Delta G}^{<}_{CC}(\bar{\omega}-\omega',\Delta\omega-2\omega') \\ -\boldsymbol{\Delta G}^{<}_{CC}(\bar{\omega}+\omega',\Delta\omega-2\omega')\mathbf{v}_{CC}(2\omega')]_{ij}\end{aligned} \tag{6.21}$$

where

$$\boldsymbol{\mathcal{H}}_{ijkl}(\Delta\omega) \equiv (\Delta\omega + i\eta - \Delta\epsilon_{ij})\delta_{ik}\delta_{jl} - \Gamma_{ijkl}(\Delta\omega) \tag{6.22}$$

These equations can be expanded by substitution to n-th order in the perturbing potential as was done before.

6.2.2 A Practical Note: Tetradic Notation

We note that eqn. 6.21 involves a tensor of rank four that operates on a matrix (tensor of rank 2). We now introduce the use of tetradic notation, which allows us to write such equations in a simple form and provides a means by which to solve such equations. In short, tetradic notation re-expresses matrices as vectors and rank four tensors as matrices. Thus, an $n \times n$ matrix $\mathbf{A}$ with elements A_{ij} can be rewritten as a vector $|A\rangle\rangle$ with elements $|A\rangle\rangle_{ni+j}$. Likewise, a tensor $\mathcal{H}$ with element $\mathcal{H}_{ijkl}$ (where i, j, k, l each spans over n elements), can be rewritten as an $n^2 \times n^2$ matrix $\mathbf{H}$, with elements $\mathbf{H}_{ni+j,nk+l}$. Note, from eqn. 6.21 that matrix multiplication is correctly preserved within this notation. Thus, we can rewrite eqn. 6.21 concisely in tetradic notation,

$$\begin{aligned} &\mathbf{H}(\Delta\omega)|\boldsymbol{\Delta G}^{<}_{CC}(\Delta\omega,\bar{\omega})\rangle\rangle = \\ &\quad |B^{(1)}_{CC}(\Delta\omega,\bar{\omega})\rangle\rangle \\ &\quad +\frac{1}{\pi}\int d\omega' |B_{CC}(\omega',\Delta\omega,\bar{\omega})\rangle\rangle \end{aligned} \tag{6.23}$$

where,

$$\mathbf{H}_{ni+j,nk+l}(\Delta\omega) \equiv \boldsymbol{\mathcal{H}}_{ijkl}(\Delta\omega) \tag{6.24}$$

$$|\boldsymbol{\Delta G}^{<}_{CC}(\Delta\omega,\bar{\omega})\rangle\rangle_{ni+j} \equiv \boldsymbol{\Delta G}^{<}_{CC,ij}(\Delta\omega,\bar{\omega}) \tag{6.25}$$

(6.26)

$$|B^{(1)}_{CC}(\Delta\omega,\bar{\omega})\rangle\rangle_{ni+j} \equiv \left[\mathbf{v}_{CC}(\Delta\omega)\mathbf{G}^{0,<}_{CC}(\bar{\omega}-\Delta\omega/2) - \mathbf{G}^{0,<}_{CC}(\bar{\omega}+\Delta\omega/2)\mathbf{v}_{CC}(\Delta\omega)\right]_{ij}$$

$$
\begin{aligned}
&|B_{CC}(\omega', \Delta\omega, \bar{\omega})\rangle\rangle_{ni+j} \equiv \\
&[\mathbf{v}_{CC}(2\omega')\boldsymbol{\Delta G}^{<}_{CC}(\bar{\omega}-\omega', \Delta\omega - 2\omega') - \boldsymbol{\Delta G}^{<}_{CC}(\bar{\omega}+\omega', \Delta\omega - 2\omega')\mathbf{v}_{CC}(2\omega')]_{ij}
\end{aligned} \tag{6.27}
$$

Inverting $\mathbf{H}(\Delta\omega)$ gives,

$$
\begin{aligned}
|\boldsymbol{\Delta G}^{<}_{CC}(\Delta\omega, \bar{\omega})\rangle\rangle = \\
&\mathbf{G}(\Delta\omega)|B^{(1)}_{CC}(\Delta\omega, \bar{\omega})\rangle\rangle \\
&+\frac{1}{\pi}\mathbf{G}(\Delta\omega)\int d\omega' |B_{CC}(\omega', \Delta\omega, \bar{\omega})\rangle\rangle
\end{aligned} \tag{6.28}
$$

where

$$
\mathbf{G}(\Delta\omega) \equiv \mathbf{H}^{-1}(\Delta\omega) \tag{6.29}
$$

Thus, tetradic notation allows for a notationally simple expression for the equation of motion. In addition, though, it also generates an equation that can easily be inverted and solved as a perturbation expansion both formally and computationally. A tensor equation becomes a matrix equation and all matrix operations (multiplication, inversion, diagonalization, etc.) can be applied to this equation of motion.

6.2.3 Special Case: Constant Potential Theory

We now discuss a way in which we can derive the steady state result for a time independent perturbation, such as a bias that has been turned on for a long time. We note that a time independent perturbation $\mathbf{v}(t) = \mathbf{v}_\circ$ can be Fourier transformed as in eqn. 6.14. Its counterpart in the frequency domain is

$$
\mathbf{v}(\Delta\omega) = 2\pi\delta(\Delta\omega)\mathbf{v}_\circ \tag{6.30}
$$

We will use the two-frequency representation of the time-dependent equations of motion to derive a time-independent correction to $G^{0,<}$.

Example: First order time-independent perturbation expansion

Truncating eqn. 6.28 to first order in $\mathbf{v}(\Delta\omega)$ and substituting eqn. 6.30 gives

$$|\boldsymbol{\Delta G}^{<}_{CC}(\Delta\omega,\bar{\omega})\rangle\rangle = 2\pi\delta(\Delta\omega)\mathbf{G}(0)|B^{(1)}_{CC}(\bar{\omega})\rangle\rangle \tag{6.31}$$

where

$$|B^{(1)}_{CC}(\bar{\omega})\rangle\rangle_{ni+j} \equiv \left[\mathbf{v}_{\circ}\mathbf{G}^{0,<}_{CC}(\bar{\omega}) - \mathbf{G}^{0,<}_{CC}(\bar{\omega})\mathbf{v}_{\circ}\right]_{ij} \tag{6.32}$$

one can thus use the expression

$$|\mathbf{G}^{0,<}_{CC}(\bar{\omega})\rangle\rangle \rightarrow |\mathbf{G}^{0,<}_{CC}(\bar{\omega})\rangle\rangle + \mathbf{G}(0)|B^{(1)}_{CC}(\bar{\omega})\rangle\rangle \tag{6.33}$$

as an initial guess steady state lesser Green function that introduces the effects of weak bias $\mathbf{v}_{\circ}$.

Exact solution

One can treat time independent fields (such as a source-drain bias that has been turned on for a long time) exactly by reformulating eqn. 6.23 to include the effects of such a field without the need to impose any restrictions on the field strength (see appendix C for a detailed derivation). An interesting point, here, is that one cannot simply include the constant perturbation within the initial lesser Green function $G^{0,<}(\bar{\omega})$. One must solve the time dependent equation of motion and then impose the limit of a time independent perturbation. Without loss of generality, the perturbing potential $\mathbf{v}(t)$ can be rewritten as the sum of a time-independent field (of arbitrary strength) $\mathbf{v}_{\circ}$ and a time dependent perturbing field $\mathbf{v}_{TD}(t)$. Fourier transforming to the frequency domain gives,

$$\mathbf{v}(\Delta\omega) = 2\pi\delta(\Delta\omega)\mathbf{v}_{\circ} + \mathbf{v}_{TD}(\Delta\omega) \tag{6.34}$$

The resulting two-frequency equation of motion becomes

$$\begin{aligned}\mathbf{H}_{v_\circ}(\Delta\omega)|\boldsymbol{\Delta G}^{<}_{TD,CC}(\Delta\omega,\bar{\omega})\rangle\rangle = \\ |B^{(1)}_{TD,CC}(\Delta\omega,\bar{\omega})\rangle\rangle \\ +\frac{1}{\pi}\int d\omega' |B_{TD,CC}(\omega',\Delta\omega,\bar{\omega})\rangle\rangle\end{aligned} \tag{6.35}$$

where the propagating super operator,

$$\mathbf{H}_{v_\circ,ni+j,nk+l}(\Delta\omega) \equiv \boldsymbol{\mathcal{H}}_{ijkl}(\Delta\omega) - (v_{\circ,ik}\delta_{lj} - v_{\circ,lj}\delta_{ik}) \tag{6.36}$$

now includes the perturbation within the Hamiltonian. The total lesser Green function is now defined in terms of a new time independent initial guess $G^{0,<}_{v_\circ}$ that includes the effects of the time-independent field exactly. In the absence of additional time-dependent perturbations, $G^{0,<}_{v_\circ}$ is the total lesser Green function for the system. The remainder, $\Delta G^{<}_{TD}$, is due solely to these remaining time dependent perturbations,

$$|\boldsymbol{\Delta G}^{<}_{TD,CC}(\Delta\omega,\bar{\omega})\rangle\rangle \equiv |G^{<}_{CC}(\Delta\omega,\bar{\omega})\rangle\rangle - 2\pi\delta(\Delta\omega)|G^{0,<}_{v_\circ,CC}(\bar{\omega})\rangle\rangle \tag{6.37}$$

where,

$$|G^{0,<}_{v_\circ,CC}(\bar{\omega})\rangle\rangle = |G^{0,<}_{CC}(\bar{\omega})\rangle\rangle + \mathbf{G}_{v_\circ}(0)|B^{(1)}_{v_\circ,CC}(\bar{\omega})\rangle\rangle. \tag{6.38}$$

Here, $\mathbf{G}_{v_\circ}(\Delta\omega) = \mathbf{H}^{-1}_{v_\circ}(\Delta\omega)$ and

$$|B^{(1)}_{v_\circ,CC}(\bar{\omega})\rangle\rangle_{ni+j} \equiv \left[\mathbf{v}_{\circ,CC}\mathbf{G}^{0,<}_{CC}(\bar{\omega}) - \mathbf{G}^{0,<}_{CC}(\bar{\omega})\mathbf{v}_{\circ,CC}\right]_{ij}. \tag{6.39}$$

The time dependent "B"-terms are written as before, only they now depend on the modified initial guess $G^{0,<}_{v_\circ}$ and the remaining time-dependent perturbations $v_{TD}(\Delta\omega)$.

(6.40)

$$\begin{aligned}|B^{(1)}_{TD,CC}(\Delta\omega,\bar{\omega})\rangle\rangle_{ni+j} \equiv \\ \left[\mathbf{v}_{TD,CC}(\Delta\omega)\mathbf{G}^{0,<}_{v_\circ,CC}(\bar{\omega}-\Delta\omega/2) - \mathbf{G}^{0,<}_{v_\circ,CC}(\bar{\omega}+\Delta\omega/2)\mathbf{v}_{TD,CC}(\Delta\omega)\right]_{ij}\end{aligned}$$

$$|B_{TD,CC}(\omega', \Delta\omega, \bar{\omega})\rangle\rangle_{ni+j} \equiv$$

$$[\mathbf{v}_{TD,CC}(2\omega')\boldsymbol{\Delta G}^{<}_{TD,CC}(\Delta\omega - 2\omega', \bar{\omega} - \omega') \tag{6.41}$$

$$- \boldsymbol{\Delta G}^{<}_{TD,CC}(\Delta\omega - 2\omega', \bar{\omega} + \omega')\mathbf{v}_{TD,CC}(2\omega')]_{ij}$$

Equations 6.23 and 6.35 are identical in form. Thus, the code used for calculating eqn. 6.23 can be used for computing eqn 6.35 with very few modifications. The effect of $\mathbf{v}_\circ$ enters explicitly only into the Hamiltonian super operator $\mathbf{H}(\Delta\omega) \rightarrow \mathbf{H}_{v_\circ}(\Delta\omega)$ and the initial lesser GF $G^{0,<} \rightarrow G^{0,<}_{v_\circ}$. However, as pointed out above, the form for $G^{0,<}_{v_\circ}$ (eqn. 6.38) is less trivial than simply using $G^{0,<}$ with the perturbation inserted into the Hamiltonian. The effect of a source-drain bias on an initially incoherent electronic charge density cannot be modeled by a simple field asymmetry embedded within the Hamiltonian.

CHAPTER VII

Model calculations

7.1 Linear Response and Wide Band Limit

Models

We concentrate in this study on the TD conductance effect through a one dimensional wire composed of hopping sites. We assume a tight-binding scenario where interactions are included only between neighbor sites. The device region is defined after dividing the system to three regions, where the central region is the device bonded to two semi-infinite bulk-wires. In the results reported below we include two sites to define the device region. An illustration of this system along with the relevant electronic parameters is provided in Figure 7.1. We note that β and s are the electronic and overlap coupling terms. The diagonal terms of the model Hamiltonian are set to the initial Fermi energy of the system. Accordingly, we express the current operator (see next section for further detailed discussion) with the numerical values assigned to the electronic integrals in the Hamiltonian

$$\mathbf{O} = \mathbf{i} \begin{bmatrix} 0 & \beta_d \\ -\beta_d & 0 \end{bmatrix}. \tag{7.1}$$

In all calculations reported below in the results section we set the FE to zero ($\mu_0 = 0$). This also defines the on site energies as described in the figure. We have also used, for the electronic coupling terms, unless differently specified: $\beta_d = 0.25eV, \beta_l =$

Figure 7.1: One dimensional wire composed of an array of hopping sites. The central region corresponds to the device, which can be set to different site to model doping. The coupling terms within the device are denote as β_d, coupling of the device-bulk β_l and β for the bulk region. Corresponding s terms for the overlap are defined as well.

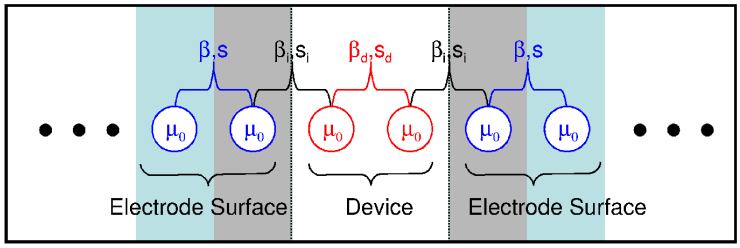

$\beta_r = 0.25eV$. We use a sufficiently small value ($\eta_d = 0.005eV$) for the fundamental broadening factor added to the imaginary component of the Hamiltonian used to calculate the G_0^R ($\eta_d = \eta$ in eq. 5.10). This describes the unperturbed equilibrated system. The bulk GF is associated with another fundamental broadening factor (η_b) of effectively 0.025eV when the mixing parameter is 0.25eV (see eq. 5.34). For selectively tuning the broadening of only the open channels and leaving the bound states unaffected, η_b is modified while η_d is kept constant. Finally, we note that in all calculations the target bias potential is set to 0.2eV.

Models

The steady state defines the unperturbed system and therefore serves as the initial point of the time propagation treatment. The proper thermalization of the full system has to be treated well in the $\mathbf{G}^{0,<}(\bar{\omega})$ as explained above using the SEs (eqns. 5.11 and 5.12). We comment also that the projected Fermi matrix to the device region needs to include correction terms due to the coupling to the bulk:

$$\bar{\mathbf{f}} \rightarrow \bar{\mathbf{f}}_{\mathbf{cc}} - (\bar{\omega}\mathbf{S}_{\mathbf{cl}} - \bar{\mathbf{h}}_{\mathbf{cl}})\bar{\mathbf{g}}_{\mathbf{ll}}^{\mathbf{R}}\bar{\mathbf{f}}_{\mathbf{lc}} - (\bar{\omega}\mathbf{S}_{\mathbf{cr}} - \bar{\mathbf{h}}_{\mathbf{cr}})\bar{\mathbf{g}}_{\mathbf{rr}}^{\mathbf{R}}\bar{\mathbf{f}}_{\mathbf{rc}} \tag{7.2}$$

These terms are found to involve a negligible effect with the models used below.

The electronic density propagation is specialized to the mixed representation. In

this representation an analytical expression as derived next is obtained within a wide-band-limit treatment. This WBL is appropriate for analyzing the dependence of the transient transport on the key parameters of the electronic channels.

Current evaluation

We now describe the evaluation of the current from the time propagated $G^<$ function. In the second quantized representation, most dynamical variables (e.g. dipole, spin and current operators) can be expressed in terms of one pair of field operators (see also eq. 3.7 and 3.8)

$$\hat{O} = \int_{-\infty}^{\infty} d\vec{x} \hat{\psi}^\dagger(\vec{x}) \mathcal{O}(\vec{x}) \hat{\psi}^(\vec{x}) \tag{7.3}$$

where the function $\mathcal{O}(\vec{x})$ is the one-particle case for a many body operator. For example, given the number density operator for a system of N particles at position $\vec{r}$, where $\sum_{n=1}^{N} \delta(\vec{x}_n - \vec{r})$, $\hat{O}$ becomes $\mathcal{O}(\vec{x}) = \delta(\vec{x} - \vec{r})$. The grand canonical expectation value of any dynamical variable (see eq. 3.7) is given by

$$\langle \hat{O}(t_1) \rangle = -i \int_{-\infty}^{\infty} d\vec{x}_1 \lim_{x_2 \to x_1} [\mathcal{O}(\vec{x}_1) G^<(x_1, x_2)] \tag{7.4}$$

Given the basis set representation, eq (4.65), this expectation value can be expressed as a product of two matrices

$$\begin{aligned} \langle \mathbf{O}(t_1) \rangle = -iTr \left[\lim_{t_2 \to t_1} [\mathcal{O}\mathbf{G}^<(t_1, t_2)] \right] = -iTr \left[\lim_{\Delta t \to 0, \bar{t} \to t_1} [\mathcal{O}\mathbf{G}^<(\bar{t}, \Delta t)] \right] = \\ Tr \left[\lim_{\bar{t} \to t_1} \left[\frac{-i}{2\pi} \int_{-\infty}^{\infty} d\bar{\omega} \mathcal{O}\mathbf{G}^<(\bar{t}, \bar{\omega}) \right] \right], \end{aligned} \tag{7.5}$$

where $\mathcal{O}_{\mathbf{ij}} = \int_{-\infty}^{\infty} \mathbf{d\tilde{x}} \phi_{\mathbf{i}}(\tilde{\mathbf{x}}) \mathcal{O}(\tilde{\mathbf{x}}) \phi_{\mathbf{j}}(\tilde{\mathbf{x}})$. Let us now consider the specific case of the current density operator. One can show that, for this operator,

$$\mathcal{O}(\vec{x}) = -i \left[\vec{\nabla}_x \delta(\vec{x} - \vec{r}) + \delta(\vec{x} - \vec{r}) \vec{\nabla}_x \right] \tag{7.6}$$

The current density operator is position dependent. It can be expressed in an LCAO basis

$$\mathcal{O}_{ji}(\vec{r}) = i\left[\phi_i(\vec{r})\vec{\nabla}\phi_j(\vec{r}) - \phi_j(\vec{r})\vec{\nabla}\phi_i(\vec{r})\right] \tag{7.7}$$

and, in matrix form, is Hermitian under permutation of the indices i and j. The electron current through a given plane is calculated by tracing $[-i\mathcal{O}\mathbf{G}^<]$. This trace, which is the vector current density defined in an AO basis, is then expressed on a spatial grid. The current is finally obtained by integrating over the plane, which is perpendicular to the flux direction.

The conductance due to electronic transmittance through a single quantum channel is analyzed for transient effects. We use the parameters as listed in the "Models" section, where only η_b is effectively increased by a factor of 3. We start by demonstrating the dramatic effect of the applied time-shaped potential pulse. In Figure 7.2, conductance due to four potential pulses are provided. In all cases, for convenience, a sufficiently slow turn-on events (elapsing 15 fs) are followed by differing time-durations at the target bias and/or differing turn-off rates. (The 15 fs corresponds to about 3 periods of a system characterized by 1eV transition energy. We analyze below in detail its relative adiabatic nature as determined in reference to other system parameters.) The responding current evolves to steady state upon a long enough constant bias. We study the effect of turning off the pulse adiabatically versus applying an abrupt perturbation on the achieved steady state current under the target potential bias. All potential switching slopes are defined by one quarter of a sinus function stretched over different time periods and, therefore, are described by continuous and analytical functions. The actual potential ramping profiles are illustrated in the left of the figure. An additional curve which includes also bound states is provided for comparison.

Figure 7.2: TD conductance ($I(t)$) due to three different pulses is studied. All pulses correspond to an analytical TD potential bias function, where the same rate is used for the turn-on (elapsing 15 fs). They differ in the rate of the turn-off and the length of the pulse at the target bias. An I(t) for a case with bound states is also provided: (i) Black line: slow rate of turn off (15fs) (ii) Red line with plus symbols: shorter pulse at target. (iii) Green line with circles: fast turn off pulse (elapsing 1fs). (iv) like (i) with two additional bound states. (**Left**) The potential ramping profiles are illustrated.

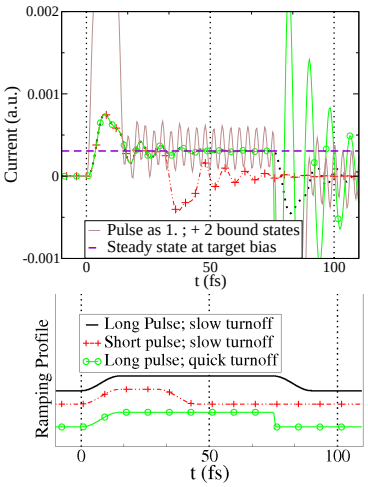

First we draw attention to the current under constant potential bias. All $I(t)$ curves achieve the same steady state current, as expected, since all ramping potentials are set to the same bias target. The related steady state currents are evaluated by $I(V) = \frac{V}{2} g_0 (\frac{\beta_d \Sigma}{(\beta_d^2 + \Sigma^2)})$, where $g_0 = e^2/h$ (a factor of two would be added to account for the spin degree of freedom), V is the voltage drop and β_d and Σ are the electronic coupling and bulk self energies respectively as defined above. These corresponding steady state currents are confirmed to agree with the long time limit of the propagation when the applied TD bias is constant for a sufficiently long time. The AC response component is shown to decay due to the bulk dephasing effects. In all cases involving (sufficiently) adiabatic switching, the amplitude of the transient AC response is much smaller than the developed DC. The added bound states are shown to result with persisting oscillations as the bulk is not effective in dissipating their effect on the conductance. We focus, next, on the effect of pulse duration on

the conductance.

In Figure 7.3 we provide the TD conductance for three pulses that differ only in the length of the pulse. The conductance of the three pulses are shown (right panel) to correspond to the same developing steady state. We are also providing the corresponding $(\bar{t}, \bar{\omega})$ Wigner distributions of the current in a form of a projection on a color scheme (left three panels). The current distributions are the integrand in equation 7.5 evaluating the TD expectation value of the current (see equation 7.4). In the figure, two rows with varying color-plot scales are provided. In the upper row we use a scale to provide an overall view of the distribution. The switching events' signature is clearly visible. In the lower row we use a smaller scale, highlighting the steady pulse region while including the switching events. The contributions of both the AC and DC components to the steady state current can now easily be distinguished.

We also note that the Wigner current distributions exhibit quantum broadening (smearing), where, for example, the response to the voltage pulse seems to begin before pulse initiation. This is a direct consequence of time-energy uncertainty principle. A real (quantum) probe cannot provide the behavior of the current energy-density at a specific time. This is also evident by observing the current which is obtained by integrating the Wigner current distribution over $\bar{\omega}$ (fig. 7.3). The current is shown to begin at the correct time as expected for a physical observable. The current distributions provide insight at the quantum mechanical level on the identified DC and the ringing components of the TD current response.

We focus now on the DC component of the conductance response and analyze it using the current distributions. In Figure 7.3 the conductance of the two site model is shown to be dominated by one open channel. The transient conductance, as observed

Figure 7.3: Time span at the target bias study: (i) short pulse (50fs) (ii) medium pulse (100fs) (iii) long pulse (200fs) **Left panel:** I(t) curves. **3 Right Panel:** Current distribution with differing color maps between the lower and upper panels.

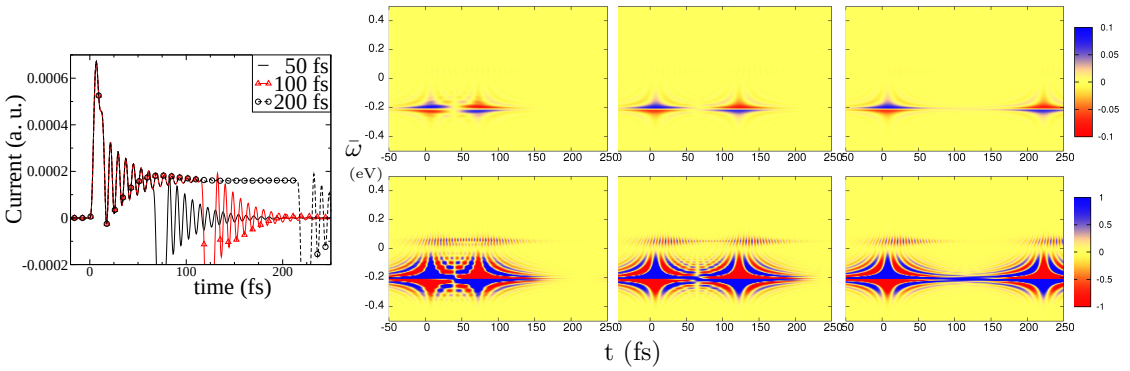

upon switching on, is shown to emerge from the related band, where the positive sign is associated with the upper portion (in energy) of the band. The lower part of the band is shown to dissipate at long enough time following the switching event leading eventually to the steady state. At the steady state only positive current contributions are noted. The switching off event is essentially characterized by mirroring the band structure of the switch-on event, where the upper part of the band becomes the negative conduction contributions. The AC component as analyzed next emerges due to interferences between the existing channels.

We consider again Figure 7.2 focusing on the turn-off event. It is interesting to note that an AC response component may persist over several cycles after the turn off event depending on the switching rate. For the slower switching rates the number of the ringing oscillations and their amplitudes become smaller. The Green curve with circles corresponds to the current under a fast rate for the potential turn off (elapsing 1fs). This relatively abrupt change leads to a strong ringing mode with amplitudes which exceed the prior DC current by an order of magnitude. This is a very strong oscillating response and its dissipation may extend over several periods depending on the details of the electronic parameters and the TD details of the perturbation.

Figure 7.4: Switch off rate study: (i) slow switching rate (30fs) (ii) medium (15 fs) (iii) quick rate (1 fs). **Left panel:** I(t) curves. **3 Right Panel:** Current distributions with differing color maps between the lower and upper panels.

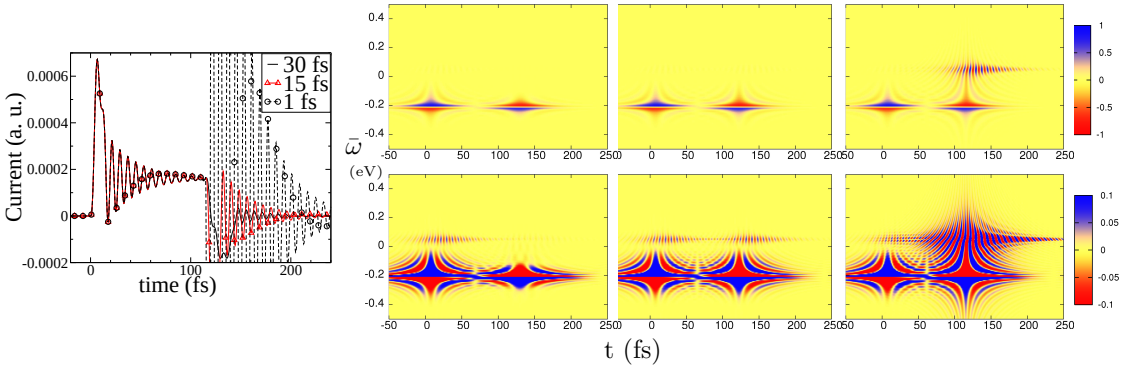

In addition, the presence of bound states as shown in the figure results with the persistence of the AC oscillations. This aspects are further analyzed below.

A strong perturbation applied on a developed steady state leads to a TD current dominated by the AC component. This clearly has an important effect on the functionality of molecular and nano scale devices. In Figure 7.4 we provide several I(t) curves, which demonstrate the dramatic dependence of the decay time on the bias-switching rate. We emphasize that even with the slowest switching case a strong transient negative current upon turnoff is observed. The first negative amplitude in absolute value exceeds the prior steady state current for the relatively slow switching event over 15fs. The slowest case involving switching over 30fs reaches about the same value as the steady state current for the same responding amplitude, and shows, as expected, the smallest number of oscillations prior to settling on the zero current. Next, we consider the corresponding Wigner current distributions under differing rates of the turn off event.

In Figure 7.4 we compare the Wigner forms of the current for cases differing significantly in the bias turn off rate. The Wigner current distribution of the most abrupt case is shown on the rightmost color map panel. The resulting strong oscillations

following the switching event are an order of magnitude larger than the calculated preceding DC values. We, therefore, include (in the lower panel) the current distribution at times where the DC component is still dominant. We use a color-map scale that highlights the AC oscillations in this temporal domain (lower row). The ringing and steady-state AC responses are both concentrated about the same value of $\bar{\omega}$. This value corresponds to an energy shift relative to the electronic level of the propagated state underlying the DC response. An important observation, therefore, is the association of the AC response at steady conditions to the strong AC ringing response due to the relatively abrupt switching event. The shift originates from quantum interference effects as described below. Hence, we focus now on the electronic structure features affecting the DC and AC components.

In order to analyze the origin of this energy shift we consider the electronic structure of conducting channels models involving two sites as used in the TD current calculations. In Figure 7.5 (Left side) the electronic-energy density-of-states (DOS) with three different base values for the broadening (imaginary smear factor parameter) of the bulk GF (see eq. 5.34). Changing the bulk broadening factor (η_b) allows us to selectively broaden only the open channels. Bound states, which will be explored following the two conducting channels analysis, remain properly unbroadened by this factor. The corresponding TD conductance plots are provided at the right side of the figure. As expected, increasing the broadening results with a larger conductivity at steady state. The I(t) curves also demonstrate the dissipation effects due to the broadening on the conductance oscillatory features. The TD oscillations are shown to dissipate quicker with increasing the broadening. Clearly, upon sufficient broadening of the participating bands in the interference, where, for example, the two channels become one effective band, the oscillatory component of the conduction

Figure 7.5: The two site system with three different broadening (base) factors. (**Left**) The electronic DOS. (**Right**) The associated I(t) curves.

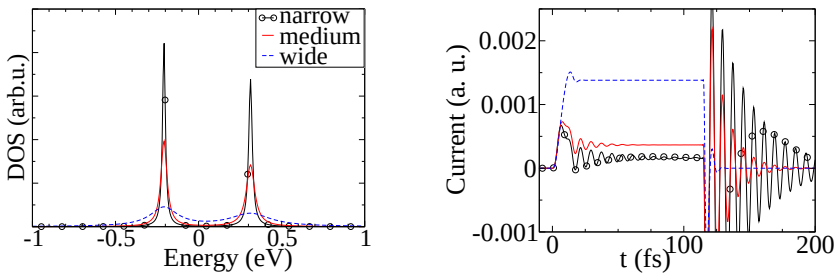

is almost completely dissipated. We focus next on the energy shift related to the value at which the oscillatory response is observed in the Wigner plots.

The current distributions associate the oscillatory response of the current to interference fringes. The interferences are observed at energy shifts from the open channel energies determined by the superposition of the two interfering states. This can be understood by simplifying the general propagation expression provided in equation 6.8 assuming that the lesser GF has a peak at bulk affected states ϵ_o ($\mathbf{G}^<(\bar{\omega}) \sim \mathbf{G}^<_{\epsilon_o}\delta(\bar{\omega}-\epsilon_o)$). We also use eqn. 6.3 to grossly approximate $G^<(\bar{t},\bar{\omega})$ by

$$ie^{-i(\epsilon_i-\epsilon_j)\bar{t}}\int_{t_0}^{\bar{t}} d\bar{t}' e^{i(\epsilon_i-\epsilon_j+2\epsilon_o-2\bar{\omega})\bar{t}'}\,\tilde{\mathbf{v}}\left(2(\bar{\omega}-\epsilon_o)\right)\mathbf{G}^<_{\epsilon_o}. \tag{7.8}$$

In the last expression, ϵ_i, ϵ_j and ϵ_o represent bulk affected states (open channels). Interference fringes are, therefore, shifted by $(\epsilon_i-\epsilon_j)/2$ from ϵ_o on the $\bar{\omega}$ axis. Furthermore, they will oscillate in time $\bar{t}$ with frequency $(\epsilon_i-\epsilon_j)$. The interferences that will actually affect the current depend on the unperturbed device's electronic structure and the details of the applied perturbation.

We now turn to focus on systems with bound states added to the open channels. These states do not mix with the bulk electronic structure bands. The bound states *do not* contribute conducting (open) channels coupling the two bulks as they do not

mix with the bulk band structure. It is interesting to note recent reports, where bound states are shown to enhance the transient ringing response due to an applied potential pulse.[39, 109] We show that bound states can lead to an oscillating response only under certain conditions. These conditions introduce a symmetry breaking effect where the coherence driven contribution due to the two interfering bound states involves a relative phase shift between the two states. A simple example for introducing such a shift is provided next.

We consider two systems, where one system includes a symmetric population of the two bound states and the second has only one of the two located below the designated Fermi energy, namely their population is very different. The bound states are clearly apparent in the electronic DOS, which are plotted in Figure 7.6 **(a)**. The resulting I(t) plots responding to the (relatively) adiabatic potential pulse are provided in Figure 7.6 **(b)**. It is shown that persisting oscillations of the current are obtained only for the case with the asymmetry introduced in the population. The current (I(t)) for the other case with both bound states populated is, however, not different from the case which has no bound states added. We next analyze the band structure of the current operator for these systems with the added bound states.

In parts **(c)** and **(d)** we provide the Wigner plots of the cases with the symmetric population and the antisymmetric case, respectively. For both the DC band at about -0.25eV due to the lower state open channel is observed. The dissipative interference between the two open channels is observed at 0eV. We then note the contribution due to the populated bound states that is overall vanishing at the switching times. In part **(c)** their interference at -1.0eV also results in a complete cancellation of the integrated result leading to the current due to the symmetry of the two bound states. Only a symmetry breaking gating field will lead to a non vanishing contribution to

Figure 7.6: The two site system including 2 additional bound states. The interference involving the bound state results with a persistent current oscillation: **(a)** The electronic density of states. **(b)** The I(t) curve. Wigner plot of the current distribution: **(c)** with two stable bound states **(d)** with one stable bound state and one unoccupied.

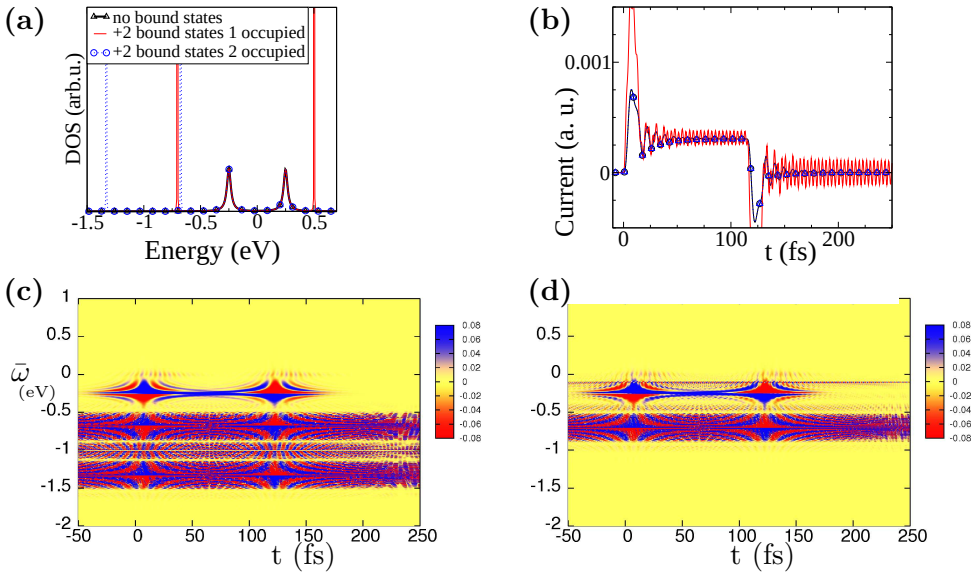

the current for this interference. This is shown in part **(d)** where the interference of the two bound states occurs at about -0.1eV and leads to the persisting oscillation of the current. We describe further in detail the conditions for the bound state presences to lead to oscillation elsewhere.

We now consider the effect of the relative scales of the electronic parameters within the model Hamiltonian on the transient effects of the conductance. The electronic coupling values are related to distances between neighboring sites or relative electronic charge capacities between these sites. All cases considered here involve the relatively adiabatic bias switching rate (over 15 fs) and a non-adiabatic turn off event (1 fs). Figure 7.7 provides the density of states for the different cases of the electronic mixing parameter. We note the bigger splitting around the FE and broadening upon the increase of the mixing parameter. The Figure also provides TD conductance curves (left) and their corresponding Wigner distributions for the three

cases with different electron coupling (β_d) values as specified. The developing DC (steady state) is shown to increase with increasing absolute values of the electronic mixing parameter. This is also associated with a decrease in AC amplitude, where the strongest transient response for the system is observed with the weakest mixing parameter.

We also note that varying the electronic coupling parameters leads to either delocalization or localization of $\bar{t}$ and $\bar{\omega}$ variables in the Wigner current distributions. The Wigner plots show that for the same perturbation the rate of the switch-on becomes essentially adiabatic for a large enough electronic coupling value. In addition, a decrease in the electronic coupling parameters leads to localization of the relevant energy range involved in the current-distribution response. Therefore, increasing $|\beta|$ leads to $\bar{t}$-localization and $\bar{\omega}$-delocalization of the current response to the switching. This is the expected dependence on the parameters that control the energy coupling strength between neighboring sites.

As a final aspect of TD conductance, we consider now a two states system with a driving TD perturbation. The DOS and the related conductance response to a driving AC potential with its frequency tuned exactly to the energy levels difference is illustrated in Figure 7.8. We now compare to the current upon applying a symmetry breaking DC potential bias and treat this as the unperturbed system. The corresponding DOS is shown to result with a slight energy splitting of the two bands. This also leads to reduce the current, where, however, the broadening ensures that most of the current is not eliminated. More interestingly, a beating frequency is also noted. These two effects are a consequence of the bands being further split which effectively detunes the focused laser field.

The coherence mediated conductance is also analyzed by the current distributions.

Figure 7.7: The effect of the strength of electronic coupling (β_d)on TD conductance: **(a)** The electronic density of states. **(b)** The I(t) curve. **(c)** Wigner plots of the current distribution for the system including the two additional bound states with different scaling color scheme.

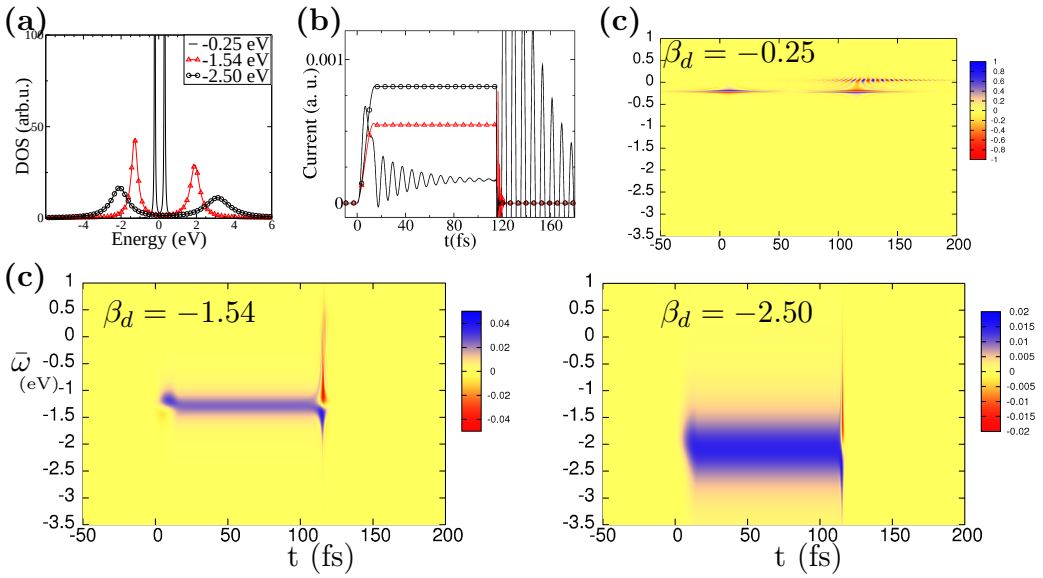

Two cases are considered. In the upper panel of Figure 7.8 the current distributions of the case with only one open channel being occupied are provided. We note that the major contribution to conductance is from the direct interference of the two states as expected. This is what the applied laser is tuned to. An additional current distribution band is located at the opposite shift from the electronic device state. The shift is defined by the energy average of the two open channels. We note that the opposite shifts (each away from the other state) are shown to contribute substantially to the current. A contribution below the ground state is observed only for the system involving a single site occupation. In the lower panel, the case with both open channels being populated is considered. For this system an additional band located at the same shift *above* the higher energy open channel band is introduced. We also note that applying the same AC on the DC-biased system results with a different shift on the two types of the bands. In this case, the structure of the major shift due

Figure 7.8: Coherence driven current of a two state system with and without a steady DC bias. (Left) The DOS and the I-t of the two state system. Current distribution of: (Up) tuned system (Low) DC detuned and (Center) One state occupied and the (Right) Two states occupied

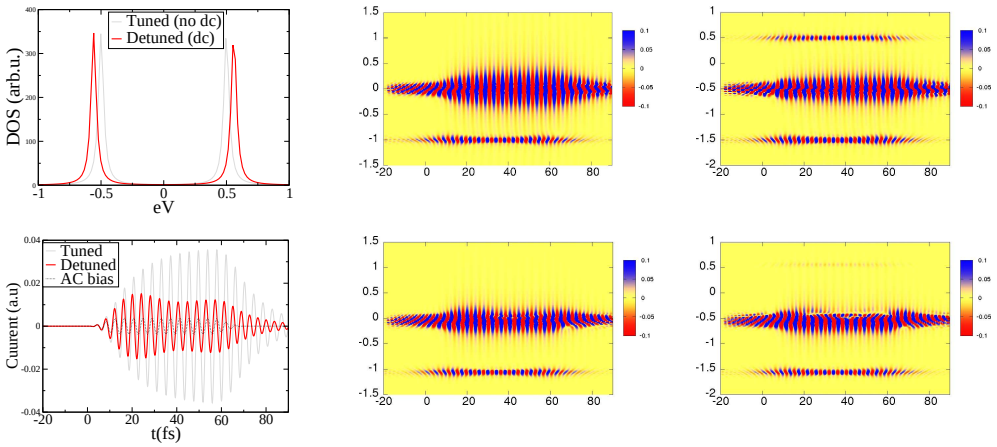

to the $\bar{\omega}$ dependence is distorted. This energy dependent shift is responsible to the beating that is observed in the calculated I-t curves.

7.2 Flux Induced Spectroscopy in explicit tight-binding models

Introduction

In this section we study the effects of non-equilibrium conditions on the electronic spectra of a model open channel system. We use the formalism derived above in the full frequency domain and solve it at the linear response level. The full frequency expressions of the e.o.m.s are used to eliminate the WBL approximation in treating the electronic structure of the bulk.[99] Instead the electrodes are treated exactly at the applied modeling level. Therefore, an energy dependent DOS of the electrode evaluated by the relevant tight binding treatment is used. This is a powerful scheme to calculate the electronic spectra of an open system at non-equilibrium conditions. We use our methodology to demonstrate that the effect of flux due to bias conditions is to allow electronic transitions that are otherwise forbidden in the equilibrated

system.

A large body of related experimental studies have been performed. The combined measurement of both conductance and spectra of molecular junctions has been reported using Raman scattering [91, 90, 17, 127]. Conductance enhancement in the junction has been correlated with changes of the *in situ* measured Raman spectra of the molecular junction. This is an exciting development that contributes to the characterization of molecular junctions under bias. The ability to obtain spectral information of the junction system under bias provides the needed probe to confirm that single molecules are indeed confined between the electrodes and carry the transport in the junction. It is, therefore, important to proceed and consider the effects of electronic flux due to the bias on the electronic spectra of the molecular junction that is mediating the electron transport.

In order to understand the dynamical effect of electron flux on the spectra or of any other photo driven ET process proper treatment of the electronic structure of the open systems has to be achieved. For achieving analysis of the flux-affected electronic spectra, a TD approach that probes the response of the electronic density to a temporal delta function potential pulse can be used to generate the system's spectra as is performed in traditional widely-used linear response implementations of TD-DFT. This is extended below to the analysis of electron flow effects on the optical excitations of a biased model system.

7.2.1 Models

The model system considered in this study is composed of a pair of sites aligned perpendicular to the direction of flow coupling two one-dimensional wires. The graphical representation of this model system is provided in Figure 7.10, where only the surface atom of the wire is depicted. The two central sites and the surface sites define

Figure 7.9: Scheme of the electronic levels of a device model system coupled to the electron reservoir at **(left) equilibrium (right) non-equilibrium** conditions.

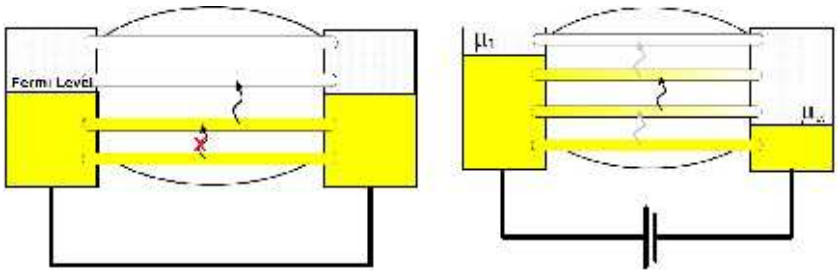

Figure 7.10: Illustration of the model composed of two sites bridging two one-dimensional semi-infinite wires. Only the surface atom of each wire is depicted.

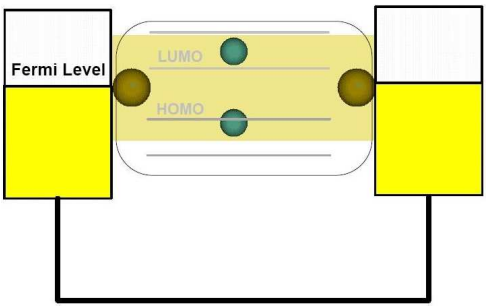

the core region of the system. We use a simple tight binding model for the electronic structure, where each site is represented by a single s type basis function. Relative to the center of a given atom A, this basis function is expressed in spherical coordinates as $\Phi(r_A, \theta_A, \phi_A) \sim e^{-\alpha r_A^2}$. The "tightness" parameter, α, is determined by setting $\langle r_A \rangle$ to the electronic radius of the given atom. The sites of the electrode have been parametrized to represent gold atoms and the device sites are each representing a single carbon atom. The corresponding region is designated below as AuC_2Au

The atomic orbital Hamiltonian matrix is parametrized based on the ionization potential and evaluated using the following Huckel-type expressions:

$$H_{A,A} = -I_A \tag{7.9}$$

$$H_{A,B} = -\frac{1}{2}K(I_A + I_B)S_{A,B} \tag{7.10}$$

where $S_{A,B}$ is the atomic orbital overlap between the s-electron basis functions centered on atoms A and B, I_A is the ionization potential for atom A, and K is a constant set to 1.75. The numerical values for these parameters are provided in Table 7.2.1. The Hamiltonian is then orthogonalized ($\mathbf{H} \rightarrow \mathbf{S}^{-1/2}\mathbf{H}\mathbf{S}^{-1/2}$) followed by the imposition of a tight-binding condition within the electrode regions, where only site and nearest-neighbor hopping elements are non-zero. All site and hopping elements are kept in the four-site region of the orthogonalized Hamiltonian that corresponds to the AuC_2Au region of the pre-orthogonalized Hamiltonian. This Hamiltonian is padded with electrode wires of nine Au atoms on each side of the perpendicular C_2 system to ensure that edge effects are minimized in the orthogonalization procedure.

We now calculate the electronic density and spectrum of this system, where we include the surface atoms in the confined device region. This defines the core device region as a four state space. The electrodes' effects on the electronic DOS of the

Atom	*radius Å*	I_A *(eV)*	α *(Å^{-2})*
C	0.77	11.26	1.074
Au	1.44	9.22	0.307

Table 7.1: Radii, ionization potentials, I_A, and Gaussian basis set coefficients, α, for C and Au

junction are represented as usual by adding to the Hamiltonian the projection of the surface GF onto the central region using the TB coupling terms. Next, we consider the system prior to probing its spectroscopy. In all cases, we note that for simplicity the Fermi energy is shifted to be zero and is located in the middle of the HOMO-LUMO gap. This is schematically illustrated in Figure 7.9(left). The steady state description is derived from a time independent perturbation perspective, where any bias has been turned on for a sufficiently long time to dissipate any transient or TD aspects. Eqn. 6.33 is used as an initial guess for the steady state lesser Green function that introduces the effects of weak bias $\mathbf{v}_\circ$.

If $\mathbf{v}_\circ$ is energetically on the order of the transition energies in the Hamiltonian, a first order expansion will not suffice. In this case we turn on the bias adiabatically (compared to the time evolution of the Hamiltonian) in n small increments. This amounts to applying eqn. 6.33 iteratively n times as described in a previous section.

7.2.2 Results

The electronic spectrum is obtained by tracing the dipole moment operator oriented along the device (C_2) axis (designated as z). This is aligned perpendicular to the gold wires axis:

$$Im\left[\langle\mu_z(\Delta\omega)\rangle\right] = \int d\bar{\omega} Tr\left[G^<(\bar{\omega},\Delta\omega)\cdot\hat{\mu}_z\right], \tag{7.11}$$

where the dipole operator matrix representation ($\{\Phi\}$ are the basis functions) is:

$$\mu_{z,ij} = \int d^3\vec{r}\Phi_i(\vec{r})\hat{z}\Phi_j(\vec{r}). \tag{7.12}$$

Figure 7.11: **(a)** The electronic density of states of the device region at **equilibrium** conditions with models including 1,2 and 3 wire sites in the central region. **(b)** The corresponding electronic spectra with the different inclusion of gold atoms in the central region (The spectra are given in atomic units as Bohr radius/Hartree).

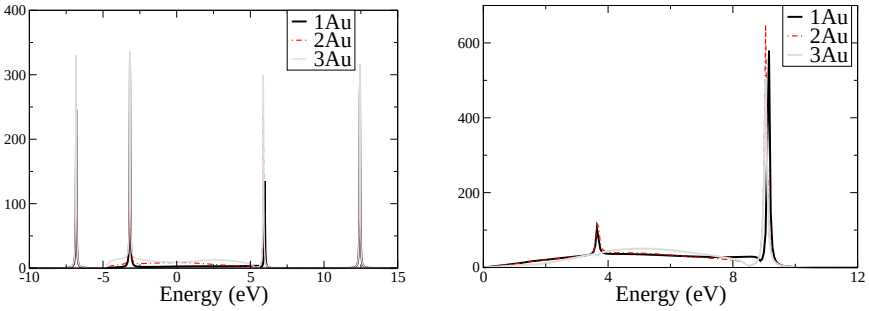

(a) Electronic DOS **(b) Electronic spectra**

The projected electronic DOS of the device region is calculated for several related models. These models differ in the number of the wire gold atoms included in the device region. Following the tight-binding picture the most distant atom included in the device region from the core pair of atoms is assumed to well represent the surface site of the wire. The electronic DOS and the corresponding spectra are provided in Figure 7.11.

We note that the DOS of the device region, which is shown on the right panel, converges with respect to the number of gold atoms included in the central region. Namely, adding gold atoms to the device region does not greatly affect the four major peaks in the distribution. These additional wire atoms mainly affect the DOS by further broadening the electronic density within the HOMO-LUMO gap. This is a reflection of the strongly delocalized nature of the electrode model used in our calculations. The effects of these broadening aspects on the modeled spectra are considered next.

Orbitals related to the main four bands of the core region are illustrated in Figure

Figure 7.12: Orbitals are plotted organized according to their energy levels from left to right in an increasing order. Left most panel illustrates the molecular model of the core system used in the calculations.

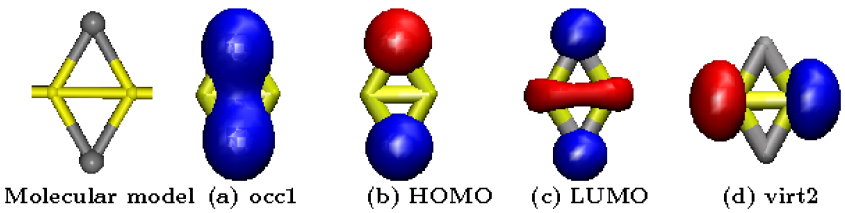

7.12. The core region includes the two carbon atoms and a gold atom from each wire which is most adjacent to the carbons. We have shifted the energies to be centered about the Fermi energy which has been chosen to be zero for simplicity. In the chosen geometry, we assign the lowest state (occ1) to a bonding interaction between the carbon atoms. The second state, which is also occupied (occ2 or HOMO) corresponds to an antibonding interaction between the carbon atoms. The next state, is unoccupied (virt1 or LUMO), which at the considered equilibrium conditions involves antibonding interactions between the two carbon atoms and with additional bonding interaction between the two gold surface atoms across the device region. Finally the highest state (virt2) is dominated by electron density localized on the gold atoms with an anti-bonding node separating the two sites.

The corresponding electronic spectra show a strong dependence on the model used. The models differ by the number of gold atoms included in the device region. First, we assign the dominant peak in all non biased spectra to the HOMO-LUMO transition. However, an unconverged response (peak) is generated for the limited model, where only a single gold atom is included in the junction's space. For this smaller model, a peak corresponding to the energy difference between states occ1 and occ2 is generated. These electronic states, however, which lie energetically below the Fermi energy, are both populated upon coupling to the two wires.

Clearly electronic transitions that couple two occupied states are forbidden at equilibrium conditions. This indicated forbidden transition is (almost completely) removed upon including additional wire sites in the device at equilibrium. It is shown that this peak in the spectra is gradually eliminated at the equilibrium conditions by expanding the central region to include one or two additional gold atoms from each wire. We also note that the differences in the broad bands between the different models result from the projection of the infinite electrodes onto the device region. This also leads to the broadening observed on the electronic spectra (see figure 7.11).

The appearance of the additional and unphysical transition at an equilibrium state is a reflection of using a too restrictive model in the response theory. This difficulty in converging the calculated spectra is due to the delocalized nature of the electronic states that participate in the considered transition. These states have a large gold atom component in their electronic DOS. The delocalized nature of the metal related electronic density is represented by self energies and is associated with the broadening effects. For example, the strong delocalization of the HOMO results with an artifact as noted above due to the self energy used in the spectra calculation. We, therefore, use the model that includes three gold atom sites in analyzing the spectra under bias conditions to allow for proper treatment of the electrodes' effects on the electronic density of the confined system. Next, we analyze the spectra at non zero bias-voltage conditions.

In Figure 7.9(right) the effect of the potential bias is schematically represented. The bias is shifting the effective Fermi energies of the two electrodes. In the illustration the resulting energy window of non-equilibrium occupations between the two electrodes is large enough to include both bands of the HOMO and LUMO electronic states. In Figure 7.13 the voltage dependent spectra are provided. It is shown that

Figure 7.13: The dependence of the electronic spectra on the voltage. (The spectra are given in atomic units as Bohr radius/Hartree).

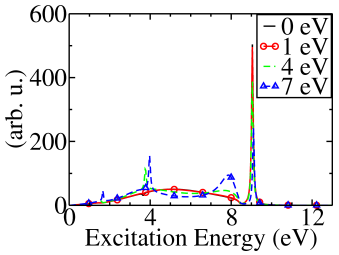

for strong enough bias voltages the otherwise forbidden transition becomes allowed. This is a flux induced transition. This is shown in the figure, where the peak corresponding to the transition between the two lowest states only starts to develop for strong enough applied voltages. It becomes a dominant peak in the spectra, when the non-equilibrium conditions are further enhanced by even higher applied potential biases.

We observe the opposite trend on the higher peak in the spectra. This peak corresponds to the transition of states occ2 to virt1 (HOMO-LUMO in the equilibrium state). It becomes weaker as the two states experience stronger non-equilibrium conditions, where both bands are populated by the dynamic electron flux flowing through them. This is another important consequence of the spectra due to the non-equilibrium conditions that is nicely demonstrated by the implemented calculations.

7.3 Population Inversion and Absolute Negative Conductance

In a classical system, such as a metallic wire, the application of a source drain bias or field forces electronic charge to move in the direction of applied force producing a forward current. In a two conducting channel quantum system the same result is achieved by moving charge through the lower conducting channel (section 7.1). In essence, the states within this conducting channel that carry a forward momentum

will have acquire a higher coefficient than those with momentum in the reverse direction. However, as is demonstrated through analytical derivation and simulation, the virtual conducting channel can have the opposite effect. When populated, this channel will produce a current in the direction opposite to that of the applied field. Thus, at infinite temperature, when both conducting channels are equally populated, the total current will be zero, as expected. However, if population inversion is achieved, the virtual conducting channel will have more population than the occupied channel and the net current produced will be in the direction reverse to the applied field.

To demonstrate this, eqn. 6.33, which represents the steady state linear response of the system to a weak bias is integrated with respect to $\bar{\omega}$, making use of the relation for total density.

$$\rho = -i \int d\bar{\omega} \mathbf{G}^{<}(\bar{\omega}) \tag{7.13}$$

This gives a steady state linear response equation for the total ($\bar{\omega}$-integrated) density.

$$\begin{aligned} |\rho_{v_\circ,CC}\rangle\rangle \rightarrow \\ |\rho_{\circ,CC}\rangle\rangle + \mathbf{G}(0)|B^{(1)}_{\rho,CC}\rangle\rangle \end{aligned} \tag{7.14}$$

where,

$$|B^{(1)}_{\rho,CC}\rangle\rangle_{ni+j} \equiv [\mathbf{v}_\circ \rho_{\circ,CC} - \rho_{\circ,CC}\mathbf{v}_\circ]_{ij} \tag{7.15}$$

and $\rho_{v_\circ}$ is the total density including the response to the source-drain bias while $\rho_\circ$ is the statistically equilibrated total density in the absence of any bias perturbations. Equation 7.14 is applied to a two-site system in the atomic orbital representation (where the overlap is diagonal), with Hamiltonian $\mathbf{h}$ and perturbation operator $\mathbf{v}$,

$$\mathbf{h} = \begin{bmatrix} -i\Sigma & \beta \\ \beta & -i\Sigma \end{bmatrix}. \tag{7.16}$$

$$\mathbf{v} = \frac{\mathbf{1}}{\mathbf{2}} \begin{bmatrix} v & 0 \\ 0 & -v \end{bmatrix}. \tag{7.17}$$

where $-i\Sigma$ represents the wide-band-limit self-energy that models the electrodes and effectively turns the two states into conducting channels. The current operator has the form,

$$\mathbf{j} = \mathbf{i} \begin{bmatrix} 0 & \beta \\ -\beta & 0 \end{bmatrix}. \tag{7.18}$$

In the representation where $\mathbf{h}$ is diagonalized, these operators take the following forms,

$$\mathbf{h} = \begin{bmatrix} \beta - i\Sigma & 0 \\ 0 & -\beta - i\Sigma \end{bmatrix}. \tag{7.19}$$

$$\mathbf{v} = \frac{\mathbf{1}}{\mathbf{2}} \begin{bmatrix} 0 & v \\ v & 0 \end{bmatrix}. \tag{7.20}$$

$$\mathbf{j} = \mathbf{i} \begin{bmatrix} 0 & -\beta \\ \beta & 0 \end{bmatrix}. \tag{7.21}$$

where β is the ground state energy and $-\beta$ is the excited state energy ($\beta > 0$). Note that rotation of the current operator into the diagonalized basis only changes its sign. The initial density matrix $\rho_\circ$ has the form,

$$\rho_\circ = \begin{bmatrix} 1 & 0 \\ 0 & 0 \end{bmatrix}. \tag{7.22}$$

when the electron population is completely in the ground conducting channel and

$$\rho_\circ = \begin{bmatrix} 0 & 0 \\ 0 & 1 \end{bmatrix}. \tag{7.23}$$

when the population is entirely in the excited conducting channel (population inversion). The total current I is calculated by tracing $\rho_{v_\circ}$ with $\mathbf{j}$. Substituting eqns. 7.19-7.20 into eqn. 7.14 for the ground state populated case (eqn. 7.22) gives a total density of

$$\rho_{v_\circ} = \begin{bmatrix} 1 & -\frac{v}{4(\beta+i\Sigma)} \\ -\frac{v}{4(\beta-i\Sigma)} & 0 \end{bmatrix}. \tag{7.24}$$

and a positive total current.

$$I(v) = \frac{1}{2}\frac{\beta\Sigma}{\beta^2+\Sigma^2}v \tag{7.25}$$

On the other hand, performing this substitution for a population inverted initial density matrix eqn. 7.23 produces a total density matrix of the form

$$\rho_{v_\circ} = \begin{bmatrix} 0 & \frac{v}{4(\beta+i\Sigma)} \\ \frac{v}{4(\beta-i\Sigma)} & 1 \end{bmatrix}. \tag{7.26}$$

and a total current

$$I(v) = -\frac{1}{2}\frac{\beta\Sigma}{\beta^2+\Sigma^2}v \tag{7.27}$$

that is opposite to direction of flow. Interestingly, the source of this reverse current is population inversion – the cause of light amplification in lasers and optical amplifiers. Note that a negative sign in the transition elements in eqn. 7.22 corresponds to an excitation, while the positive sign in eqn. 7.26 carries a relaxation back to the ground state.

Absolute Negative Conductance in a Three State System

Population inversion is not an easy phenomenon to achieve. In a two state system, one can, at best, achieve a steady state balance in which both states have an equal occupation number. Transient population inversion is achieved in such systems via

Figure 7.14: Schematic diagram of 3-state system in the localized *site* representation (left) and the diagonalized representation (right). The strong coupling of the conducting sites/channels are represented by their "smearing" and emersion in the electrodes. The ground state ϵ is weakly coupled to the conducting channels (represented by dotted lines). The left (right) electrode is biased at $+(-)v/2$ around the unbiased fermi energy ϵ_f.

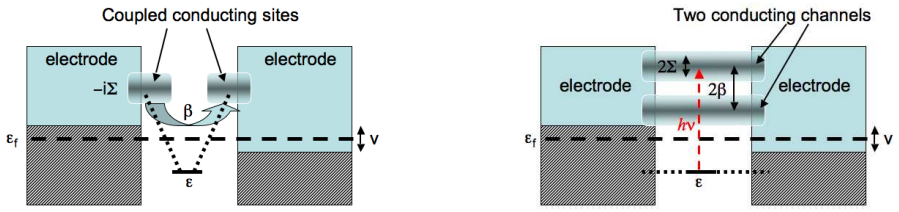

Rabi flopping which typically requires very intense ac fields. However, a steady state population inversion can be achieved in a three level system – the basis for light amplification in a laser. We now demonstrate that a three level structure can lead to absolute negative conductance. Similar to a laser, our system consists of a weakly conducting populated ground state and two unoccupied strongly conducting excited states (conducting channels). The system is biased by a dc ramping field. Population is subsequently excited from the ground state to the second excited state (fig. 7.14, right panel), creating a population inversion between the first and secnd excited states. Under bias, this configuration will transfer net charge in the direction opposing the bias field (absolute negative conductance).

We consider a three level system (fig. 7.14) that can be constructed by strongly coupling two "sites" (e.g. quantum dots) to electrodes and to each other. The ground state can then be introduced by a third site that is weakly coupled to the two conducting sites (denoted by dotted lines in fig. 7.14) but has a comparably low on-site energy ϵ. This low lying site is below the fermi energy of the electrodes, ϵ_f, and is therefore occupied. The two upper levels are both unoccupied and strongly coupled to each other by hopping energy β and to the electrodes via a self energy Σ. The

Figure 7.15: (Left) Density of states ($\epsilon_f = 0$). (Right) Current vs. time for an applied bias of 0.01 meV and a 240 ps applied AC field at $\nu = 0.246$ meV.

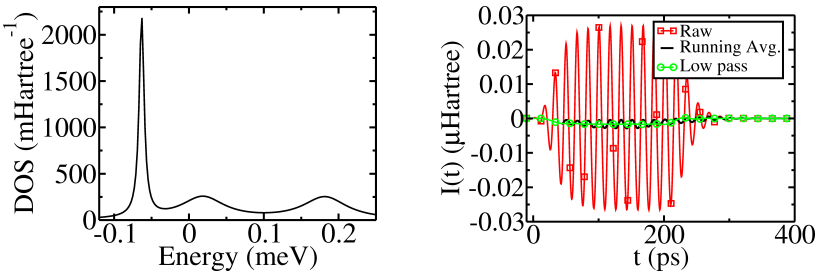

ground state is thus spatialy summetric (bonding) while the first and second excited conducting channels are, by construction, bonding and anti-bonding, respectively. A wide band approximation is applied to the electrodes giving them a uniform density of states and, thus, making Σ independent of state energy. These couplings produce two broadened conducting channels (smeared in fig. 7.14) whose energy centers are seperated by 2β and whose bandwidths are given by 2Σ. The ground state coupling to the conducing sites is 100 times smaller than β. Hence, it is also subjected to a small broadening. In addition, a device broadening of 0.004 meV is uniformly applied to all three states. This has the effect of broadening the ground state to allow more rapid simulation convergence. However, this broadening factor is an order of magnitude smaller than Σ ensuring that it will contribute negligible conductance. This density of states for this system is given by the left panel in fig. 7.15. Note that, by design, the ground state is weakly conducting due to its much smaller broadening when compared with the two conducting channels. Most of the current must be carried by the unoccupied conducting channels or absolute negative conductance will be difficult to achieve. The resulting mid-band energies and bandwidths are listed in table 7.3.

A constant ramping potential (v in fig. 7.15) is applied to the system to facilitate the transfer of charge (current) from one electrode to the other when the ac field is

state	*energy* (meV)	*FWHM* (meV)
g	-0.0637	0.01
1x	0.0183	0.07
2x	0.182	0.07

Table 7.2: Mid band energies and bandwidths for the ground, first and second excited states, labeled "g", "1x" and "2x" respectively.

transition	μ *(arb. u.)*
g-1x	0.0
g-2x	1.4
1x-2x	50.

Table 7.3: Transition dipole strengths for excitations between the ground (g), first excited (1x) and second excited (2x) states.

applied. The simulations were run for $v = 0.01meV$ and $v = 0.04meV$. These biases are weak compared with the transition energies of the states so spectroscopic Stark shifts are negligible. Consequently, an ac field tuned to the excitation frequency between the ground and second excited states ($\nu = \omega_0/(2\pi) = 0.246meV$) is applied to systems under both biases. Table 7.3 gives the transition dipole strengths between the three states. Note that the ground to first excited state transition is forbidden because the states possess the same symmetry. The ground to second excited state transition, which is of interest to us, is very weak when compared with the first to second excited state transition. This is a consequence of the weak coupling between the ground state and the two unoccupied conducting channels. Most of the ground state's charge density is localized to the central site in fig. 7.14. The conducting channels, on the other hand, have most of their charge divided between the left and right sites. Hence, the overlap between the ground state and the conducting channels is very small. This weak coupling is necessary to ensure that the conducting channels do not strongly broaden the ground state, making it strongly conducting as well. The strength of the applied ac field must be carefully chosen because the method used for

these simulations as described in chapter VI employs a time dependent perturbation expansion. Like time independent perturbation theory, the strength of the perturbation must be much smaller than the transition energies in the system. However, time dependent perturbation theory has an additional constraint for resonant excitations. Namely, even for weak perturbations that fit this energy criterion, the perturbative result will diverge from the exact result if the perturbation endures for long enough times. To demonstrate this, one can examine the simple case of Rabi flopping between two discrete states since such a system is analytically understood and readily provides a measure of the deviation of perturbation theory from the exact result.

An oscillatory perturbation applied at $t = 0$ to a two state system with excitation energy ν has the form,

$$\mathbf{v}(t) = \begin{bmatrix} 0 & v_0 \sin(\omega_0 t) \\ v_0 \sin(\omega_0 t) & 0 \end{bmatrix}. \tag{7.28}$$

This oscillatory field will create a coherence between the ground and excited states and cause their respective occupation numbers to oscillate at the Rabi frequency, v_0. If one considers, for example the ground state population in time, $P_0(t)$,

$$P_0(t) = \cos^2\left(\frac{v_0 t}{2}\right) \tag{7.29}$$

one can expand this solution to second order in v_0,

$$P_0(t) = 1 - \frac{1}{4}(v_0 t)^2 + ... \tag{7.30}$$

The perturbative result will diverge and produce negative populations for $t > 2/v_0$. Consequently, there is a time limit, inversely proportional to the Rabi frequency, by which the the perturbation must be shut off. Extending the driving field beyond this limit can lead to inaccurate and unphysical results in perturbation theory.

Figure 7.16: Energy resolved total occupation distribution (left) and integral of distribution over the ground conducting channel - −0.15 meV to 0.00 meV (right).

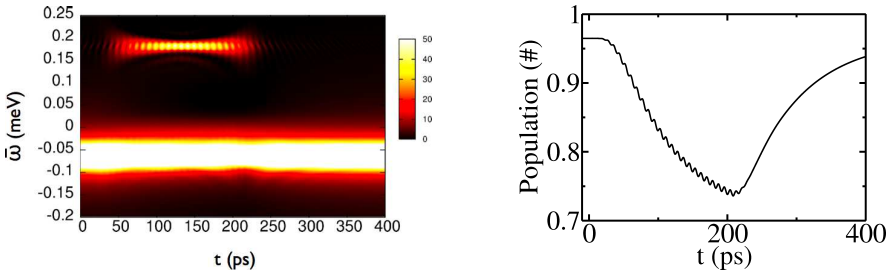

The Rabi flopping argument clearly demonstrates this limitation of time dependent perturbation theory and thus, care must be taken to ensure that perturbatively calculated population changes between conducting channels do not exceed a given threshold. Consequently, we employ the rule of thumb is that one should not let the perturbation theory calculated population loss exceed approximately one third of the total population in the donating band. From the discrete state model, we note that the perturbative result and the actual result differ by about 11 percent for a population loss of 1/3 from the ground state. We apply an ac perturbation that is smoothly turned up to 0.014 meV over 40 ps, subsequently maintained at this energy for 160 ps and, finally, turned of smoothly over another 40 ps. The total duration of the pulse is thus 240 ps. These conditions ensure that the maximum population loss is slightly in excess of a quarter (fig. 7.16 right).

The resulting current as a function of time is shown on the right side of figure 7.15 for the case of an applied bias $v = 0.01$ meV. The current is highly oscillatory because it includes the resonant oscillations in charge induced by the ac field. Furthermore, it looks symmetric about zero. A running average of the current over several cycles (fig. 7.17, left), however, shows an overall negative current and, thus, demonstrates absolute negative conductance. A low pass filter applied to the current, in which all components with absolute frequency above 0.13 meV are zeroed, agrees well with the

Figure 7.17: Time dependent (left) and spectral (right) first and second order contributions to the current at an applied bias of 0.01 meV and a 240 ps applied AC field at $\nu = 0.246$ meV.

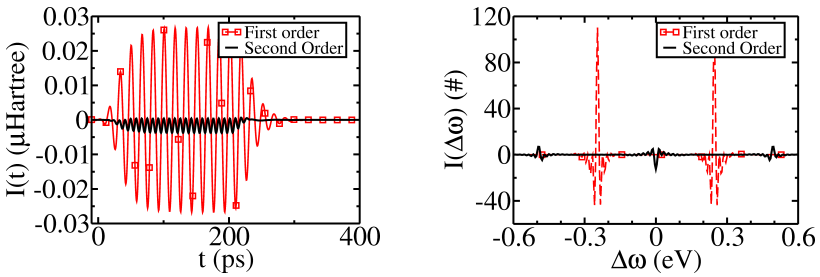

running average. Figure 7.17 shows that the absolute negative conductance comes from the contribution to the current that is second order in the perturbing field. The right panel is the Fourier transform of the data in the left panel and shows oscillatory responses at first order at $\pm\nu$ and at second order at $\pm 2\nu$ as expected. The second order contribution shows a negative component around zero frequency, a clear signature of the negative DC current. This also indicates that the current comes from population transfer because a second order response to the ac field is required to induce a population transfer between states.

Finally, we show evidence that population inversion between the first and second excited states is achieved, and, that the population in the second excited (anti-bonding) conducting channel is responsible for the reversed current flow. The left panel in figure 7.16 indicates that population is transfered to the second excited state by the ac pulse. This, together with the right panel in fig. 7.16, which indicates the population loss from the ground state suggests that the ac pulse has transfered this population, as expected. The right panel in figure 7.18, which is the second order contribution to the energy resolved time dependent occupation number, also shows a population transfer from the ground state, at energy -0.0637 meV to the second excited state at 0.182 meV. Both of these graphs indicate no increase in

Figure 7.18: Energy resolved current distribution (left) and energy resolved second order contribution to the occupation distribution (right) for an applied bias of 0.01 meV and a 240 ps applied AC field at $\nu = 0.246$ meV.

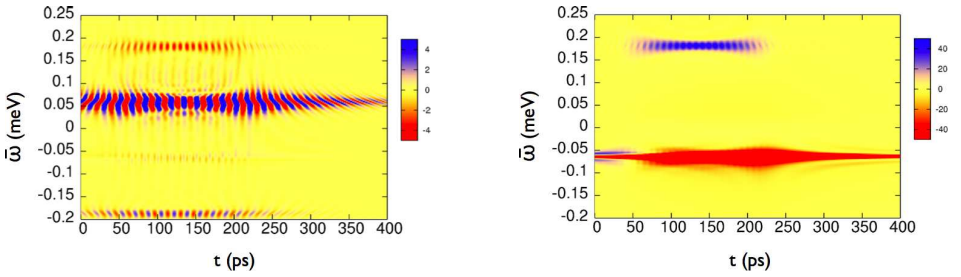

population at the first excited state (0.0183 meV). Thus a population inversion is achieved. The left panel in figure 7.18 is the energy resolved current distribution for this system. It indicates two major features. The more intense feature is the positive-negative oscillating interference fringe located exactly in between the ground and second excited states with oscillation frequency equal to the transition energy between these two states. This is the resonant first order response of the current to the ac field. The second feature, located at the second excited state energy, is completely negative, with superposed oscillations at twice the resonant frequency. This is indicative of the second order contribution to the current (fig. 7.17). This is a clear indicator that the population transfered from the ground state to the second excited state responds to the applied bias by moving in the direction opposite to the applied bias. Figure 7.19 compares the low pass filtered data for the same applied ac field at different applied biases. The negative current increases with increased applied bias. The energy needed to work against the applied bias is provided by the ac field. For comparison, we also perform runs where the fermi energy is raised to be between the first and second excited states. The first excited state is thus occupied while the second excited state is vacant. Biases equivalent to those of figure 7.19 are applied, but, no ac field is applied. The currents are listed in table 7.3. The currents

Figure 7.19: Low pass filtered current as a function of time for applied biases of 0.01 meV and 0.04 meV and a 240 ps applied AC field at $\nu = 0.246$ meV.

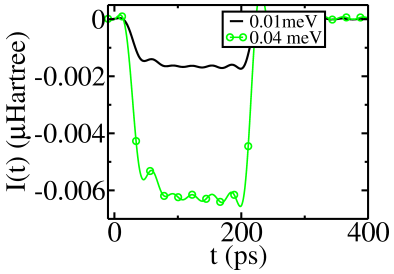

bias (meV)	*current* (μH)
0.0100	0.0595
0.0400	0.227

Table 7.4: Currents at given bias voltages for an un-pumped system with initial fermi energy located between first and second excited states.

respond positively to the these biases and are much larger than the negative currents achieved above.

CHAPTER VIII

Future Work: Disagreements in DC Current Methodologies

Constant potential theory, as developed in section 6.2.3 is an approach that can be applied to the calculation of steady state transport properties. As such, its predictions of transport properties should agree well, in the ballistic limit, with Landauer theory, which will be summarized in section 8.1.1. However, we find that this is not the case. One drawback of CPT is that, thus far, it has not included the applied bias in the electrodes. In this chapter, an approximate CPT that includes these effects for electrodes approximated by the wide band limit is derived. Preliminary results on a two conducting channel system indicate that such an approach produces conductances that are identical to those given by Landauer theory in the ballistic limit. Preliminary Landauer calculations are also performed on a six carbon chain connected to gold wire electrodes in preparation for benchmarking this extended CPT with Landauer on a more realistic system. The Hamiltonian for the system is calculated by density functional theory (DFT). This approach therefore provides a path for resolving the Landauer-CPT discrepancy in future work.

8.1 Summary of Formalisms

8.1.1 Landauer Theory

Most molecular conductivity calculations are based on the Landauer description where molecular conductance is associated with noninteracting scattering electrons. [53] In this approach conductivity is evaluated by integration over quantum mechanical transmission-

$$I(V) = e/h \int T(E)[f_l(E, \mu_l) - f_r(E, \mu_r)]dE, \tag{8.1}$$

where T is the (molecular) transmittance function and f_l and f_r are the Fermi distributions of the leads. The transmission function peaks at different molecular electronic levels due to scattering events through the conductor.

The quantum transmission is then evaluated from the device Green's (G_c) and broadening functions ($\Gamma_{l,r}$):[106]

$$T(E) = tr[G_c^R \Gamma_l G_c^A \Gamma_r]. \tag{8.2}$$

The broadening functions describe the effect of the random scattering events in the metal contacts on the molecular states. These functions are related to the coupling of the conductor to the contacts (the self-energies) by:

$$\Gamma = i[\Sigma - \Sigma^\dagger]. \tag{8.3}$$

8.1.2 Constant Potential Theory

A Dynamically-Driven view of the Steady-State transport

The Keldysh approach, which considers the full correlation effects of the electronic density at non-equilibrium conditions,[13, 57, 14, 70, 18] provides an important alternative to the widely used scattering models, which use a static (equilibrium) foundation for the description. Recently, we have implemented several solutions of

the electronic equations of motion (K-B equations) of a model open system under non-equilibrium conditions. [99] In this report we use the full dynamical treatment to derive a simplified expression for describing the system under steady state conditions. This is in contrast to most treatments limited to steady state, which are based on tractable one-variable expressions. We use our methodology to demonstrate that a dynamical perspective is necessary to model reliably the resulting steady state.

Our starting point is the electronic equation of motion (e.o.m.) of the coupled system, where the electronic structure of the bulk is projected on the device region using the electrode's self-energy (eqn. 6.9):

(8.4)
$$i\frac{\partial}{\partial \bar{t}}\mathbf{\Delta G}^{<}(\bar{t},\bar{\omega}) = [\mathbf{h},\mathbf{\Delta G}^{<}(\bar{t},\bar{\omega})] + \int d\omega'[\mathbf{v}(\bar{t},\omega')\mathbf{G}^{<}(\bar{t},\bar{\omega}-\omega') - \mathbf{G}^{<}(\bar{t},\bar{\omega}+\omega')\mathbf{v}(\bar{t},\omega')] + \int_{-\infty}^{\infty} dt'[\mathbf{\Sigma}^{\mathbf{R}}(\bar{t}-t')\mathbf{\Delta G}^{<}(t',\bar{\omega})e^{-i\mathbf{h}(\bar{t}-t')} - e^{i\mathbf{h}(\bar{t}-t')}\mathbf{\Delta G}(t',\bar{\omega})\mathbf{\Sigma}^{\mathbf{A}}(t'-\bar{t})].$$

Here $G^{<}(\bar{t},\bar{\omega}) = G^{0,<}(\bar{\omega}) + \Delta G^{<}(\bar{t},\bar{\omega})$, where $G^{0,<}$ is the lesser GF at fully equilibrated conditions and is used as the initial guess for the propagation. Recently, we have used a solution to the e.o.m. expressed in the full frequency domain (eqn. 6.14),

(8.5)
$$\boldsymbol{G}^{<}(\Delta\omega,\bar{\omega}) \equiv \int_{-\infty}^{\infty} d\bar{t} e^{i\Delta\omega\bar{t}}\boldsymbol{G}^{<}(\bar{t},\bar{\omega}),$$

to study electronic spectra under non-equilibrium conditions. Here we use the full-frequency domain expressions to analyze the steady state limit of the equations.

We now use the two-frequency representation of the time-dependent equations of motion to derive a time-independent correction to $G^{0,<}$. We note that a time independent perturbation $\mathbf{v}(t) = \mathbf{v}$ can be Fourier transformed as in eqn. 8.5. Its counterpart in the frequency domain is given by eqn. 6.30,

(8.6)
$$\mathbf{v}(\Delta\omega) = 2\pi\delta(\Delta\omega)\mathbf{v}.$$

This simplifies the expression by eliminating a convolution integral term ($\Delta\omega \to 0$) and can be written as:

$$-[h_0 + v, \Delta G^<(\bar{\omega}) = [v, G^<(\bar{\omega})]. \tag{8.7}$$

This will allow to compare the treatments for the transport at steady state conditions, where all transient aspects and other time-dependent effects are fully dissipated. We will refer below to our approach for modeling the steady-state as the dynamically driven description of steady state (DDSS) approach.

As usual, we designate subspaces for the device (C) and electrodes (generic I), solving for $\Delta G^<_{CC}$ by two equations:

$$-h_{CI}\Delta G^<_{IC} - h_{CC}\Delta G^<_{CC} + \Delta G^<_{CI}h_{IC} + \Delta G^<_{CC}h_{CC} = [v_{CC}, G^<_{CC}], \tag{8.8}$$

and

$$-h_{II}\Delta G^<_{IC} - h_{IC}\Delta G^<_{CC} + \Delta G^<_{II}h_{IC} + \Delta G^<_{IC}h_{CC} = v_{II}G^<_{IC} - G^<_{IC}v_{CC}. \tag{8.9}$$

We also omit from the expression the dependence of the G on $\bar{\omega}$. We will continue to use this shorter notation in the next equations for G and ΔG.

We proceed in the representation spanned by the eigenvectors (with $\{\epsilon_i\}$ as values) of the voltage affected device region ($h_v = h_0 + v$). In this representation eq. 8.9 becomes:

(8.10)

$$\Delta G^<_{IC,ij} = [g^R_{II}(\epsilon_j)h_{IC}]_{ik}\Delta G^<_{CC,kj} - [g^R_{II}(\epsilon_j)\Delta G^<_{II}]_{ik}h_{IC,kj} + g^R_{II}(\epsilon_j)[v_{II}G^<_{IC} - G^<_{IC}v_{CC}]_{ij},$$

For clarity we noted the indices in the last expression. We further clarify that we are expanding this using voltage affected device vectors, where ϵ_j are the values. Namely, in this representation:

$$-h_{v,II}\Delta G_{IC} + \Delta G_{IC}h_{v,CC} \to (\epsilon_j\delta_{ik} - h_{v,II,ik})\Delta G_{IC,kj} \equiv (g^R_{II,ik})^{-1}(\epsilon_j)\Delta G_{IC,kj}. \tag{8.11}$$

Similarly

$$-h_{CC}\Delta G_{CC} + \Delta G_{CC}h_{CC} \to -(\epsilon_i\delta_{ik}\Delta G_{CC,kj} - \Delta G_{CC,ik}\delta_{kj}\epsilon_j). \tag{8.12}$$

Also $\Delta G^{<}_{CI,ij} = -\Delta G^{*<}_{IC,ji}$. We also define as usual the SEs:

$$\Sigma^R(\epsilon) = h_{CI}g_{II}(\epsilon)h_{IC}. \tag{8.13}$$

These relations are next inserted into 8.8 for the same bias shifted diagonalized device space and for clarity with expanded indices becomes

(8.14)

$$(-\Sigma^R(\epsilon_j)_{ik} - \epsilon_i\delta_{ik})\Delta G_{CC,kj} + (\Sigma^A(\epsilon_i)_{kj} + \epsilon_j\delta_{kj})\Delta G_{CC,ik} =$$

$$[v_{CC}, G^{<}_{CC}]_{ij} - [h_{CI}g^R_{II}(\epsilon_i)\Delta G^{<}_{II}h_{IC}]_{ij} + [h_{CI}\Delta G^{<}_{II}g^A_{II}(\epsilon_i)h_{IC}]_{ij}$$

$$+[h_{CI}g^R_{II}(\epsilon_j)v_{II}G^{<}_{IC} - h_{CI}g^R_{II}(\epsilon_j)G^{<}_{IC}v_{CC} - G^{<}_{CI}v_{II}g^A_{II}(\epsilon_i)h_{IC} + v_{CC}G^{<}_{CI}g^A_{II}(\epsilon_i)h_{IC}]_{ij}.$$

We also define, for convenience, the device-space voltage affected propagator as:

(8.15)

$$\mathcal{H}_v\Delta G_{CC,ij}(\bar{\omega}) \equiv \Sigma_k(-\Sigma^R(\epsilon_j)_{ik} - \epsilon_i\delta_{ik})\Delta G_{CC,kj}(\bar{\omega}) + (\Sigma^A(\epsilon_i)_{kj} + \epsilon_j\delta_{kj})\Delta G_{CC,ik}(\bar{\omega}).$$

For the final simplification we use the equilibration relation for the electrodes' quantities, where the Fermi function is used to occupy the lowest levels up to the Fermi energy. We emphasize that the equilibration relations are not used to impose the overall electronic properties of the junction space but rather use the proper bulk domain properties. This amounts to

$$G^{<}_{II}(\bar{\omega}) = f(\bar{\omega} + v_I)(g^A_{II}(\bar{\omega}) - g^R_{II}(\bar{\omega})), \tag{8.16}$$

where by assuming $f_{IC} = 0$ one can show that

$$G^{<}_{IC} = g^R_{II}h_{IC}G^R_{CC}f_{CC} - f_{II}g^A_{II}h_{IC}g^A_{CC}, \tag{8.17}$$

and $G^{<}_{IC} = -G^{<\dagger}_{CI}$. We also note the we denote $g^{R/A}_{CC}$ as the retarded/advanced GFs of the device region w/o the self-energies.

The final equation is then generated where in the chosen (bias affected) representation:

$$\begin{aligned}
\mathcal{H}_v|\Delta G^{<}_{CC}\rangle &= v_{CC}G^{<}_{CC} \\
&+f(\bar{\omega}+v_I/2)[h_{CI}[g^{A}_{II}(\bar{\omega})-g^{R}_{II}(\bar{\omega})]g^{A}_{II}(\epsilon_i)h_{IC}] \\
&+h_{CI}g^{R}_{II}(\epsilon_j)g^{R}_{II}(\bar{\omega})\bar{h}_{IC}G^{R}_{CC}(\bar{\omega})f_{CC}[v_I I_{CC}-v_{CC}] \\
&+h_{CI}g^{R}_{II}(\epsilon_j)g^{A}_{II}(\bar{\omega})h_{IC}g^{A}_{CC}(\bar{\omega})f(\bar{\omega})[v_I I_{CC}-v_{CC}] \\
&+\text{conj. transpose}
\end{aligned} \tag{8.18}$$

(AP-check last equation) This is done in a diagonal representation for the bulk states, where $f_{IC} = 0$. To further clarify, we assume that v_{CC} includes at least one of the potential shifted site of each bulk in the device region and $v_I I_{CC}$ amounts to project the bias of one electrode on all the device region ($v_l + v_r \equiv= 0$ and I is the identity) We also define the bulk-coupling dependent terms on the RHS (excluding the first term and its conjugate transpose) as $\mathcal{G}(\bar{\omega})$.

The total density under bias effects can now be generated by integrating the responded $G^{<}$ as calculated by eq. 8.7 with respect to $\bar{\omega}$:

$$\rho = -i\int d\bar{\omega}\mathbf{G}^{<}(\bar{\omega}). \tag{8.19}$$

This can also be expressed in a form for the total density as (eqn. 7.14),

$$|\rho_v\rangle = |\rho_\circ\rangle + \mathcal{H}_v^{-1}\int d\bar{\omega}|[v, G^{0,<}(\bar{\omega})]\rangle. + \mathcal{H}_v^{-1}\int d\bar{\omega}\mathcal{G}(\bar{\omega}) \tag{8.20}$$

Electron Transport through model two-state systems

We next solve for the transport properties of a model system by both the simple Landauer scheme and the DDSS approach. For illustrating the effects of the dy-

namical approach we consider a 2 state model as the device region embedded within two wires through tight-binding type of interactions as routinely implemented in transport calculations. This is illustrated in Figure 7.1. In the considered model two-state systems, the device region is defined by bands of the ground state and of the excited-state. The two-state system The Hamiltonian **h** and the perturbation operator **v** in the atomic-orbital representation expressed in the device region are (eqns. 7.16, 7.17):

$$\mathbf{h} = \begin{bmatrix} -i\Sigma & \beta \\ \beta & -i\Sigma \end{bmatrix}, \tag{8.21}$$

and

$$\mathbf{v_{CC}} = \begin{bmatrix} v/2 & 0 \\ 0 & -v/2 \end{bmatrix}. \tag{8.22}$$

where $-i\Sigma$ represents the effect of the electrodes and effectively turns the two states into conducting channels by contributing the broadening effects. The surface GF is designated as g.

We now apply a wide band limit approximation to the bulk and for further simplicity express the TB site of the bulk by a single basis function. We denote the coupling parameter within the two states by β_w. Here $\Sigma \equiv \beta_w^2 g$ and $g \equiv 1/\beta_w$, a choice that optimizes the resonant tunneling across the interface.

Equation 8.18 simplifies to:

(8.23)

$$\mathcal{H}_v|\Delta G^<_{CC}\rangle = (1-(\Sigma/\beta)^2)[v_{CC}, G^<_{CC}] + f(\bar{\omega}+v_I/2)(\Sigma^A_I(\epsilon_j) - \Sigma^R_I(\epsilon_j))2i\Sigma/\beta^2.$$

The current operator for tracing the current between the two junctions' sites has

the form (eqn. 7.18),

$$\mathbf{j} = \mathbf{i} \begin{bmatrix} 0 & -\beta \\ \beta & 0 \end{bmatrix}. \tag{8.24}$$

The ground-state density matrix ρ has the form

$$\rho = i \int d\bar{\omega} f(\bar{\omega}) \begin{bmatrix} 1/(\bar{\omega}-\beta)^2 + \Sigma^2 & 0 \\ 0 & 1/(\bar{\omega}+\beta)^2 + \Sigma^2 \end{bmatrix}, \tag{8.25}$$

when the electron population is in the ground conducting channel.

8.2 Results

Steady state conductivity comparison

Linear response. Next, for comparing the Landauer result for the transport of the two state system to the DDSS expression we apply a first order expansion in term of the applied voltage. The first order assumes that the source drain bias is weak enough (compared to the bandwidth of or energy spacing between conducting channels). This is applicable for the low bias limit we are considering and has been used in implementing the TD perturbation treatment as detailed above. The current expression can be expanded by a Taylor series in the source-drain bias. The first order is

$$I^{(1)}(v) = \left(\left. \frac{dI}{dv} \right|_{v=0} \right) v, \tag{8.26}$$

where $I(0) = 0$. The derivative in eqn. 8.26 is the conductance evaluated at zero bias.

In the Landauer formulation, only the Fermi functions depend on v (eqn. 8.1). At $T = 0K$, the Fermi functions can be written in terms of Heaviside step functions

$$f(\epsilon) = 1 - \Theta(\epsilon - \mu). \tag{8.27}$$

Thus at low temperatures the derivative of a Fermi function is proportional to a delta function, and the current, in the limit of linear response, is expressed simply by the transmission function evaluated at the Fermi energy (μ_0)

$$I^{(1)}(v) = T(\mu_0)v. \tag{8.28}$$

For the considered two conducting channel system, the transmission gives the following expression for current,

$$I^{(1)}_{\text{Landauer}}(v) = \frac{4\beta_d^2\Sigma^2}{2\pi(\beta_d^2+\Sigma^2)^2}v. \tag{8.29}$$

Extracting the first order CPT term in the bias for this example leads to a different expression for the conductance:

$$I^{(1)}_{\text{DDSS}}(v) = \left\{(\Sigma^2-\beta_c^2)(\pi + 2tan^{-1}(\frac{\Sigma}{2\beta_d} - \frac{\beta_d}{2\Sigma})) + 4\Sigma\beta_d\right\}\frac{\beta_d\Sigma}{4\pi\beta_c^2(\beta_d^2+\Sigma^2)}v. \tag{8.30}$$

The first order expansion of the DDSS scheme essentially assumes no voltage dependence of the propagator $G_{v_\circ}(\Delta\bar{\omega})$.

We now compare the steady state conductance of the two state systems as obtained from the Landauer (eq. 8.29) formalism and by the DDSS treatment (eq. 8.30). The dependence of the conductance on the electronic interaction parameters according to these two expressions is plotted in Figure 8.1. In the plot, the electronic interactions are parametrized by the ratio $\alpha \equiv \beta_d/\beta_w$, which is defined above within the model (fig. 7.1).

We now remark on the physical relevance of the α parameter at different regimes of its numerical value. Physically, the low value limit of α corresponds to a molecular system that is only weakly coupled to the electrodes and therefore it acts as an insulator. Its conductance increases as the coupling to the electrodes is increased up to

Figure 8.1: The conductance of a two state model system as a function of the electronic interaction integrals represented by β/Σ (see text), evaluated by the first order expression of the Landauer-based and the dynamic-based expansions. The left curve provide closer look at the low α region of the scale.

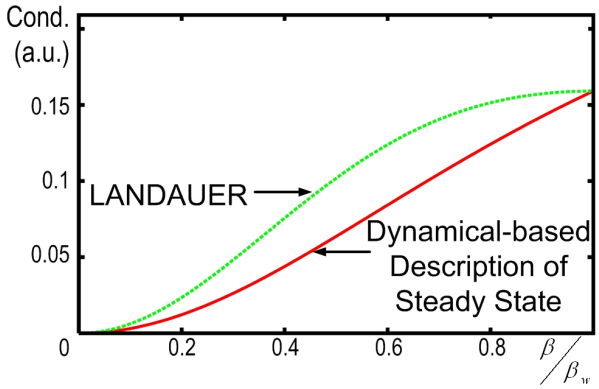

the limit where it becomes fully coherent, where $\alpha = 1$. Namely, the orbitals are exactly delocalized through the system, which corresponds to a perfect one dimensional wire of tight-binding sites.

I-V analytical results.

We now consider conductivities as evaluated by the two theories for channels with different α values. This is described by eqn. 8.29 and by eqn. 8.30 for the DDSS and Landauer approaches respectively. In Figure 8.2 we provide the analytically evaluated I-V relations for three α values: 1, 0.5 and 0.1. For 1 as discussed above we have a fully coherent system. The smaller values correspond to molecular systems. The divergence of the Landauer-based estimate from the current as evaluated by the DDSS approach is the smallest for channels identified by α values that are closer to 1. It is, however, the lower α value which is more relevant for molecular systems and which are associated with stronger resistance properties. In this regime the divergence of the current as expected from the conductance observation is increased.

It is, therefore, interesting to note that the divergence is much more apparent at the low α limit. As the system becomes more coherent, on the other hand, the

Figure 8.2: The current (I(V)) of the two state model system with different values of the α parameter

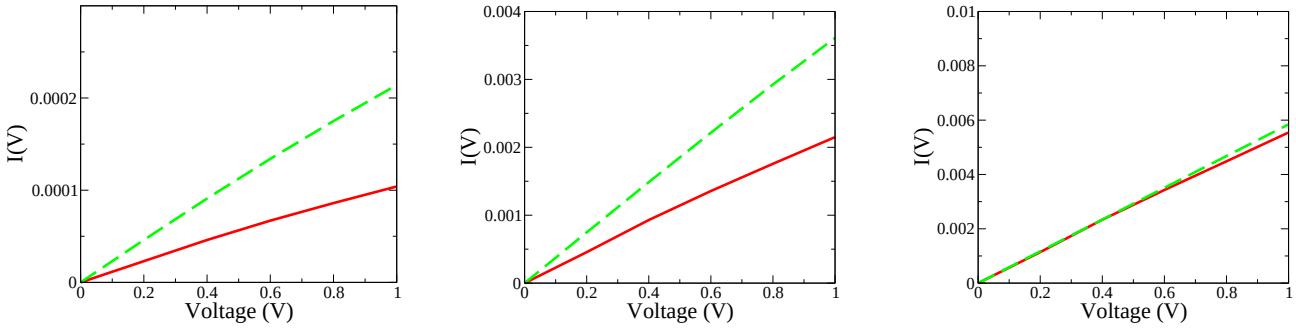

divergence of the Landauer description becomes smaller. The results demonstrate that as the system becomes more coherent and/or at the low voltage limit the Landauer scheme will agree better with the dynamic description. Here the coherence is measured and compared by the ratio between the strength of the internal electronic interaction to the coupling to the electrode. This agreement is especially improved for the higher α values regime.

8.3 First steps toward molecular systems: Landauer calculation on C6 wire

In this section, the Landauer method is benchmarked on a density functional theory Hamiltonian for a more realistic six carbon molecular junction connected to gold wires using an LANL2DZ basis set and effective core potential for the metallic atoms. This is the first step in benchmarking our CPT approach against Landauer on a real system. In order to achieve this, we must first benchmark Landauer theory on such a system to ensure that we have defined our device and electrode regions to give converged results.

Models The benchmarking is performed on a set of 1-dimensional model systems. The molecular device is based on a linear chain of carbon atoms (cumulene) and is depicted in figure 8.3. A chemically more complex system, where a pair of electron withdrawing and donating groups are added is also considered. This is achieved by bonding a NO_2 to one edge carbon and a NH_2 group on the other edge carbon. This allows us to generalize the considered electronic structure features which are important for electron transport properties. These cumulenes are then bonded to 1-dim electrodes, as depicted in fig. 7.1.

Conductance studies employing atomistic gold have been applied, for example, to study magnetoresistance of molecular devices.[49, 50, 52] One-dimensional atomic bulk models have been shown to reproduce dominant trends observed with larger surface models employing the Landauer description as well.[51] In addition, this is an important model system simulating a single atom link between the thiol and the gold surface which exists in several experimental setups as indicated by Tao et al[131, 130]. In their experiments, a STM tip is used to pull a string of gold atoms off the surface[137, 92] leading eventually to the ability to bind a single di-thiolated molecule between two fragments of a gold atom wire. In addition we also consider variants of these systems where the bulk consists of Al atoms and/or the molecular geometry is allowed to bend out of the line defined by the electrodes. Transmission calculations implement the Green function formalism as described above on these different systems, where the transport is considered to occur through the molecular device immersed between the two semi-infinite bulk materials. Below we focus on results obtained with gold model. The other considered systems feature similar trends.

Within the GF formalism the effect of the infinite bulk on the molecular system is

achieved by projection on pre defined subspaces. This involves calculating the bulk's self energy models. Therefore, the implementation of the Green function formalism requires several choices. These define the size of the immersed device, namely, the number of metal atoms included in the device region. Next, a decision on the size of the electronic structure matrix, which is used to represent the bulk must be made. This is equivalent to studying the extent that delocalization effects in the metal are important to describe correctly the bulk-conductor interaction. In the TB scheme, a smaller repeating unit implies more truncation of such long range effects. The TB calculation is implemented with the α and β parameters (see eq. 5.39) obtained at the DFT level described below.

The choices that define the partition of the system are illustrated in fig. 7.1. In the figure, **M** is the number of metal atoms included with the device and **L** is the total number of gold atoms included in the electronic structure calculation. **N** is the number of bulk atoms included in the repeating TB unit. The size of the TB period defines the extent of truncation of long range electronic integrals included in the α and β TB parameters. In this scenario, for example, all basis functions on atoms which are more than N+M layers away from the edge (but still within L) are not included through the TB expansion. It is useful to note that this scheme does not vary the nature of the repeating unit but merely is a tool to determine the extent of electronic integral truncation within the coupling terms. A set of these three numbers defines the self energy model used in the transmission evaluation and will be referred to below by **L(M)-N**. Clearly for sufficiently large L, M and N values the model choice becomes converged as it does not introduce arbitrariness into the resulting calculated transmission. In the discussion below we study the radius of convergence of these choices for transmission calculations.

Electronic structure information is obtained for cluster models including the molecule and finite metal wires as described above. Twenty-four metal atoms are included on each side of the considered molecule, unless otherwise noted, at a density functional level of theory. The DFT calculation employs the B3LYP functional[15, 16] with a LANL2DZ ECP basis set[125] for the transition metal atoms and 6-31G for all other atoms. In all electronic structure calculations, the overall spin and charge of these systems, unless otherwise stated, is a neutral singlet. The electronic structure calculations were implemented using a prerelease version of Qchem 3.0[107] and the transmission calculations were performed with a code developed in our group.

Device (M) convergence. We begin our benchmarking discussion by inspecting the convergence of the SE models with respect to M. This corresponds to the part of the electrode where screening effects and relaxation due to the adsorption are dominant. Therefore, M corresponds to the number of gold atoms included in the contact region. Namely, we are considering the depth to which the surface adsorption causes a significant perturbation on the electronic structure of the electrode layers. First, we consider the plain non-polar cumulene bonded between two gold atom chains. *The calculated transmission functions are described by projection on a color contour, where the bright color region corresponds to T=1 and darker regions represent smaller transmission amplitudes.* This allows to follow clearly the convergence of a calculated series of transmission functions.

Figure 8.5 provides the projected calculated transmission functions for different M values with the L and N values kept constant (L=24 and N=2 (left part) or N=3 (right)). All transmission plots involve a single peak near the Fermi-energy (FE) of the bulk electrode. At the WBL level of bulk representation there is no influence on increasing the bulk period size (N value). This is confirmed by comparing the

two parts of the figure. However, the plots highlight a parity divergence, where the height of the peak converges differently depending on whether M is odd or even. Therefore, the use of SE models calculated with the WBL description for the bulk must ensue in arbitrary performance which depends on the M value.

Next we consider the same sequence of transmission plots with, however, a full TB treatment of the bulk. Figure 8.6 describes the corresponding plots. With the TB bulk treatment, it is apparent that the odd-even parity can be lifted. However, while most of the disparity is eliminated already with N=2 plots (left side of the figure), almost complete elimination of the remaining divergence is demonstrated with an N odd value (N=3 in the right side). This small M parity with even N is removed only for large enough N value. Namely, with odd N values a much faster convergence of the transmission plots is generated. This trend is demonstrated in Figure 8.7, where the functionalized cumulene is considered. In the figure we follow the differences between devices defined with odd and even M values (4 and 5) when coupled with an even or odd bulk N value. In part (a) the transmission curves with even N values are shown to reduce the parity only at N=6 or 8, where the two curves with N=2 are shown to differ substantially. In part (b) the use of an odd N parameter leads to a faster convergence at N=3 or 5. In (c) the convergence of the odd and even with sufficiently large N cases is demonstrated. Next, we further consider the generality of the observations by calculating the M sequence of the transmission plots with the more complex cumulene which involves the polarizing groups.

The M dependence plots of the functionalized cumulene using the WBL and TB approximations for modeling the bulk are provided in figures 8.8 (WBL) and 8.9 (TB). The transmission plots in the figures are calculated with a small imaginary shift value (smear factor) added to the Hamiltonian of the device region when solv-

ing for the device GF as in eq. 5.5. For the curves in part b (right side) a larger device shift factor is employed. This larger value allows to further "smear" the electronic structure features of the MW and therefore highlights the main features of the molecular transmission pattern, where the dominant broadening effects due to the bulk are emphasized.

Indeed, the polarized cumulene transmission plots feature more structure as expected when compared to the plain cumulene results. However, the main observed transmission features confirm our discussion comparing the TB and WBL based approaches. Namely, the use of the TB model in calculating the bulk's GF results with a converging model. Evidently the performance of the crude WBL approximation for describing the bulk (fig. 8.8) in the calculation of transmission through the polarized cumulene is even worse than for the non functionalized cumulene. The WBL plots clearly demonstrate a divergence that cannot be reduced by increasing the N bulk parameter. This observation is confirmed also as outlined above after using a a larger shift factor. This factor is added to the device Hamiltonian in obtaining its GF. The same observations on the WBL divergence of the transmission function are maintained with the larger factor (see fig. 8.8(a) and (b)). The TB curves illustrated in fig. 8.9, on the other hand, provide a convergent series.

Next we comment on the origin of the difference in the M performance for the WBL and TB based models. In WBL, the device' transmission pattern is determined by the parity of the last atom included in the device space. The coupling to the simplified bulk models in the WBL is unable to compensate for the device electronic structure differences between including an even or odd number of bulk atoms in the device subspace. This situation is rectified by using a more complex bulk GF generated by the explicit TB treatment of the bulk. Namely, the TB is capable by appropriately

coupling to the variety of the electronic states of the device region to produce a consistent description as evident from the M series transmission plot. These trends have been verified to persist in both singlet and triplet spin coupling schemes. We note, however, that TB still involves small divergence with respect to the M factor. The effect of this small divergence on calculated conductance or I-V plots is, however, negligible. In addition, this can be further reduced by increasing the N parameter. However, the M convergence is slower for even values of N, while the performance of M series with odd values of N is shown to provide a faster converging set of plots.

Most of the remaining M-value related divergence observed at the TB level is in a form of minor changes in the transmission function at around -7.6eV, which are emphasized by the smaller shift factor (fig. 8.9(a)). The smaller shift factor allows expression of these features in the transmission plots. These originate from the electronic DOS of the gold atoms included with the device. The number of these localized peaks increases with the number of gold atoms included within the device. However, their overall contribution to conductance is minute since these are not broadened significantly and are well distant from the FE. Overall, it is important to note that both sets are shown to converge to similar transmission patterns. Therefore consistent conductivity plots correspond to these converged M values series. To summarize this discussion, the crude description employing the WBL approximation for the bulk fails to provide consistent transmission with regard to the device parameter. This highlights the need for the more accurate TB description of the bulk. These observations are noted also for the calculated transmission of the other systems considered in this work. Next, we study the convergence of the bulk size parameter included in the TB model.

Bulk (N) convergence. We now turn to study the convergence of the SE models

with respect to the size of the space used to define the repeating unit in the bulk's TB calculation. A larger N factor allows a more complete description of bulk electronic delocalization effects through the TB parameters, where electronic integrals over atomic orbital indices with larger inter-bulk-atom distances are included. This is the size of the subspace that is considered to be the repeating unit in the bulk periodic material. The transmission curves calculated with varying N values and setting M=3 and L=24 are plotted in figure 8.10. The provided plots demonstrate an overall fast convergence with respect to this bulk unit size parameter. The two parts of the figures correspond to different shift factors which are used with the bulk's GF calculation.

We first focus on the plots provided on the left side of the figure, which employ the smaller bulk shift factor. Several features related to the bulk model are shown to converge slowly with the N value. These are manifested as strongly localized deep wells and peaks of the overall transmission plot, which are eliminated when a large enough bulk is included. This demonstrates the effect of using a truncated bulk model for describing a metallic system. Only large enough models, which include enough of the bulk long range interactions can better describe the delocalized nature of the metallic bulk. We note, however, that these discretization effects also have only a marginal effect on the integrated transmission (of course only when a sufficiently large bulk space is used).

These cluster effects in the bulk model can also be treated within the bulk GF calculation. With the larger smear factor the convergence of the curves is even faster with N = 3 or 4 as provided in the right part of the figure. These observations also are consistent for all the considered systems, including the Al bulk calculations, the various molecular orientations and the polarized and plain cumulene systems. We next turn to study the effect of the cluster model size used in the electronic structure

calculation on the evaluated transmission.

Electronic structure cluster model (L) convergence. Next, we consider the effect of using a truncated cluster model for describing the interaction of the bulk with the transporting molecule. This is implemented by repeating the transmission calculation with varying the number of bulk atoms included in the electronic structure calculation. This amounts to repeating the evaluation of the supermolecule electronic structure with a modified L value. The transmission plots where N and M are each set to three and with the changing L values are provided in figure 8.11.

In figure 8.11 different limits for the odd and even cases of the L value are demonstrated. It is also apparent that fast convergence is exhibited for the even and odd cases separately. Not more than 3 atoms over the size defined by N+M are needed to converge each of the odd or even series. The few atoms added beyond N+M atoms reduce small edge effects. These edge effects are shown to only shift or increase moderately the transmission peaks. As noted above, however, the results indicate a disparity of the transmission between the odd and even L values. This divergence originates from the open shell character of the gold atoms. This is indicated also by simply noting that the HOMO-LUMO gap and energies depend on the parity of the number of gold atoms included in the electronic structure calculation. Therefore, an essentially different transporting material is modeled by merely choosing the number of gold atoms in the cluster model calculation. This stems from the different inter-atomic spin coupling schemes involved with varying the parity of the number of open shell metal atoms included in the model.

Figure 8.3: The molecular systems considered include a cumulene bonded between gold or aluminum wires. In addition we have considered a functionalized cumulene as indicated by the NO_2 and NH_2 polarizing groups added to the edge carbons. We have also considered bent structures where the cumulene is not on the same line defined by the two electrodes.

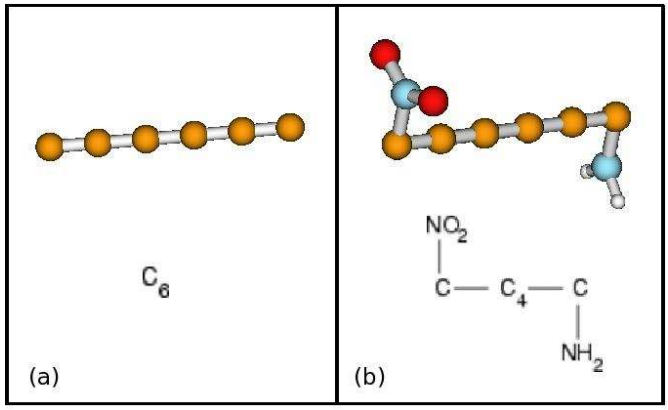

Figure 8.4: The self energy models are defined by three integer values as indicated in the figure. L denotes the total number of metal atoms included in the cluster calculation for representing each electrode. M are the number of metal layers included with the device after partitioning the system and N defines the length of inter-atom interactions included in defining the bulk. The subspace defined by N is the repeating unit assumed for the periodic bulk material.

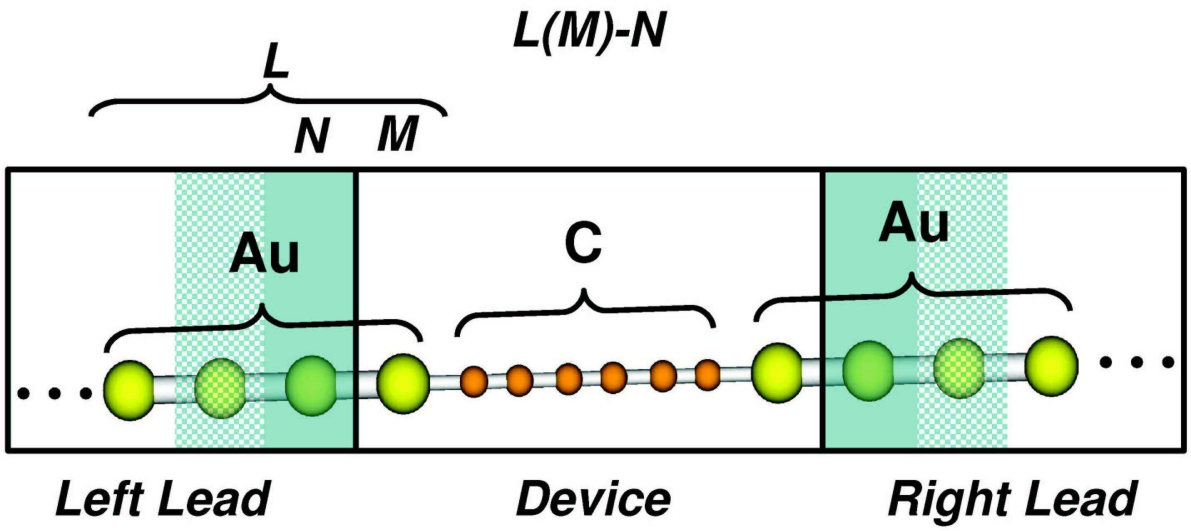

Figure 8.5: Color-coded transmission plots of the non-polar cumulene calculated with varying the space of included gold atoms with the device (M). The bulk is represented by the WBL approximation. The size of the repeating period of the bulk is (a) two (N=2) (b) three (N=3).

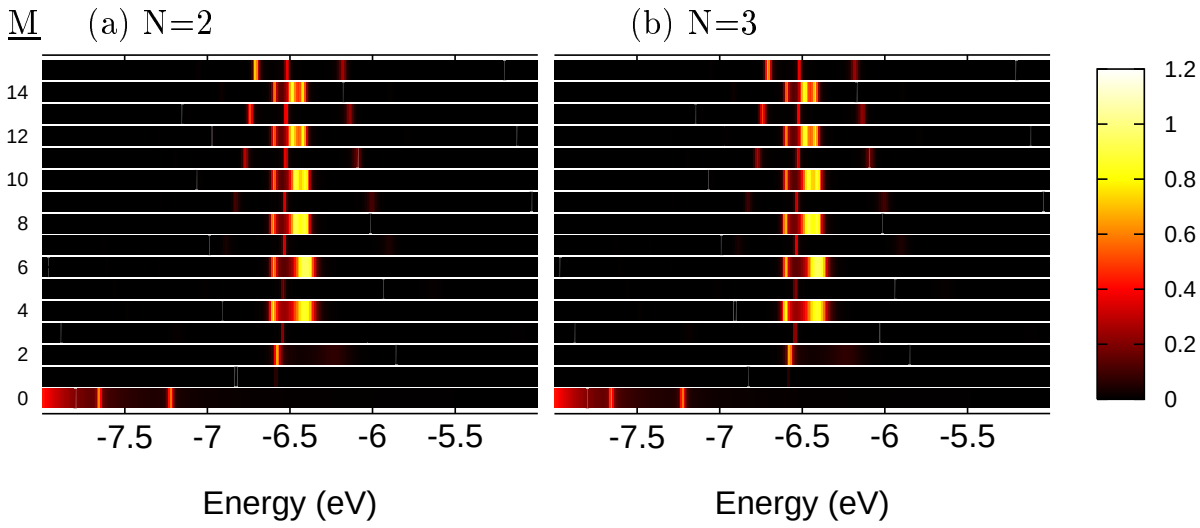

Figure 8.6: Color-coded transmission plots of the non-polar cumulene calculated with varying the space of included gold atoms with the device (M). The bulk is represented by an explicit TB calculation. The size of the repeating period of the bulk is (a) two (N=2) (b) three (N=3).

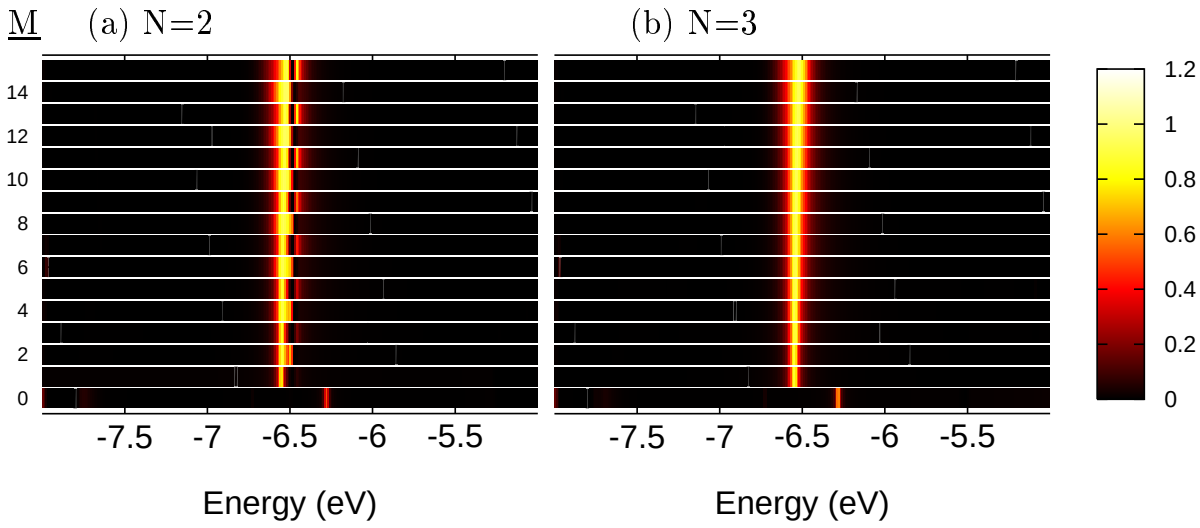

Figure 8.7: Transmission plots of the polar cumulene. The disparity between using 4 or 5 gold atoms in the device is compared for different choices of the bulk parameter (N). Tranmsission (a) for even N values converges at N=8. (b) for odd N values convergence at N=5. (c) Converged transmission for odd and even N at N=5 and N=8.

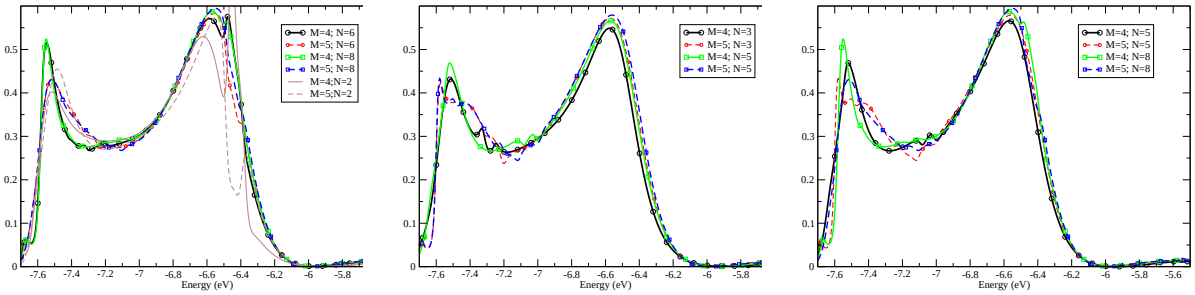

(a) Even bulk (b) Odd Bulk (c) Bulk Convergence

Figure 8.8: Color-coded transmission plots of the polarized cumulene calculated with varying the space of included gold atoms with the device (M). The bulk is represented by a WBL approximation with (N=3). The shift factor used in calculating the device GF is (a) 0.001eV (b) 0.01eV.

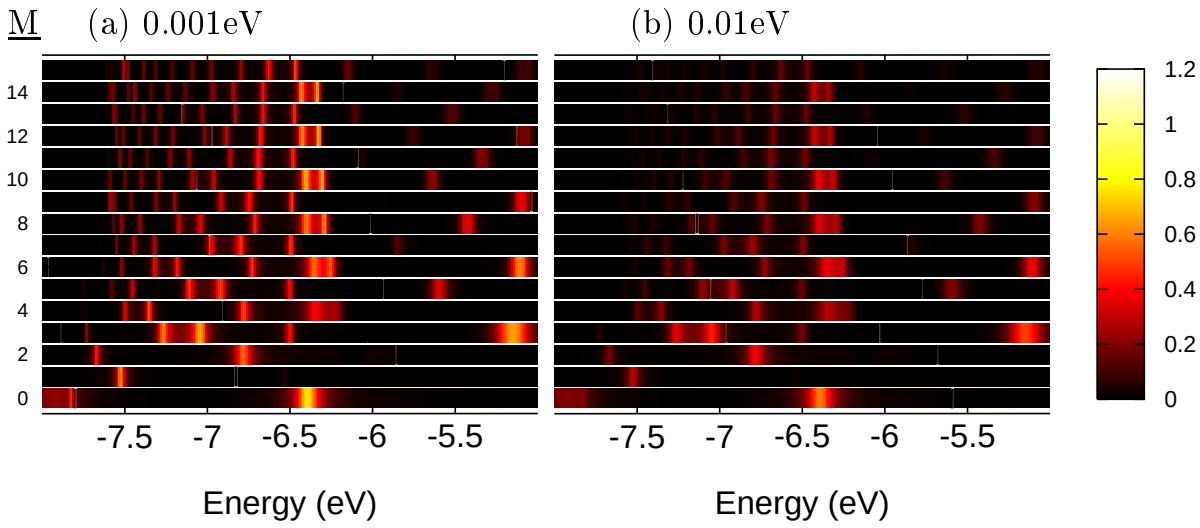

Figure 8.9: Color-coded transmission plots of the polarized cumulene calculated with varying the space of included gold atoms with the device (M). The bulk is represented by an explicit TB calculation with (N=3). The shift factor used in calculating the device GF is (a) 0.001eV (b) 0.01eV.

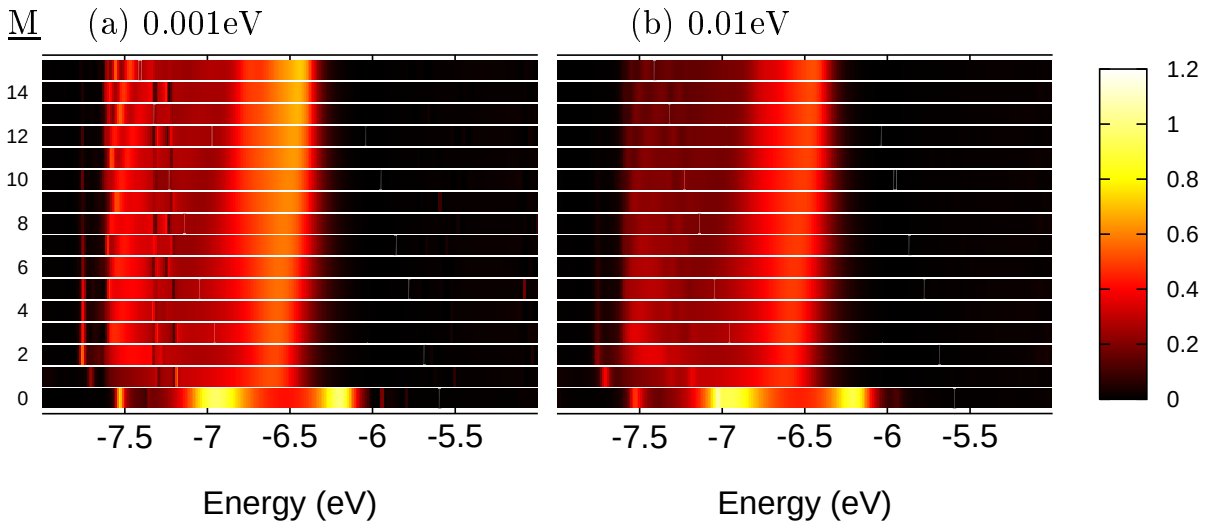

Figure 8.10: Color-coded transmission plots of the polarized cumulene calculated with varying the size of the repeating unit for describing the bulk. The device space is set constant (M=3). The shift factor used in calculating the bulk GF is (a) 0.001eV (b) 0.026eV.

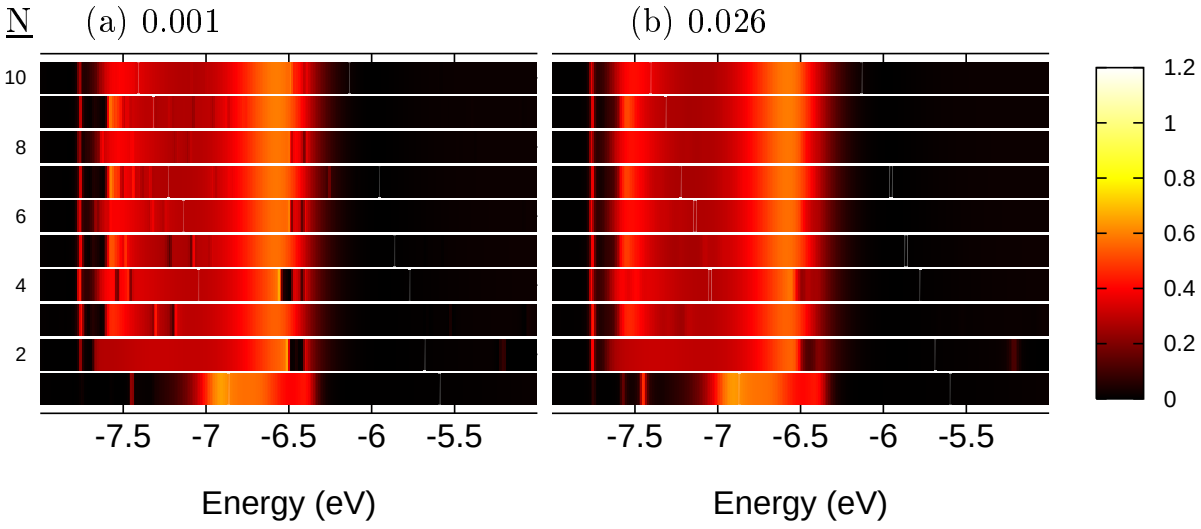

Figure 8.11: Color-coded transmission plots of the polarized cumulene calculated with varying the number of gold atoms included in the model used in the electronic structure calculation (L).

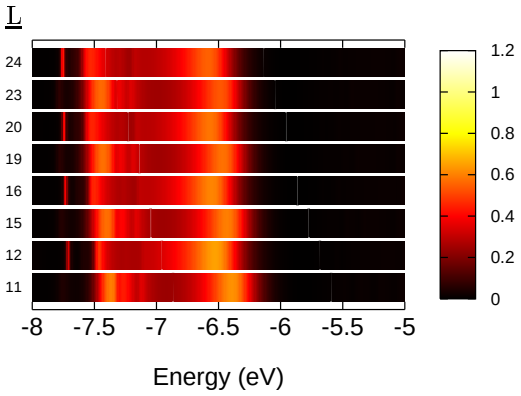

CHAPTER IX

Summary

A formalism based on propagating the K-B electronic e.o.ms is implemented to study transient and TD effects of current through model electronic-channels. This is achieved by solving the equations of motion in a mixed time-frequency representation. In this formalism, SE expressions in the energy domain represent the bulk effects on the electronic densities. Namely, bulk induced broadening effects on the device's electronic structure are directly included in the propagation. We also note that our approach is based on the more physical appropriate non-partitioned scheme[30] as recently pursued in real time treatments.[110, 65, 112]

Our approach by using the SE expressed in the frequency domain avoids the difficulties in propagating open systems in real time representation. This provides an efficient and reliable framework for including the contacts effects on electronic conductance. This provides the opportunity to benefit from highly efficient low order TD perturbation treatments and to avoid difficulties related to real-time propagations. The effectiveness of the linear response implemented here has been confirmed by its ability to reproduce the related steady state description upon a long enough constant perturbing DC bias. The low order perturbation treatment is highly useful in addressing weak perturbations where the 'bending' of the perturbed electronic

states can still be neglected. This approach as implemented, therefore, is useful for studying spectroscopy of open systems and transport under low bias perturbations.

Furthermore, as opposed to approaches based on real time propagation of density matrices, our approach treats directly the coupling of the device to the bulk system in the propagation. Namely, induced device-based mini bands are being propagated. This also allows to resolve the features within the bulk-induced mini-band that determine the transient conductance of the electronic channels. We relate the transient features to quantum interference effects between the device channels or present bound states.

We analyze in detail the interplay between the fundamental electronic parameters and the TD conductance through electronic channels. The parameters include the rate of potential switching event, electronic coupling strength between neighboring sites mediating the electron transfer and the overall electronic broadening factor representing a host of mechanisms leading to broaden the electronic state. Several time-dependent currents and their Wigner current distributions under different applied potential pulses, are compared. The system's ability to decay to its equilibrium state after bias turn off, or to achieve a pure DC current at constant bias, is studied. We show that optimization of the DC over AC response (or vice versa) can be attained by controlling the electronic coupling terms and/or shaping the applied TD potential pulse. The tuning of the broadening term was also shown to vary the quantum dephasing effects due to the electrodes and therefore to different decay rates of the AC/ringing response.

The effect of the presence of bound states on the conductance is also studied. The presence of device-bound states may result with long time persisting oscillations, which can dissipate only through other mechanisms. We find that the oscillatory

response due to bound state is dependent on a symmetry breaking scenario between the interfering bound states. Finally we have also studied the coherence driven AC and the effect of a present DC bias at the unperturbed state. The effect of the DC-induced band shift on the coherence driven AC response are analyzed using the Wigner form of the current distribution.

Furthermore, a recently developed approach for the propagation of the electronic density of a system coupled to electron reservoirs under dynamic non-equilibrium conditions is used to study electrode biasing effects on the electronic spectra. The projected equations of motion represent the effect of the electrodes on the dynamics expressed on the Keldysh contour, where the full time correlation is represented by two time variable propagators, the Green functions. The projection is achieved by using self-energy expressions to represent the effect of electrode coupling. In this report, the general equation of motion is reexpressed in the full frequency domain and is solved at the linear response level to obtain the electronic response to electronic perturbations represented in the dipole approximation.

This method is implemented on a model system involving two carbon atoms sandwiched by and aligned perpendicular to two gold atom wires. Exposing the system to steady non-equilibrium conditions, where the potentials of the two electrodes are shifted, leads to electron flux that dynamically affects the electronic spectra. Electronic transitions between conducting electronic channels, which are fully populated at equilibrium, become allowed upon applying voltage bias. It is shown that a transition involving two occupied states (at equilibrium) becomes stronger with the increase of the voltage bias, whereas the electronic flux can lead to some reduction of the transition for a transition coupling an occupied level to a virtual level.

This two-frequency approach was also used to study the phenomenon of absolute

negative conductance (ANC). It is found that ANC can be caused by population inversion where more population is transfered to an anti-bonding channel than to a bonding channel.

Finally, we addressed the need to extend our approach to including the effect of the source drain bias in the electrodes in order to get agreement with well established transport theories for non-interacting electrons at the ballistic limit. Transport through open quantum systems follows phase coherence of the charge carriers with the leads. For non interacting electron resistance arises through dissipation and backscattering at the source interface, where electrons are injected into the device. In the coherent regime this injection does not violate the exclusion principle.

We compare the steady state conductance through model electronic channels described by the widely used Landauer-based scheme to an approach derived from a fully dynamical perspective as provided by the Keldysh formalism. The full TD approach is reduced to treat the steady state of the model channels provide a rigorous scheme for consistent consideration of the equilibration effects. The Landauer approach, on the other hand, is based on imposing a simultaneous equilibration of the junction with two electrodes at different chemical potentials. These imposed equilibration assumptions lead to associate transmission spectra to the current. The two approaches, therefore, address fundamentally differently the injection process at the source electrode.

The Keldysh formalism based description (addressed here as the DDSS) avoids any of the equilibration model-approximation that are inherent to the Landauer scheme and therefore allows to quantify the impact of these approximations. The two theories are implemented on exactly the same electronic structure model. We scan the space spanned by the electronic parameters within models of 2 state channels

carrying the transport. The simplicity of the system is then used to derive analytical expressions for the I-V relations and conductances using the two approaches.

The results demonstrate that the Landauer scheme is bound to overestimate the conductance properties of the electronic channels. The divergence from the related exact result increases as the channel becomes less coherent. The divergence remains substantial for a wide range of the electronic parameters characterizing the channel. It is noted, that for parameters, which correspond to molecular-based systems, the results obtained by the Landauer scheme-based expressions overestimate the transport properties. *It is, therefore, shown that a dynamical perspective, which treats consistently the broadening effects, is required to enhance the ability to model conductance even at well established steady state conditions for non-interacting electrons.* This provides a fundamental explanation for the widely noted overestimation of conductances of molecular systems by state-of-the-art modeling and also suggests the requirements that need to be considered when devising approaches aimed to improve the description of the transport at steady state.

APPENDICES

APPENDIX A

Derivation of the Contour Ordered Expression for Dynamic Expectation Values

In this appendix, the expression for the expectation value of an operator, $O(t)$ in terms of KC ordering operators and propagators (eqns. 3.14-3.16) is derived by demonstration from the expression for $O(t)$ in terms of real time propagators (eqns. 3.8, 3.12),

$$O(t) = \frac{Tr\{\hat{U}(t_0 - i\beta, t_0)\hat{U}(t_0, t)\hat{O}_t\hat{U}(t, t_0)\}}{Tr\{\hat{U}(t_0 - i\beta, t_0)\}}. \tag{A.1}$$

A.1 Multiple Propagator Form

First, the relation,

$$O(t) = \frac{Tr\{\hat{T}_C\left[\hat{U}_C(t_0 - i\beta, t_0)\hat{U}_C(t_0, t)\hat{O}_t\hat{U}_C(t, t_0)\}\right]}{Tr\{\hat{U}_C(t_0 - i\beta, t_0)\}}. \tag{A.2}$$

where the real-time operators $\hat{U}(t, t')$ have been replaced by complex contour propagators $\hat{U}_C(t, t')$. This is verified for the following two cases: first, when t is on the purely real branches of the KC, and second, when t is on the complex branch of the KC.

A.1.1 Real Branch

First, we assume that t is on the real branch of the KC. That is, t is a real time. It is apparent that, for t real and greater than or equal to t_0, $\hat{U}(t, t_0) = \hat{U}_C(t, t_0)$

in eqn. A.2 because the KC branch from $t0$ to t traverses the real time axis in the forward direction.

To show that $\hat{U}(t_0,t) = \hat{U}_C(t_0,t)$ is a little more complex. Noting that

$$
\begin{aligned}
\hat{U}(t_0,t) =& \hat{U}^\dagger(t,t_0) \\
=& \hat{1} + \sum_{n=1}^{\infty} \frac{(i)^n}{n!} \int_{t_0}^{t} dt_1 \cdots \int_{t_0}^{t} dt_n \times \\
& \left[\hat{T}\left[\hat{H}(t_1)\cdots\hat{H}(t_n)\right]\right]^\dagger \\
=& \hat{1} + \sum_{n=1}^{\infty} \frac{(i)^n}{n!} (-1) \int_{t}^{t_0} dt_1 \cdots (-1) \int_{t}^{t_0} dt_n \times \\
& \sum_P \Theta(t_{P(1)} - t_{P(2)})\Theta(t_{P(2)} - t_{P(3)}) \cdots \Theta(t_{P(n-1)} - t_{P(n)}) \times \\
& \left[\hat{H}_{P(1)}(t_{P(1)}) \cdots \hat{H}_{P(n)}(t_{P(n)})\right]^\dagger \\
=& \hat{1} + \sum_{n=1}^{\infty} \frac{(-i)^n}{n!} \int_{t}^{t_0} dt_1 \cdots \int_{t}^{t_0} dt_n \times \\
& \sum_P \Theta(t_{P(1)} - t_{P(2)})\Theta(t_{P(2)} - t_{P(3)}) \cdots \Theta(t_{P(n-1)} - t_{P(n)}) \times \\
& \hat{H}_{P(n)}(t_{P(n)}) \cdots \hat{H}_{P(1)}(t_{P(1)}) \\
=& \hat{1} + \sum_{n=1}^{\infty} \frac{(-i)^n}{n!} \int_{t}^{t_0} dt_1 \cdots \int_{t}^{t_0} dt_n \hat{T}_r \left[\hat{H}(t_1)\cdots\hat{H}(t_n)\right]
\end{aligned}
\tag{A.3}
$$

Note that the effect of the conjugate transpose reversed both the limits of integration as well as the order of the Hamiltonians, creating an effective reverse time ordering operator, $\hat{T}_r$. Unlike $\hat{T}$, $\hat{T}_r$ orders the operators in chronological order from left to right. Thus, the integration limits and $\hat{T}_r$ is coincident with the the $t \to t_0$ branch of the KC and its direction. As a result, $\hat{U}(t_0,t)$ can be replaced by $\hat{U}_C(t_0,t)$ here as well.

A.1.2 Complex Branch

Now, we assume that t is on the complex branch of the KC. That is, $t = t_0 - i\tau$ where $0 \leq \tau \leq \beta$. Note that, when the complex time is $t_0 - i\tau$, the real time is t_0 and the real propagators become $\hat{U}(t_0, t_0) = \hat{1}$, converting eqn. A.1 into the stationary ensemble average of the operator $\hat{O}$, as expected.

$$O(t) = \frac{Tr\{\hat{\rho}_\circ \hat{O}\}}{Tr\{\hat{U}_C(t_0 - i\beta, t_0)\}}. \tag{A.4}$$

This relation is preserved, when $\hat{U}$ is replaced by $\hat{U}_C$, as shown below.

$$\begin{aligned}
O(t) =& \frac{Tr\{\hat{T}_C \left[\hat{U}_C(t_0 - i\beta, t_0)\hat{U}_C(t_0, t_0 - i\tau)\hat{O}_{t_0 - i\tau}\hat{U}_C(t_0 - i\tau, t_0)\right]\}}{Tr\{\hat{U}_C(t_0 - i\beta, t_0)\}} \\
=& \frac{Tr\{\hat{T}_C \left[\hat{U}_C(t_0 - i\beta, t_0)\hat{O}_{t_0 - i\tau}\hat{U}_C(t_0, t_0 - i\tau)\hat{U}_C(t_0 - i\tau, t_0)\right]\}}{Tr\{\hat{U}_C(t_0 - i\beta, t_0)\}} \\
=& \frac{Tr\{\hat{T}_C \left[\hat{U}_C(t_0 - i\beta, t_0 - i\tau)\hat{U}_C(t_0 - i\tau, t_0)\hat{O}_{t_0 - i\tau}\right]\}}{Tr\{\hat{U}_C(t_0 - i\beta, t_0)\}} \\
=& \frac{Tr\{\hat{U}_C(t_0 - i\beta, t_0 - i\tau)\hat{O}_{t_0 - i\tau}\hat{U}_C(t_0 - i\tau, t_0)\}}{Tr\{\hat{U}_C(t_0 - i\beta, t_0)\}} \\
=& \frac{Tr\{\hat{U}_C(t_0 - i\tau, t_0)\hat{U}_C(t_0 - i\beta, t_0 - i\tau)\hat{O}_{t_0 - i\tau}\}}{Tr\{\hat{U}_C(t_0 - i\beta, t_0)\}} \\
=& \frac{Tr\{\hat{U}_C(t_0 - i\beta, t_0 - i\tau)\hat{U}_C(t_0 - i\tau, t_0)\hat{O}_{t_0 - i\tau}\}}{Tr\{\hat{U}_C(t_0 - i\beta, t_0)\}} \\
=& \frac{Tr\{\hat{U}_C(t_0 - i\beta, t_0)\hat{O}_{t_0 - i\tau}\}}{Tr\{\hat{U}_C(t_0 - i\beta, t_0)\}} \\
=& \frac{Tr\{\hat{\rho}_\circ \hat{O}\}}{Tr\{\hat{\rho}_\circ\}}
\end{aligned} \tag{A.5}$$

A.2 Single Propagator Form

In this section, the relation (eqn. 3.15),

$$O(t) = \frac{Tr\{\hat{T}_C \left[e^{-i\int_C dt_1 (\hat{H}(t_1) - \mu\hat{N})}\hat{O}_t\right]\}}{Tr\{\hat{U}(t_0 - i\beta, t_0)\}}. \tag{A.6}$$

is verified.

A.2.1 Simple Demonstration

For visual ease, this is demonstrated with the first two terms of the expansion eqn. 3.8,

$$\hat{U}(t,t') = \hat{1} - i\int_{t'}^{t} dt_1 \hat{H}(t_1) + ... \tag{A.7}$$

for the Heisenberg operator $\hat{U}(t_0,t)\hat{O}_t\hat{U}(t,t_0)$.

$$\begin{aligned}
&\hat{U}(t_0,t)\hat{O}_t\hat{U}(t,t_0) = \\
&\qquad \left(\hat{1} - i\int_{t}^{t_0} dt_1 \hat{H}(t_1) + ...\right)\hat{O}_t\left(\hat{1} - i\int_{t_0}^{t} dt_2 \hat{H}(t_2) + ...\right) \\
&= \hat{O}_t - i\int_{t}^{t_0} dt_1 \hat{H}(t_1)\hat{O}_t - i\int_{t_0}^{t} dt_2 \hat{O}_t\hat{H}(t_2) \\
&\quad - \int_{t}^{t_0} dt_1 \int_{t_0}^{t} dt_2 \hat{H}(t_1)\hat{O}_t\hat{H}(t_2) + ...
\end{aligned} \tag{A.8}$$

The integral $\int_{t_0}^{t} dt_2$ comes before the application of $\hat{O}_t$ while the integral $\int_{t}^{t_0} dt_1$ is performed afterward. For this reason, the forward (t_2) and reverse (t_1) integrals will not, in general, cancel each other. Thus, each of these real-time integrals can be replaced by a KC integral where only the branch corresponding to the appropriate real-time region is counted. That is, $\int_{t}^{t_0} dt_1 \rightarrow \int_C dt_1 \Theta_C(t_1,t)$ and $\int_{t_0}^{t} dt_2 \rightarrow \int_C dt_1 \Theta_C(t,t_2)$. This gives,

$$\begin{aligned}
&\hat{O}_t - i\int_{t}^{t_0} dt_1 \hat{H}(t_1)\hat{O}_t - i\int_{t_0}^{t} dt_2 \hat{O}_t\hat{H}(t_2) \\
&\quad - \int_{t}^{t_0} dt_1 \int_{t_0}^{t} dt_2 \hat{H}(t_1)\hat{O}_t\hat{H}(t_2) + ... \\
&= \hat{O}_t - i\int_C dt_1 \left[\Theta_C(t_1,t)\hat{H}(t_1)\hat{O}_t + \Theta_C(t,t_1)\hat{O}_t\hat{H}(t_1)\right] \\
&\quad - \int_C dt_1 \int_C dt_1 \Theta_C(t_1,t)\Theta_C(t,t_2)\hat{H}(t_1)\hat{O}_t\hat{H}(t_2) + ... \\
&= \hat{O}_t - i\int_C dt_1 \hat{T}_C\left[\hat{H}(t_1)\hat{O}_t\right] \\
&\quad - \int_C dt_1 \int_C dt_2 \Theta_C(t_1,t)\Theta_C(t,t_2)\hat{H}(t_1)\hat{O}_t\hat{H}(t_2) + ...
\end{aligned} \tag{A.9}$$

In order to deal with the last term on the right hand side of eqn. A.9, two additional terms from the remainder of the expansion are used,

(A.10)

$$
\begin{aligned}
\hat{O}_t - i\int_C dt_1 \hat{T}_C\left[\hat{H}(t_1)\hat{O}_t\right] & \\
&- \int_C dt_1 \int_C dt_2 \Theta_C(t_1,t)\Theta_C(t,t_2)\hat{H}(t_1)\hat{O}_t\hat{H}(t_2) \\
&- \frac{1}{2}\int_t^{t_0} dt_1 \int_t^{t_0} dt_2 \hat{T}_r\left[\hat{H}(t_1)\hat{H}(t_2)\right]\hat{O}_t \\
&- \frac{1}{2}\int_{t_0}^{t} dt_1 \int_{t_0}^{t} dt_2 \hat{T}\hat{O}_t\left[\hat{H}(t_1)\hat{H}(t_2)\right] + ... \\
&= \hat{O}_t - i\int_C dt_1 \hat{T}_C\left[\hat{H}(t_1)\hat{O}_t\right] \\
&- \frac{1}{2}\int_C dt_1 \int_C dt_2 \left[\Theta_C(t_1,t)\Theta_C(t,t_2)\hat{H}(t_1)\hat{O}_t\hat{H}(t_2) - \Theta_C(t_2,t)\Theta_C(t,t_1)\hat{H}(t_2)\hat{O}_t\hat{H}(t_1)\right] \\
&- \frac{1}{2}\int_t^{t_0} dt_1 \int_t^{t_0} dt_2 \left[\Theta(t_1-t_2)\hat{H}(t_2)\hat{H}(t_1) - \Theta(t_2-t_1)\hat{H}(t_1)\hat{H}(t_2)\right]\hat{O}_t \\
&- \frac{1}{2}\int_{t_0}^{t} dt_1 \int_{t_0}^{t} dt_2 \hat{O}_t\left[\Theta(t_1-t_2)\hat{H}(t_1)\hat{H}(t_2) - \Theta(t_2-t_1)\hat{H}(t_2)\hat{H}(t_1)\right] + ... \\
&= \hat{O}_t - i\int_C dt_1 \hat{T}_C\left[\hat{H}(t_1)\hat{O}_t\right] \\
&- \frac{1}{2}\int_C dt_1 \int_C dt_2 \times \\
&[\Theta_C(t_1,t)\Theta_C(t,t_2)\hat{H}(t_1)\hat{O}_t\hat{H}(t_2) - \Theta_C(t_2,t)\Theta_C(t,t_1)\hat{H}(t_2)\hat{O}_t\hat{H}(t_1) \\
&\Theta_C(t_1,t_2)\Theta_C(t_2,t)\hat{H}(t_1)\hat{H}(t_2)\hat{O}_t - \Theta_C(t_2,t_1)\Theta_C(t_1,t)\hat{H}(t_2)\hat{H}(t_1)\hat{O}_t \\
&\Theta_C(t,t_1)\Theta_C(t_1,t_2)\hat{O}_t\hat{H}(t_1)\hat{H}(t_2) - \Theta_C(t,t_2)\Theta_C(t_2,t_1)\hat{O}_t\hat{H}(t_2)\hat{H}(t_1)] + ... \\
&= \hat{O}_t - i\int_C dt_1 \hat{T}_C\left[\hat{H}(t_1)\hat{O}_t\right] \\
&- \frac{1}{2}\int_C dt_1 \int_C dt_2 \hat{T}_C\left[\hat{H}(t_1)\hat{H}(t_2)\hat{O}_t\right] + ...
\end{aligned}
$$

This demonstrates eqn. A.6 when t is on the real branches of the KC. To include the possibility of complex t, $\hat{U}(t_0 - i\beta, t_0)$ is combined with this expression in the manner described above to give eqn. A.6.

A.2.2 General Derivation

A more general derivation of eqn. A.6, analogous to the one in the previous section, is presented here. As before, the Heisenberg representation of $\hat{O}$ is investigated,

$$\begin{aligned}
&\hat{U}(t_0,t)\hat{O}_t\hat{U}(t,t_0) = \\
&\quad \left(\hat{T}_r\left[e^{-i\int_t^{t_0} dt_1\left(\hat{H}(t_1)-\mu\hat{N}\right)}\right]\right)\hat{O}_t\left(\hat{T}\left[e^{-i\int_{t_0}^{t} dt_1'\left(\hat{H}(t_1')-\mu\hat{N}\right)}\right]\right) \\
&\quad = \left(\hat{1}+\sum_{m=1}^{\infty}\frac{(-i)^m}{m!}\int_t^{t_0}dt_1\cdots\int_t^{t_0}dt_m\hat{T}_r\left[\hat{H}(t_1)\cdots\hat{H}(t_m)\right]\right)\hat{O}_t\times \\
&\quad \left(\hat{1}+\sum_{n=1}^{\infty}\frac{(-i)^n}{n!}\int_{t_0}^{t}dt_1'\cdots\int_{t_0}^{t}dt_n'\hat{T}\left[\hat{H}(t_1')\cdots\hat{H}(t_n')\right]\right)
\end{aligned} \tag{A.11}$$

The sums in the last part of eqn. A.11 can be reordered so that each term in the sequence has the same total number of Hamiltonians,

$$\begin{aligned}
&\hat{U}(t_0,t)\hat{O}_t\hat{U}(t,t_0) = \\
&\quad \sum_{j=0}^{\infty}\sum_{m,n\geq 0;m+n=j}\frac{(-i)^{m+n}}{m!n!}\int_t^{t_0}dt_1\cdots\int_t^{t_0}dt_m\int_{t_0}^{t}dt_1'\cdots\int_{t_0}^{t}dt_n'\times \\
&\quad \hat{T}_r\left[\hat{H}(t_1)\cdots\hat{H}(t_m)\right]\hat{O}_t\hat{T}\left[\hat{H}(t_1')\cdots\hat{H}(t_n')\right] \\
&= \sum_{j=0}^{\infty}\sum_{m,n\geq 0;m+n=j}\frac{(-i)^{m+n}}{m!n!}\int_t^{t_0}dt_1\cdots\int_t^{t_0}dt_m\int_{t_0}^{t}dt_1'\cdots\int_{t_0}^{t}dt_n'\times \\
&\quad \sum_P\Theta(t_{P(1)}-t_{P(2)})\Theta(t_{P(2)}-t_{P(3)})\cdots\Theta(t_{P(n-1)}-t_{P(n)})\times \\
&\quad \hat{H}_{P(m)}(t_{P(m)})\cdots\hat{H}_{P(1)}(t_{P(1)})\times\hat{O}_t\times \\
&\quad \sum_P{}'\Theta(t_{P'(1)}-t_{P'(2)})\Theta(t_{P'(2)}-t_{P'(3)})\cdots\Theta(t_{P'(n-1)}-t_{P'(n)})\times \\
&\quad \hat{H}_{P'(1)}(t_{P'(1)})\cdots\hat{H}_{P'(n)}(t_{P'(n)})
\end{aligned} \tag{A.12}$$

where $m = 0$ implies that there are no Hamiltonians on the left side of $\hat{O}_t$ and, likewise, $n = 0$ implies that there are no Hamiltonians to the right of $\hat{O}_t$. The ordering of the operators indicates that the real time ordering operators, $\hat{T}_r$ and $\hat{T}$ can be replaced by a contour ordering operator $\hat{T}_C$. However, the combinatoric

coefficient must be calculated correctly. The explicit expressions for $\hat{T}_r$ and $\hat{T}$ in eqn. A.12 both sum over all permutations of the operators being ordered. This implies that every possible rearrangement of Hamiltonians to the left (and likewise, to the right) of $\hat{O}_t$ has been accounted for. To allow for a global application of $\hat{T}_C$, all possible permutations must be allowed. Since the order of the m Hamiltonians on the left (or n Hamiltonians on the right) of $\hat{O}_t$ is already accounted for, the missing factor must only account for the number of ways that one can choose m Hamiltonians on the left (or conversely n Hamiltonians on the right) from the total number number of Hamiltonians, $m+n$. From combinatorics, this number is given by $(m+n)!/(m!n!)$ and the sum constrained by $(m+n=j)$ eqn. (A.12) can be rewritten, giving

$$\begin{aligned}
&\hat{U}(t_0,t)\hat{O}_t\hat{U}(t,t_0) = \\
&\qquad \sum_{j=0}^{\infty} \sum_{m,n\geq 0; m+n=j} \frac{(-i)^{m+n}}{m!n!} \frac{m!n!}{(m+n)!} \int_{C'} dt_1 \cdots \int_{C'} dt_{m+n} \times \\
&\qquad \sum_{P} \Theta_C(t_{P(1)}, t_{P(2)}) \Theta(t_{P(2)}, t_{P(3)}) \cdots \Theta(t_{P(m+n-1)}, t_{P(m+n)}) \times \\
&\qquad \hat{H}_{P(1)}(t_{P(1)}) \cdots \hat{O}_t \cdots \hat{H}_{P(m+n)}(t_{P(m+n)}) \\
&\qquad = \sum_{j=0}^{\infty} \frac{(-i)^j}{j!} \int_{C'} dt_1 \cdots \int_{C'} dt_j \hat{T}_C \left[\hat{H}_{P(1)}(t_{P(1)}) \cdots \hat{H}_{P(j)}(t_{P(j)}) \hat{O}_t \right]
\end{aligned} \tag{A.13}$$

where C' includes the branches of the KC where t is real. As in the previous section, $\hat{U}(t_0 - i\beta, t_0)$ is combined with this expression in a similar manner to give eqn. A.6.

APPENDIX B

Derivation of the Quantum Master Equation for Open Systems

We begin with the mixed representation equation of motion of the full system (eq. 6.2):

$$\text{(B.1)}\quad \frac{\partial}{\partial \bar{t}}\mathbf{G}^{<}(\bar{t},\bar{\omega}) = i\,[\mathbf{G}^{<}(\bar{t},\bar{\omega}),\mathbf{h}_0] + i\int d\omega'[\mathbf{G}^{<}(\bar{t},\bar{\omega}+\omega')\bar{\mathbf{v}}(\bar{t},\omega') - \bar{\mathbf{v}}(\bar{t},\omega')\mathbf{G}^{<}(\bar{t},\bar{\omega}-\omega')].$$

where $\mathbf{h}_0 = \mathbf{S}^{-1/2}\tilde{\mathbf{h}}_0\mathbf{S}^{-1/2}$, $\bar{\mathbf{v}}(\bar{t},\omega') = \mathbf{S}^{-1/2}\tilde{\bar{\mathbf{v}}}(\bar{t},\omega')\mathbf{S}^{-1/2}$ and $\mathbf{G}^{<}(\bar{t},\bar{\omega}) = \mathbf{S}^{1/2}\tilde{\mathbf{G}}^{<}(\bar{t},\bar{\omega})\mathbf{S}^{1/2}$. Here $\tilde{\mathbf{h}}_0$, $\tilde{\bar{\mathbf{v}}}(\bar{t},\omega')$ and $\tilde{\mathbf{G}}^{<}(\bar{t},\bar{\omega})$ are in the AO representation and $\mathbf{S}$ is the AO overlap matrix. We note that eqn. B.1 applies to a system that is infinite in extent. Our goal is to derive an appropriate mixed-representation equation of motion for a finite system under the influence of infinite baths. We will do this by partitioning our system into a device region and two bulk regions.

$$\text{(B.2)}\qquad \tilde{\mathbf{h}}_0 = \begin{bmatrix} \tilde{\mathbf{h}}_{0LL} & \tilde{\mathbf{h}}_{0LC} & 0 \\ \tilde{\mathbf{h}}_{0CL} & \tilde{\mathbf{h}}_{0CC} & \tilde{\mathbf{h}}_{0CR} \\ 0 & \tilde{\mathbf{h}}_{0RC} & \tilde{\mathbf{h}}_{0RR} \end{bmatrix}$$

$$\text{(B.3)}\qquad \tilde{\mathbf{S}} = \begin{bmatrix} \tilde{\mathbf{S}}_{LL} & 0 & 0 \\ 0 & \tilde{\mathbf{S}}_{CC} & 0 \\ 0 & 0 & \tilde{\mathbf{S}}_{RR} \end{bmatrix}$$

$$\tilde{\bar{\mathbf{v}}}(t,\omega) = \begin{bmatrix} 0 & 0 & 0 \\ 0 & \tilde{\bar{\mathbf{v}}}_{CC}(t,\omega) & 0 \\ 0 & 0 & 0 \end{bmatrix} \tag{B.4}$$

$$\tilde{\mathbf{G}}^{<}(\bar{t},\bar{\omega}) = \begin{bmatrix} \tilde{\mathbf{G}}^{<}_{LL}(\bar{t},\bar{\omega}) & \tilde{\mathbf{G}}^{<}_{LC}(\bar{t},\bar{\omega}) & 0 \\ \tilde{\mathbf{G}}^{<}_{CL}(\bar{t},\bar{\omega}) & \tilde{\mathbf{G}}^{<}_{CC}(\bar{t},\bar{\omega}) & \tilde{\mathbf{G}}^{<}_{CR}(\bar{t},\bar{\omega}) \\ 0 & \tilde{\mathbf{G}}^{<}_{RC}(\bar{t},\bar{\omega}) & \tilde{\mathbf{G}}^{<}_{RR}(\bar{t},\bar{\omega}) \end{bmatrix} \tag{B.5}$$

Note that we make the following two important assumptions: first the system-bulk coupling overlap submatrices ($\mathbf{S}_{LC}$, $\mathbf{S}_{RC}$, etc.) are zero; second, the TD perturbation is nonzero only in the device (CC) region. This derivation will lead to a generalized quantum master equation (GQME) with memory terms that resemble the weak system bath coupling memory kernel for the density matrix GQME. Partitioning yields the following equations of motion:

$$\begin{aligned} i\frac{\partial}{\partial \bar{t}}\mathbf{G}^{<}_{CC}(\bar{t},\bar{\omega}) &= [\mathbf{h}_{0CC}, \mathbf{G}^{<}_{CC}(\bar{t},\bar{\omega})] \\ &+ \sum_{I\in L,R} [\mathbf{h}_{CI}\mathbf{G}^{<}_{IC}(\bar{t},\bar{\omega}) - \mathbf{G}^{<}_{CI}(\bar{t},\bar{\omega})\mathbf{h}_{IC}] \\ &+ \int d\omega' [\bar{\mathbf{v}}_{CC}(\bar{t},\omega')\mathbf{G}^{<}_{CC}(\bar{t},\bar{\omega}-\omega') - \mathbf{G}^{<}_{CC}(\bar{t},\bar{\omega}+\omega')\bar{\mathbf{v}}_{CC}(\bar{t},\omega')]. \end{aligned} \tag{B.6}$$

$$\begin{aligned} i\frac{\partial}{\partial \bar{t}}\mathbf{G}^{<}_{IC}(\bar{t},\bar{\omega}) &= \mathbf{h}_{0II}\mathbf{G}^{<}_{IC}(\bar{t},\bar{\omega}) + \mathbf{h}_{0IC}\mathbf{G}^{<}_{CC}(\bar{t},\bar{\omega}) \\ &- \mathbf{G}^{<}_{II}(\bar{t},\bar{\omega})\mathbf{h}_{0IC} - \mathbf{G}^{<}_{IC}(\bar{t},\bar{\omega})\mathbf{h}_{0CC} \\ &- \int d\omega' [\mathbf{G}^{<}_{IC}(\bar{t},\bar{\omega}+\omega')\bar{\mathbf{v}}_{CC}(\bar{t},\omega')]. \end{aligned} \tag{B.7}$$

where $I \in L, R$. Furthermore, given the assumptions made on the overlap matrix, we have $\bar{\mathbf{v}}_{CC}(\bar{t},\omega') = \mathbf{S}^{-1/2}_{CC}\tilde{\bar{\mathbf{v}}}_{CC}(\bar{t},\omega')\mathbf{S}^{-1/2}_{CC}$, $\mathbf{h}_{0IJ} = \mathbf{S}^{-1/2}_{II}\tilde{\mathbf{h}}_{0IJ}\mathbf{S}^{-1/2}_{JJ}$ and $\mathbf{G}^{<}_{IJ}(\bar{t},\bar{\omega}) = \mathbf{S}^{1/2}_{II}\tilde{\mathbf{G}}^{<}_{IJ}(\bar{t},\bar{\omega})\mathbf{S}^{1/2}_{JJ}$ for $I, J \in L, C, R$. In addition, we will assume that the last term in eqn. B.7 is negligible. In studying large chemical systems in the AO representation,

this can easily be achieved by extending the dimension of the device beyond the spatial extent of the perturbation (assuming that the perturbation is finite in spatial extent). We now divide the lesser GF into a sum of two parts, as follows,

$$\mathbf{G}^{<}(\bar{t},\bar{\omega}) \equiv \mathbf{G}^{0,<}(\bar{\omega}) + \mathbf{\Delta G}^{<}(\bar{t},\bar{\omega}) \tag{B.8}$$

where $\mathbf{G}^{0,<}(\bar{\omega})$ is the lesser GF in the absence of a TD perturbation (i.e. Hamiltonian is constant in time) and $\mathbf{\Delta G}^{<}(\bar{t},\bar{\omega})$ is the remainder (i.e. the part that carries all perturbation effects). Note that we do not claim that $\mathbf{G}^{0,<}(\bar{\omega})$ is the lesser GF at $\bar{t} = t_0 \to -\infty$. It is merely the contribution to the GF in the absence of a time dependent perturbation. Note furthermore, that $\mathbf{G}^{0,<}(\bar{\omega})$ does not depend on $\bar{t}$ by definition of the Green function. This implies that

$$\frac{\partial}{\partial \bar{t}}\mathbf{G}^{0,<}(\bar{\omega}) = 0 \tag{B.9}$$

and therefore,

$$\frac{\partial}{\partial \bar{t}}\mathbf{G}^{<}(\bar{t},\bar{\omega}) = \frac{\partial}{\partial \bar{t}}\mathbf{\Delta G}^{<}(\bar{t},\bar{\omega}) \tag{B.10}$$

Using these properties and the approximations above, we can rewrite eqns. B.6 and B.7 in terms of $\mathbf{\Delta G}^{<}(\bar{t},\bar{\omega})$.

$$\begin{aligned} i\frac{\partial}{\partial t}\mathbf{\Delta G}^{<}_{CC}(\bar{t},\bar{\omega}) &= [\mathbf{h}_{0CC}, \mathbf{\Delta G}^{<}_{CC}(\bar{t},\bar{\omega})] \\ &+ \sum_{I\in L,R}[\mathbf{h}_{CI}\mathbf{\Delta G}^{<}_{IC}(\bar{t},\bar{\omega}) - \mathbf{\Delta G}^{<}_{CI}(\bar{t},\bar{\omega})\mathbf{h}_{IC}] \\ &+ \int d\omega'[\bar{\mathbf{v}}_{CC}(\bar{t},\omega')\mathbf{G}^{0,<}_{CC}(\bar{\omega}-\omega') - \mathbf{G}^{0,<}_{CC}(\bar{\omega}+\omega')\bar{\mathbf{v}}_{CC}(\bar{t},\omega')] \\ &+ \int d\omega'[\bar{\mathbf{v}}_{CC}(\bar{t},\omega')\mathbf{\Delta G}^{<}_{CC}(\bar{t},\bar{\omega}-\omega') - \mathbf{\Delta G}^{<}_{CC}(\bar{t},\bar{\omega}+\omega')\bar{\mathbf{v}}_{CC}(\bar{t},\omega')] \end{aligned} \tag{B.11}$$

$$i\frac{\partial}{\partial \bar{t}}\mathbf{\Delta G}^{<}_{IC}(\bar{t},\bar{\omega}) = \mathbf{h}_{0II}\mathbf{\Delta G}^{<}_{IC}(\bar{t},\bar{\omega}) - \mathbf{\Delta G}^{<}_{IC}(\bar{t},\bar{\omega})\mathbf{h}_{0CC} + \mathbf{h}_{0IC}\mathbf{\Delta G}^{<}_{CC}(\bar{t},\bar{\omega}) \tag{B.12}$$

We can integrate these equations as suggested in the formalism by redefining $\mathbf{\Delta G}^{<}_{IC}(\bar{t},\bar{\omega})$ as follows:

$$\mathbf{\Delta G}^{<}_{IC}(\bar{t},\bar{\omega}) \equiv \mathbf{e}^{-i\mathbf{h}_{0II}(\bar{t}-t_0)}\mathbf{\Delta \mathcal{G}}^{<}_{IC}(\bar{t},\bar{\omega})\mathbf{e}^{i\mathbf{h}_{0CC}(\bar{t}-t_0)}. \tag{B.13}$$

Upon substitution of definition eqn. B.13 into eqn. B.12 we get,

APPENDIX C

Derivation of Two-Frequency Equation of Motion with Exact Treatment of Steady State Bias

A derivation of eqn. 6.35 is presented here. We start with the general two-frequency equation of motion (eqn. 6.23),

$$\begin{aligned}\mathbf{H}(\Delta\omega)|\boldsymbol{\Delta G}^{<}_{CC}(\Delta\omega,\bar{\omega})\rangle\rangle = \\ |B^{(1)}_{CC}(\Delta\omega,\bar{\omega})\rangle\rangle \\ +\frac{1}{\pi}\int d\omega' |B_{CC}(\omega',\Delta\omega,\bar{\omega})\rangle\rangle\end{aligned} \tag{C.1}$$

and the frequency representation of a classical driving field, expressed, without loss of generality, as a sum of the time independent field of arbitrary strength $v_\circ$ and a time dependent perturbation v_{TD} (eqn. 6.34),

$$\mathbf{v}(\Delta\omega) = 2\pi\delta(\Delta\omega)\mathbf{v}_\circ + \mathbf{v}_{TD}(\Delta\omega). \tag{C.2}$$

Substituting eqn. C.2 into eqn. C.1 gives,

$$\begin{aligned}\mathbf{H}(\Delta\omega)|\boldsymbol{\Delta G}^{<}_{CC}(\Delta\omega,\bar{\omega})\rangle\rangle = \\ 2\pi\delta(\Delta\omega)|B^{(1)}_{v_\circ,CC}(\bar{\omega})\rangle\rangle \\ +\mathbf{V}_\circ|\boldsymbol{\Delta G}^{<}_{CC}(\Delta\omega,\bar{\omega})\rangle\rangle \\ +|B^{(1)}_{TD,CC}(\Delta\omega,\bar{\omega})\rangle\rangle \\ +\frac{1}{\pi}\int d\omega' |B_{TD,CC}(\omega',\Delta\omega,\bar{\omega})\rangle\rangle\end{aligned} \tag{C.3}$$

where $\mathbf{V}_\circ$ is the time-independent driving field in tetradic notation,

$$\mathbf{V}_{\circ,ni+j,nk+l} \equiv v_{\circ,ik}\delta_{lj} - v_{\circ,lj}\delta_{ik} \tag{C.4}$$

and $|B^{(1)}_{v_\circ,CC}(\bar{\omega})\rangle\rangle$, $|B^{(1)}_{TD,CC}(\Delta\omega,\bar{\omega})\rangle\rangle$, and $|B_{TD,CC}(\omega',\Delta\omega,\bar{\omega})\rangle\rangle$ are defined as follows,

$$|B^{(1)}_{v_\circ,CC}(\bar{\omega})\rangle\rangle_{ni+j} \equiv \left[\mathbf{v}_{\circ,CC}\mathbf{G}^{0,<}_{CC}(\bar{\omega}) - \mathbf{G}^{0,<}_{CC}(\bar{\omega})\mathbf{v}_{\circ,CC}\right]_{ij}. \tag{C.5}$$

(C.6)

$$|B^{(1)}_{TD,CC}(\Delta\omega,\bar{\omega})\rangle\rangle_{ni+j} \equiv \left[\mathbf{v}_{TD,CC}(\Delta\omega)\mathbf{G}^{0,<}_{CC}(\bar{\omega}-\Delta\omega/2) - \mathbf{G}^{0,<}_{CC}(\bar{\omega}+\Delta\omega/2)\mathbf{v}_{TD,CC}(\Delta\omega)\right]_{ij}$$

(C.7)

$$|B_{TD,CC}(\omega',\Delta\omega,\bar{\omega})\rangle\rangle_{ni+j} \equiv$$

$$[\mathbf{v}_{TD,CC}(2\omega')\boldsymbol{\Delta G}^{<}_{CC}(\Delta\omega-2\omega',\bar{\omega}-\omega') - \boldsymbol{\Delta G}^{<}_{CC}(\Delta\omega-2\omega',\bar{\omega}+\omega')\mathbf{v}_{TD,CC}(2\omega')]_{ij}$$

The second term on the right side of eq. C.3 is the contribution of $2\pi\delta(\Delta\omega)\mathbf{v}_\circ$ to the second term on the right hand side of eqn. C.1. This term can be moved to the left hand side of eqn. C.3 giving,

$$\begin{aligned}\mathbf{H}_{v_\circ}(\Delta\omega)|\boldsymbol{\Delta G}^{<}_{CC}(\Delta\omega,\bar{\omega})\rangle\rangle = \\ 2\pi\delta(\Delta\omega)|B^{(1)}_{v_\circ,CC}(\bar{\omega})\rangle\rangle \\ +|B^{(1)}_{TD,CC}(\Delta\omega,\bar{\omega})\rangle\rangle \\ +\frac{1}{\pi}\int d\omega'|B_{TD,CC}(\omega',\Delta\omega,\bar{\omega})\rangle\rangle\end{aligned} \tag{C.8}$$

where $\mathbf{H}_{v_\circ}(\Delta\omega) \equiv \mathbf{H}(\Delta\omega) - \mathbf{V}_\circ(\Delta\omega)$ simply adds the time-independent driving field to the original Hamiltonian,

$$\mathbf{H}_{v_\circ,ni+j,nk+l}(\Delta\omega) \equiv \Delta\omega - [(\epsilon_i\delta_{ik} + v_{ik})\,\delta_{lj} - (\epsilon_j\delta_{lj} + v_{lj})\,\delta_{ik}] - \Gamma_{ijkl}(\Delta\omega). \tag{C.9}$$

Now, we multiply both sides of eqn. C.8 by $\mathbf{G}_{v_\circ}(\Delta\omega) = \mathbf{H}_{v_\circ}^{-1}(\Delta\omega)$ giving,

$$
\begin{aligned}
|\boldsymbol{\Delta G}^{<}_{CC}(\Delta\omega,\bar{\omega})\rangle\rangle = \\
2\pi\delta(\Delta\omega)\mathbf{G}_{v_\circ}(0)|B^{(1)}_{v_\circ,CC}(\bar{\omega})\rangle\rangle \\
+\mathbf{G}_{v_\circ}(\Delta\omega)|B^{(1)}_{TD,CC}(\Delta\omega,\bar{\omega})\rangle\rangle \\
+\frac{1}{\pi}\mathbf{G}_{v_\circ}(\Delta\omega)\int d\omega'|B_{TD,CC}(\omega',\Delta\omega,\bar{\omega})\rangle\rangle
\end{aligned}
\tag{C.10}
$$

The first term on the right side of eqn. C.10 can be absorbed into the left side with the following definition,

$$
|\boldsymbol{\Delta G}^{<}_{TD,CC}(\Delta\omega,\bar{\omega})\rangle\rangle \equiv |\boldsymbol{\Delta G}^{<}_{CC}(\Delta\omega,\bar{\omega})\rangle\rangle - 2\pi\delta(\Delta\omega)\mathbf{G}_{v_\circ}(0)|B^{(1)}_{v_\circ,CC}(\bar{\omega})\rangle\rangle \tag{C.11}
$$

yielding,

$$
\begin{aligned}
|\boldsymbol{\Delta G}^{<}_{TD,CC}(\Delta\omega,\bar{\omega})\rangle\rangle = \\
\mathbf{G}_{v_\circ}(\Delta\omega)|B^{(1)}_{TD,CC}(\Delta\omega,\bar{\omega})\rangle\rangle \\
+\frac{1}{\pi}\mathbf{G}_{v_\circ}(\Delta\omega)\int d\omega'|B_{TD,CC}(\omega',\Delta\omega,\bar{\omega})\rangle\rangle.
\end{aligned}
\tag{C.12}
$$

Substituting eqn. C.11 into the right side of eqn. C.12 gives

$$
\begin{aligned}
|\boldsymbol{\Delta G}^{<}_{TD,CC}(\Delta\omega,\bar{\omega})\rangle\rangle = \\
\mathbf{G}_{v_\circ}(\Delta\omega)|B^{(1)}_{TD,CC}\left[G_{v_\circ}\right](\Delta\omega,\bar{\omega})\rangle\rangle \\
+\frac{1}{\pi}\mathbf{G}_{v_\circ}(\Delta\omega)\int d\omega'|B_{TD,CC}\left[\Delta G_{v_\circ}\right](\omega',\Delta\omega,\bar{\omega})\rangle\rangle.
\end{aligned}
\tag{C.13}
$$

where,

(C.14)

$$
|B^{(1)}_{TD,CC}\left[G_{v_\circ}\right](\Delta\omega,\bar{\omega})\rangle\rangle_{ni+j} \equiv \left[\mathbf{v}_{TD,CC}(\Delta\omega)\mathbf{G}^{0,<}_{v_\circ,CC}(\bar{\omega}-\Delta\omega/2) - \mathbf{G}^{0,<}_{v_\circ,CC}(\bar{\omega}+\Delta\omega/2)\mathbf{v}_{TD,CC}(\Delta\omega)\right]_{ij}
$$

(C.15)

$$
\begin{aligned}
|B_{TD,CC}\left[\Delta G_{v_\circ}\right](\omega',\Delta\omega,\bar{\omega})\rangle\rangle_{ni+j} \equiv \\
\left[\mathbf{v}_{TD,CC}(2\omega')\boldsymbol{\Delta G}^{<}_{v_\circ,CC}(\Delta\omega-2\omega',\bar{\omega}-\omega') - \boldsymbol{\Delta G}^{<}_{v_\circ,CC}(\Delta\omega-2\omega',\bar{\omega}+\omega')\mathbf{v}_{TD,CC}(2\omega')\right]_{ij}
\end{aligned}
$$

and

$$|G^{0,<}_{v_\circ,CC}(\bar{\omega})\rangle\rangle \equiv |G^{0,<}_{CC}(\bar{\omega})\rangle\rangle + \mathbf{G}_{v_\circ}(0)|B^{(1)}_{v_\circ,CC}(\bar{\omega})\rangle\rangle. \tag{C.16}$$

Note that eqn. 6.35 has now been derived and is analogous to eqn. 6.23, but with a different propagator tensor ($\mathbf{G} \rightarrow \mathbf{G}_{v_\circ}$) and a different initial guess ($G^{0,<} \rightarrow G^{0,<}_{v_\circ}$). To verify that this is indeed the case, the equation for the total lesser GF must be expressible in terms of the new initial guess (eqn. C.16) and the new time dependent remainder, eqn. C.11 ideally, in a manner analogous to

$$\mathbf{G}^{<}_{CC}(\Delta\omega, \bar{\omega}) \equiv \boldsymbol{\Delta G}^{<}(\Delta\omega, \bar{\omega}) + 2\pi\delta(\Delta\omega)\mathbf{G}^{0,<}_{CC}(\bar{\omega}) \tag{C.17}$$

This can easily be verified by substituting eqn. C.11 into the above definition of the total lesser GF eqn. C.17. This substitution gives,

$$\mathbf{G}^{<}_{CC}(\Delta\omega, \bar{\omega}) = \boldsymbol{\Delta G}^{<}_{TD,CC}(\Delta\omega, \bar{\omega}) + 2\pi\delta(\Delta\omega)\mathbf{G}^{0,<}_{v_\circ,CC}(\bar{\omega}) \tag{C.18}$$

verifying this point.

BIBLIOGRAPHY

BIBLIOGRAPHY

[1] D. M. Adams, L. Brus, C. E. D. Chidsey, S. Creager, C. Creutz, C. R. Kagan, P. V. Kamat, M. Lieberman, S. Lindsay, R. A. Marcus, R. M. Metzger, M. E. Michel-Beyerle, J. R. Miller, M. D. Newton, D. R. Rolison, O. Sankey, K. S. Schanze, J. Yardley, and X. Y. Zhu. Charge transfer on the nanoscale: Current status. *J. Phys. Chem. B*, 107:6668–6697, 2003.

[2] A. Agarwal and D. Sen. Nonadiabatic charge pumping in a one-dimensional system of non-interacting electrons by an oscillating potential. *Physical Review B (Condensed Matter and Materials Physics)*, 76(23):235316, 2007.

[3] M. P. Anantram and S. Datta. Effect of phase breaking on the ac response of mesoscopic systems. *Phys. Rev. B*, 51:7632, 1995.

[4] L. Arrachea. Green-function approach to transport phenomena in quantum pumps. *Phys. Rev. B*, 72(12):125349, 2005.

[5] L. Arrachea, Carlos Naon, and Mariano Salvay. Quantum pump effect in one-dimensional systems of dirac fermions. *Phys. Rev. B*, 76:165401, 2007.

[6] Liliana Arrachea. Green-function approach to transport phenomena in quantum pumps. *Phys. Rev. B*, 72:125349, 2005.

[7] Liliana Arrachea. Symmetry and environment effects on rectification mechanisms in quantum pumps. *Phys. Rev. B*, 72:121306, 2005.

[8] Liliana Arrachea and Michael Moskalets. Relation between scattering-matrix and keldysh formalisms for quantum transport driven by time-periodic fields. *Phys. Rev. B*, 74(24):245322, 2006.

[9] R. Baer and D. Neuhauser. Ab initio electrical conductance of a molecular wire. *Int. J. Quant. Chem.*, 91:524–532, 2003.

[10] R. Baer and D. Neuhauser. Real-time linear response for time-dependent density-finctional theory. *J. Chem. Phys.*, 121:9803–9807, 2004.

[11] R. Baer, T. Seidman, S. Ilani, and D. Neuhauser. Ab initio study of the alternating current impedance of a molecular junction. *J. Chem. Phys.*, 120:3387–3396, 2004.

[12] P. F. Bagwell and T. P. Orlando. Landauer's conductance formula and its generalization to finite voltages. *Phys. Rev. B*, 40:1456–1464, 1989.

[13] G. Baym. Conservation laws and correlation functions. *Physical Review*, 124:287, 1961.

[14] G. Baym. Self-consistent approximations in many-body systems. *Physical Review*, 127:1391, 1962.

[15] A. D. Becke. *J. Chem. Phys.*, 98:1372, 1993.

[16] A. D. Becke. *J. Chem. Phys.*, 98:5648, 1993.

[17] Andrew P. Bonifas and Richard L. McCreery. In-situ optical absorbance spectroscopy of molecular layers in carbon based molecular electronic devices. *Chemistry of Materials*, 20(12):3849–3856, 2008.

[18] M. Bonitz. *Quantum Kinetic Theory*. Teubner, Stuttgart, 1998.

[19] M. Brandbyge, J. L. Mozos, P. Ordejon, J. Taylor, and K. Stokbro. Density-functional method for nonequilibrium electron transport. *Phys. Rev. B*, 65:165401, 2002.

[20] P. W. Brouwer. Scattering approach to parametric pumping. *Phys. Rev. B*, 58(16):R10135–R10138, 1998.

[21] P. W. Brouwer. Rectification of displacement currents in an adiabatic electron pump. *Phys. Rev. B*, 63(12):121303, 2001.

[22] Ph. Brune, C. Bruder, and H. Schoeller. Photon-assisted transport through ultrasmall quantum dots: Influence of intradot transitions. *Phys. Rev. B*, 56(8):4730–4736, Aug 1997.

[23] Kieron Burke, Roberto Car, and Ralph Gebauer. Density functional theory of the electrical conductivity of molecular devices. *Phys. Rev. Lett.*, 94:146803, 2005.

[24] N. Bushong, N. Sai, and M. Di Ventra. Approach to steady-state transport in nanoscale conductors. *Nano. Lett.*, 5:2569, 2005.

[25] Sébastien Camalet, Sigmund Kohler, and Peter Hänggi. Shot-noise control in ac-driven nanoscale conductors. *Phys. Rev. B*, 70(15):155326, Oct 2004.

[26] Sébastien Camalet, Jörg Lehmann, Sigmund Kohler, and Peter Hänggi. Current noise in ac-driven nanoscale conductors. *Phys. Rev. Lett.*, 90(21):210602, May 2003.

[27] F. Chen, J. Hihath, Z. Huang, X. Li, and Tao N. J. Measurement of single-molecule conductance. *Annu. Rev. Phys. Chem.*, 58:535–564, 2007.

[28] J. Chen, M. A. Reed, A. M. Rawlett, and J. M. Tour. Large on-off ratios and negative differential resistance in a molecular electronic device. *Science*, 286:1550–1552, 1999.

[29] C.-L. Cheng, J. S. Evans, and T. Van Voorhis. Simulating molecular conductance using real-time density functional theory. *Phys. Rev. B*, 74:155112, 2006.

[30] M. Cini. Time-dependent approach to electron transport through junctions: General theory and simple applications. *Phys. Rev. B*, 22:5887, 1980.

[31] C. P. Collier, G. Mattersteig, E. W. Wong, Y. Luo, K. Beverly, J. Sampaio, F. M. Raymo, J. F. Stoddart, and J. R. Heath. A [2]catenane-based solid state electronically reconfigurable switch. *Science*, 289:1172–1175, 2000.

[32] C. P. Collier, E. W. Wong, M Belohradsky, F. M. Raymo, J. F. Stoddart, P. J. Kuekes, R. S. Williams, and J. R. Heath. Electronically configurable molecular-based logic gates. *Science*, 285:391–394, 1999.

[33] P. G. Collins, M. S. Arnold, and P. Avouris. Engineering carbon nanotubes and nanotube circuits using electrical breakdown. *Science*, 292:706–709, 2001.

[34] X. D. Cui, A. Primak, X. Zarate, J. Tomfohr, O. F. Sankey, A. L. Moore, T. A. Moore, D. Gust, G. Harris, and S. M. Lindsay. Reproducible measurement of single-molecule conductivity. *Science*, 294:571–574, 2001.

[35] P. Damle, A. W. Ghosh, F. Zahid, and S. Datta. First-principles analysis of molecular conduction using quantum chemistry software. *Chem. Phys*, 171-187:225, 2002.

[36] P. S. Damle, A. W. Ghosh, and S. Datta. Unified description of molecular conduction: From molecules to metallic wires. *Phys. Rev. B*, 64:201403(R), 2001.

[37] S. Datta. *Electronic Transport in Mesoscopic Systems*. Cambridge University Press, New York, 1995.

[38] P.A. Derosa and J. M. Seminario. Electron transport through single molecules: Scattering treatment using density functional and green function theories. *J. Phys. Chem. B*, 105:471, 2001.

[39] A. Dhar and D. Sen. Nonequilibrium green's function formalism and the problem of bound states. *Phys. Rev. B*, 73:085119, 2006.

[40] M. Di Ventra, S. T. Pantelides, and N. D. Lang. First-principles calculation of transport properties of a molecular device. *Phys. Rev. Lett.*, 84:979–982, 2000.

[41] L. DiCarlo, C. M. Marcus, and J. S. Harris. Photocurrent, rectification, and magnetic field symmetry of induced current through quantum dots. *Phys. Rev. Lett.*, 91(24):246804, 2003.

[42] F. R. F. Fan, J. P. Yang, L. T. Cai, D. W. Price, S. M. Dirk, D. V. Kosynkin, Y. X. Yao, A. M. Rawlett, J. M. Tour, and A. J. Bard. Charge transport through self-assembled monolayers of compounds of interest in molecular electronics. *J.Amer.Chem.Soc.*, 124:5550–5560, 2002.

[43] F.-R.F. Fan, Y. Yao, L. Cai, L. Cheng, J.M. Tour, and A.J. Bard. Structure-dependent charge transport and storage in self-assembled monolayers of compounds of interest in molecular electronics: Effects of tip material, headgroup, and surface concentration. *Journal of the American Chemical Society*, 126(12):4035–4042, 2004.

[44] A. L. Fetter and J. D. Walecka. *Quantum Statistical Mechanics*. Dover, 2003.

[45] C. M. Fischer, M. Burghard, and S. Roth. Molecular rectification in organic quantum-wells. *Synth. Met.*, 71:1975–1976, 1995.

[46] Akira Fujiwara, Katsuhiko Nishiguchi, and Yukinori Ono. Nanoampere charge pump by single-electron ratchet using silicon nanowire metal-oxide-semiconductor field-effect transistor. *Applied Physics Letters*, 92(4):042102, 2008.

[47] N.P. Guisinger, M.E. Greene, R. Basu, A.S. Baluch, and M.C. Hersam. Room temperature negative differential resistance through individual organic molecules on silicon surfaces. *Nano. Lett.*, 4:55–59, 2004.

[48] K. Hirose and M. Tsukada. First-principles calculations of the electroic structure for bielectrode junction suystem under strong field and current. *Phys. Rev. B*, 51:5278, 1995.

[49] O. Hod, R. Baer, and E. Rabani. *J. Phys. Chem. B*, 108:14807, 2004.

[50] O. Hod, R. Baer, and E. Rabani. A parallel electromagnetic molecular logic gate. *J. Am. Chem. Soc.*, 127(6):1648–1649, 2005.

[51] O. Hod, E. Rabani, and R. Baer. Magnetoresistance devices based on single-walled carbon nanotubes. *J. Chem. Phys.*, 123:051103, 2005.

[52] O. Hod, E. Rabani, and R. Baer. Magnetoresistance of nanoscale molecular devices. *Acc. Chem. Res.*, 39(2):109–117, 2006.

[53] Y. Imry and R. Landauer. *Rev. Mod. Phys.*, 71:S306, 1999.

[54] Y. Imry and R. Landauer. Conductance viewed as transmission. *Rev. Mod. Phys.*, 71:S306–S312, 1999.

[55] Antti-Pekka Jauho, Ned S. Wingreen, and Yigal Meir. Time-dependent transport in interacting and noninteracting resonant-tunneling systems. *Phys. Rev. B*, 50(8):5528–5544, Aug 1994.

[56] C. Joachim, J. K. Gimzewski, and A. Aviram. Electronics using hybrid-molecular and monomolecular devices. *Nature*, 408:541–548, 2000.

[57] L. P. Kadanoff and G. Baym. *Quantum Statistical Mechanics*. Benjamin and Cummings, New York, 1962.

[58] B. J. Keay, S. Zeuner, S. J. Allen, K. D. Maranowski, A. C. Gossard, U. Bhattacharya, and M. J. W. Rodwell. Dynamic localization, absolute negative conductance, and stimulated, multiphoton emission in sequential resonant tunneling semiconductor superlattices. *Phys. Rev. Lett.*, 75(22):4102–4105, Nov 1995.

[59] L. Keldysh. Diagram technique for nonequilibrium processes. *Soviet physics, JETP*, 20:1018, 1965.

[60] K. Kitagawa, T. Morita, and S. Kimura. Molecular rectification of a helical peptide with a redox group in the metal-molecule-metal junction. *J. Phys. Chem. B*, 109:13906–13911, 2005.

[61] S. Kohler, J. Lehmann, and P. Hanggi. Driven quantum transport on the nanoscale. *Physics Reports*, 406:379, 2005.

[62] L. P. Kouwenhoven, S. Jauhar, K. McCormick, D. Dixon, P. L. McEuen, Yu. V. Nazarov, N. C. van der Vaart, and C. T. Foxon. Photon-assisted tunneling through a quantum dot. *Phys. Rev. B*, 50:2019–2022, 1994.

[63] L. P. Kouwenhoven, S. Jauhar, J. Orenstein, P. L. McEuen, Y. Nagamune, J. Motohisa, and H. Sakaki. Observation of photon-assisted tunneling through a quantum dot. *Phys. Rev. Lett.*, 73:3443–3446, 1994.

[64] L. P. Kouwenhoven, A. T. Johnson, N. C. van der Vaart, C. J. P. M. Harmans, and C. T. Foxon. Quantized current in a quantum-dot turnstile using oscillating tunnel barriers. *Phys. Rev. Lett.*, 67(12):1626–1629, Sep 1991.

[65] S. Kurth, G. Stefanucci, C. O. Almbladh, A. Rubio, and E. K. U. Gross. Time-dependent quantum transport: A practical scheme using density functional theory. *Phys. Rev. B*, 72:035308, 2005.

[66] J.G. Kushmerick, J. Lazorcik, C.H. Patterson, R. Shashidhar, D.S. Seferos, and G.C. Bazan. Vibronic contributions to charge transport across molecular junctions. *Nano. Lett.*, 4:639–642, 2004.

[67] R. Landauer. Electrical resistance of disordered one-dimensional lattices. *Philos. Mag.*, 21:863, 1970.

[68] N. D. Lang and Ph. Avouris. Carbon-atom wires: Charge-transfer doping, voltage drop, and the effect of distortions. *Phys. Rev. Lett.*, 84:358, 2000.

[69] N.D. Lang. Resistance of atomic wires. *Phys. Rev. B*, 52:5335–5342, 1995.

[70] D. C. Langerth. *Linear and Non-linear Electron Transport in Solids*. Plenum Press, New-York, 1976.

[71] B. Larade, J. Taylor, H. Mehrez, and H. Guo. *Phys. Rev. B*, 64:075420, 2001.

[72] P. J. Leek, M. R. Buitelaar, V. I. Talyanskii, C. G. Smith, D. Anderson, G. A. C. Jones, J. Wei, and D. H. Cobden. Charge pumping in carbon nanotubes. *Phys. Rev. Lett.*, 95(25):256802, Dec 2005.

[73] Jörg Lehmann, Sigmund Kohler, Peter Hänggi, and Abraham Nitzan. Molecular wires acting as coherent quantum ratchets. *Phys. Rev. Lett.*, 88(22):228305, May 2002.

[74] Jorg Lehmann, Sigmund Kohler, Peter Hanggi, and Abraham Nitzan. Rectification of laser-induced electronic transport through molecules. *The Journal of Chemical Physics*, 118(7):3283–3293, 2003.

[75] W. J. Liang, M. P. Shores, M. Bockrath, J. R. Long, and H. Park. Kondo resonance in a single-molecule transistor. *Nature*, 417:725–729, 2002.

[76] Rosa López, Ramón Aguado, Gloria Platero, and Carlos Tejedor. Kondo effect in ac transport through quantum dots. *Phys. Rev. Lett.*, 81:4688–4691, 1998.

[77] M. P. López Sancho, J. M. L. López Sancho, and J. Rubio. Highly convergent schemes for the calculation of bulk and surface green function. *J. Phys. F: Met. Phys.*, 15:851–858, 1985.

[78] Y. Luo, C. P. Collier, J. O. Jeppesen, K. A. Nielsen, E. Delonno, G. Ho, J. Perkins, H. R. Tseng, T. Yamamoto, J. F. Stoddart, and J. R. Heath. Two-dimensional molecular electronics circuits. *ChemPhysChem*, 3:519, 2002.

[79] J. Maciejko, J. Wang, and H. Guo. Time-dependent quantum transport far from equilibrium: An exact non linear response theory. *Phys. Rev. B*, 74:085324, 2006.

[80] R. L. McCreery. Molecular electronic junctions. *Chem. Mater.*, 16:4477–4496, 2004.

[81] R. M. Metzger. Unimolecular electrical rectifiers. *Chem. Rev.*, 103:3803–3834, 2003.

[82] M. Moskalets and M. Büttiker. Adiabatic quantum pump in the presence of external ac voltages. *Phys. Rev. B*, 69:205316, 2004.

[83] M. Moskalets and M. Büttiker. Adiabatic quantum pump in the presence of external ac voltages. *Phys. Rev. B*, 69(20):205316, May 2004.

[84] M. B. Nardelli. Electronic transport in extended systems: Application to carbon nanutubes. *Phys. Rev. B*, 60:7828–7833, 1999.

[85] D. Natelson, L. H. Yu, J. W. Ciszek, and Z. K. Tour J. M. Keane. Single-molecule transistors: Electron transfer in the solid state. *Chem. Phys*, 324:267–275, 2006.

[86] G. V. Nazin, X. H. Qiu, and W. Ho. Visualization and spectroscopy of a metal-molecule-metal bridge. *Science*, 302:77–81, 2003.

[87] D. Neuhauser and R. Baer. Efficient linear-response method circumventing the exchange-correlation kernel: Theory for molecular conductance under finite bias. *J. Chem. Phys.*, 123:204105, 2005.

[88] A. Nitzan. Electron transmission through molecles and molecular interfaces. *Annu. Rev. Phys. Chem.*, 52:681, 2001.

[89] Peter Nordlander, Michael Pustilnik, Yigal Meir, Ned S. Wingreen, and David C. Langreth. How long does it take for the kondo effect to develop? *Phys. Rev. Lett.*, 83(4):808–811, Jul 1999.

[90] Aletha M. Nowak and Richard L. McCreery. Characterization of carbon/nitroazobenzene/titanium molecular electronic junctions with photoelectron and raman spectroscopy. *Analytical Chemistry*, 76(4):1089–1097, 2004.

[91] Aletha M. Nowak and Richard L. McCreery. In situ raman spectroscopy of bias-induced structural changes in nitroazobenzene molecular electronic junctions. *J. Am. Chem. Soc.*, 126(50):16621–16631, 2004.

[92] H. Ohnishi, Y. Kondo, and Takayanagi. Quantized conductance through individual rows of suspended gold atoms. *Nature*, 395:780–783, 1998.

[93] T. H. Oosterkamp, T. Fujisawa, W. G. van der Wiel, K. Ishibashi, R. V. Hijman, S. Tarucha, and L. P. Kouwenhoven. Microwave spectroscopy of a quantum-dot molecule. *Nature*, 395:873–876, 1998.

[94] T. H. Oosterkamp, L. P. Kouwenhoven, A. E. A. Koolen, N. C. van der Vaart, and C. J. P. M. Harmans. Photon sidebands of the ground state and first excited state of a quantum dot. *Phys. Rev. Lett.*, 78(8):1536–1539, 1997.

[95] Hongkun Park, J Park, Andrew K. L. Lim, Erik H. Anderson, A. Paul Alivisatos, and Paul L. McEuen. Nanomechanical oscillations in a single-c60 transistor. *Nature*, 407:57–60, 2000.

[96] J. Park, A. N. Pasupathy, J. I. Goldsmith, C. Chang, Y. Yaish, J. R. Petta, M. Rinkoski, J. P. Sethna, H. D. Abruna, P. L. McEuen, and D. C. Ralph. Coulomb blockade and the kondo effect in single-atom transistors. *Nature*, 417:722–725, 2002.

[97] Paul G. Piva, Gino A. DiLabio, Jason L. Pitters, Janik Zikovsky, Moh'd Rezeq, Stanislav Dogel, Werner A. Hofer, and Robert A. Wolkow. Field regulation of single-molecule conductivity by a charged surface atom. *Nature*, 435:658–661, 2005.

[98] G. Platero and R. Aguado. Photon-assisted transport in semiconductor nanostructures. *Phys. Reports*, 395:1–157, 2004.

[99] A. Prociuk and B. D. Dunietz. Time-dependent current through electronic channel models using a mixed time-frequency solution of the equations of motion. *Phys. Rev. B*, 78:165112, 2008.

[100] A. Prociuk, B. Van Kuiken, and B. D. Dunietz. Benchmarking the performance of density functional theory based green's function formalism utilizing different self-energy models in calculating electronic transmission through molecular systems. *J.Chem.Phys.*, 125:204717, 2006.

[101] X. Qian, J. Ju Li, X. Lin, and S. Yip. Time-dependent density functional theory with ultrasoft pseudopotentials: Real-time electron propagation across a molecular junction. *Phys. Rev. B*, 73:035408, 2006.

[102] M. A. Reed, C. Zhou, C. J. Muller, T. P. Burgin, and J. M. Tour. Conductance of a molecular junction. *Science*, 278:252–254, 1997.

[103] T. Rueckes, K. Kim, E. Joselevich, G. Y. Tseng, C. L. Cheung, and C. M. Lieber. Carbon nanotube-based nonvolatile random access memory for molecular computing. *Science*, 289:94–97, 2000.

[104] N. Sai, M. Zwolak, G. Vignale, and M. Di Ventra. Dynamical corrections to the dft-lda electron conductance in nanoscale systems. *Phys. Rev. Lett.*, 94:186810, 2005.

[105] M. P. Samanta, W. Tian, S. Datta, J. I. Henderson, and C. P. Kubiak. Electronic conduction through organic molecules. *Phys. Rev. B*, 53:R7626–R7629, 1996.

[106] T. Seideman and W. H. Miller. Quantum-mechanical reaction probabilities via a discrete variable representation-absorbing boundary-condition green-function. *J. Chem. Phys.*, 97:2499–2514, 1992.

[107] Y. Shao, L. Fusti-Molnar, Y. Jung, J. Kussmann, C. Ochsenfeld, S. T. Brown, A. T. B. Gilbert, L. V. Slipchenko, S. V. Levchenko, D. P. O'Neill, R. A. Distasio Jr., K. Lochan, T. Wang, G. J. O. Beran, N. A. Besley, J. M. Herbert, C. Y. Lin, T. Van Voorhis, S. H. Chien, A. Sodt, R. P. Steele, V. A. Rassolov, P. E. Maslen, P. P. Korambath, R. D. Adamson,

B. Austin, J. Baker, E. F. C. Byrd, H. Dachsel, R. J. Doerksen, A. Dreuw, B. D. Dunietz, A. D. Dutoi, T. R. Furlani, S. R. Gwaltney, A. Heyden, S. Hirata, C.-P. Hsu, G. Kedziora, R. Z. Khalliulin, P. Klunzinger, A. M. Lee, M. S. Lee, W. Liang, I. Lotan, N. Nair, B. Peters, E. I. Proynov, P. A. Pieniazek, Y. M. Rhee, J. J Ritchie, E. Rosta, C. D. Sherrill, A. C. Simmonett, J. E. Subotnik, H. L. Woodcock III, W. Zhang, A. T. Bell, A. K. Chakraborty, D. M. Chipman, F. J. Keil, A. Warshel, W. J. Hehre, H. F. Schaefer III, J. Kong, A. I. Krylov, P. M. W. Gill, and M. Head-Gordon. Advances in methods and algorithms in a modern quantum chemistry program package. *Phys. Chem. Chem. Phys.*, 8(27):3172–3191, 2006.

[108] C. A. Stafford and Ned S. Wingreen. Resonant photon-assisted tunneling through a double quantum dot: An electron pump from spatial rabi oscillations. *Phys. Rev. Lett.*, 76:1916–1919, 1996.

[109] G. Stefanucci. Bound states in *ab initio* approaches to quantum transmport: A time dependent formulation. *Phys. Rev. B*, 75:195115, 2007.

[110] G. Stefanucci and C. O. Almbladh. Time-dependent partition free approach in resonant tunneling systems. *Phys. Rev. B*, 69:195318–195334, 2004.

[111] G. Stefanucci and C. O. Almbladh. An exact *ab-initio* theory of quantum transport using tddft and nonequilibrium green's functions. *J. of Physics: Conference series*, 35:17–24, 2006.

[112] G. Stefanucci, S. Kurth, A. Rubio, and E. K. U. Gross. Time-dependent approach to electron pumping in open quantum systems. *Phys. Rev. B*, 77:075339, 2008.

[113] B. C. Stipe, M. A. Rezaei, and W. Ho. Single-molecule vibrational spectroscopy and microscopy. *Science*, 280:1732–1735, 1998.

[114] K. Stokbro, J. Taylor, M. Brandbyge, J. L. Mozos, and P. Ordejon. Theoretical study of the non linear conductance of di-tiol benzene coupled to au(111) surfaces via thiol and thiolate bonds. *Comput.Mater.Sci*, 27:151–160, 2002.

[115] T. H. Stoof and Yu. V. Nazarov. Time-dependent resonant tunneling via two discrete states. *Phys. Rev. B*, 53(3):1050–1053, Jan 1996.

[116] M. Switkes, C. M. Marcus, K. Campman, and A. C. Gossard. An Adiabatic Quantum Electron Pump. *Science*, 283:1905–1908, 1999.

[117] A. Szabo and N. S. Ostlund. *Modern Quantum Chemistry, First Edition, Revised*. McGraw Hill Publishing Company, New York, 1989.

[118] J. Taylor, H. Guo, and J. Wang. *Ab initio* modeling of quantum transport properties of molecular electronic devices. *Phys. Rev. B*, 63:245407, 2001.

[119] W. Tian, S. Datta, S. Hong, R. Reifenberger, J. I. Henderson, and C. P. Kubiak. Conductance spectra of moleceular wires. *J. Chem. Phys.*, 109:2874–2882, 1998.

[120] Luis E. F. Foa Torres. Mono-parametric quantum charge pumping: Interplay between spatial interference and photon-assisted tunneling. *Phys. Rev. B*, 72:245339, 2005.

[121] J. M. Tour, A. M. Rawlett, M. Kozaki, Y. X. Yao, R. C. Jagessar, S. M. Dirk, D. W. Price, M. A. Reed, C. W. Zhou, J. Chen, W. Y. Wang, and I. Campbell. Synthesis and preliminary testing of molecular wires and devices. *Chem.-Eur. J.*, 7:5118–5134, 2001.

[122] N. C. van der Vaart, S. F. Godijn, Y. V. Nazarov, C. J. P. M. Harmans, J. E. Mooij, L. W. Molenkamp, and C. T. Foxon. Resonant tunneling through two discrete energy states. *Phys. Rev. Lett.*, 74(23):4702–4705, Jun 1995.

[123] R. van Leeuwen, N. E. Dahlen, G. Stefanucci, C.-O. Almbladh, and U. von Barth. Introduction to the Keldysh formalism and applications to time-dependent density-functional theory. *ArXiv Condensed Matter e-prints*, June 2005.

[124] M. G. Vavilov, L. DiCarlo, and C. M. Marcus. Photovoltaic and rectification currents in quantum dots. *Phys. Rev. B*, 71(24):241309, 2005.

[125] W. R. Wadt and J. P. Hay. *J. Chem. Phys.*, 82:299, 1985.

[126] Baigeng Wang, Jian Wang, and Hong Guo. Parametric pumping at finite frequency. *Phys. Rev. B*, 65(7):073306, Jan 2002.

[127] D. R. Ward, N. J. Halas, J. W. Ciszek, J. M. Tour, Y. Wu, P. Nordiander, and D Natelson. Simultaneous measurements of electronic conduction and raman response in molecular junctions. *Nano. Lett.*, 8:919–924, 2008.

[128] B. H. Wu and J. C. Cao. Interference of conductance and shot noise properties of photon-assisted transport through a t-shaped double quantum dot. *Phys. Rev. B*, 73(20):205318, 2006.

[129] X. Xiao, B. Q. Xu, and N. Tao. Changes in the conductance of single peptide molecules upon metal-ion binding. *Angew. Chem. Int. Ed.*, 45:6148–6152, 2004.

[130] X. Xiao, B. Q. Xu, and N. Tao. Measurement of single molecule conductance: Benzenedithiol and benzenedimethanethiol. *Nano. Lett.*, 4:267–271, 2004.

[131] B. Q. Xu and N. Tao. Measurement of single-molecule resistance by repeated formation of molecular junctions. *Science*, 301:1221–1223, 2003.

[132] B. Q. Xu, X. Y. Xiao, X. Yang, L. Zang, and N. J. Tao. Large gate modulation in the current of a room temperature single molecule transistor. *J.Amer.Chem.Soc.*, 127(8):2386–2387, 2005.

[133] Y. Xue, S. Datta, and M. A. Ratner. Charge transfer and "band lineup" in molecular electronic devices: A chemical and numerical interpretation. *J. Chem. Phys.*, 115:4292–4299, 2001.

[134] Y. Xue, S. Datta, and M. A. Ratner. First-principles based matrix green's function approach to molecular electronic devices: general formalism. *Chem. Phys*, 281:151–170, 2002.

[135] Y. Xue and M. A. Ratner. Microscopic study of electrical transport through individual molecules with metallic contacts. i band lineup, voltage drop, and high-field transport. *Phys. Rev. B*, 68:115406, 2003.

[136] S. N. Yaliraki, A. E. Roitberg, C. Gonzalez, V. Mujica, and M. A. Ratner. The injecting energy at molecule/metal interfaces: Implications for conductance of molecular junctions from an ab initio molecular description. *J. Chem. Phys.*, 111:6997–7002, 1999.

[137] A. I. Yanson, G. Rubio Rollinger, H. E. van der Brom, N. Agrait, and J. M. van Ruitenbeek. Formation and manipulation of a metallic wire of single gold atoms. *Nature*, 395:783–785, 1998.

[138] F. Zhou, B. Spivak, and B. Altshuler. Mesoscopic mechanism of adiabatic charge transport. *Phys. Rev. Lett.*, 82(3):608–611, 1999.